Experiments on Superconducting Qubits Coupled to Resonators

Untersuchung an Resonatoren gekoppelter supraleitender Qubits

Zur Erlangung des akademischen Grades eines
DOKTORS DER NATURWISSENSCHAFTEN
von der Fakultät für Physik des
Karlsruher Institut für Technologie (KIT)

genehmigte

DISSERTATION

von

Dipl.-Phys. Markus Jerger
aus Bühl

Tag der mündlichen Prüfung: 1. Februar 2013

Referent: Prof. Dr. Alexey V. Ustinov
Korreferent: Prof. Dr. ir. J. E. Mooij

Contents

1 Introduction

Classical and Quantum Computation

In the period of a few decades, computers have conquered the world. Once bulky and expensive machines, they have evolved into everyday devices that fit into the smallest pocket. Today, a daunting amount of computational power is at anyones disposal.

It is debatable when the first computer (in a broad sense) was contrived – the first known mechanical calculation aid, the Abacus, dates back some 3,000 years; and first mechanical adding machines were built in the 1600s. However all these machines were special-purpose devices, applicable only to a very limited range of problems. The birth of the universal computer can be fixed to the late 1930s, when Alan Turing described a theoretical model[Tur37] that later became known as the Turing machine. The Church-Turing thesis[Tur39] asserts that every effectively calculable function can be computed by such a machine.

Computability does not imply that a computation can be done efficiently, i.e. that the time and memory required for the computation scales at most polynomially with the size of the input, and in fact it turns out that many problems of practical interest can not be efficiently calculated on a Turing machine. In a 1981 talk[Fey82], Richard Feynman pointed out that the numerical simulation of quantum physics is among those problems. The simplest argument that can be made to prove this is that the number of matrix elements of a composite quantum system's wave function, and therefore the memory required to store them, increases exponentially with the number of constituent parts. Feynman proposed to overcome this problem by mapping the system onto a lattice of two-state quantum systems, later designated qubits, with configurable nearest-neighbor interactions, a device he calls an universal quantum simulator.

In the course of the 1980s his idea was developed further, culminating in the concept of the universal quantum computer. The universal quantum computer is a device very similar to a Turing machine but empowered with superposition and entanglement, two distinctively quantum features. In the quantum theory of computation, it plays the same role the Turing machine plays in the classical theory[Deu89]. A revised version of the Church-Turing thesis due to David Deutsch[Deu85] concludes that it can perfectly simulate every finitely realizable (quantum) physical system.

Like the Turing machine, the universal quantum computer is an abstract concept rather than a construction blueprint of a physical device. To describe the workings of practical computers the circuit model[Deu89] is more intuitive to use. It depicts the computer as a network of quantum gates akin to a classical electrical circuit of logic gates, with each gate representing a unitary transformation applied to a subset of qubits. Only a handful of different gates, namely single qubit rotations and an almost arbitrary two-qubit gate[Llo95], suffice to make the circuit model universal.

By design, any classical algorithm will also run on a universal quantum computer with equal efficiency. If this was the end of the story, if quantum computation could not do significantly better than classical computation in a problem of practical significance, no one would bother contemplating it. Luckily, a few quantum algorithms are known to provide an exponential speedup compared to any known classical alternative. These have spawned interest in the field and promoted the construction of real quantum computers.

Decoherence

The main difficulty in the physical realization of quantum computers is eliminating any undesirable interactions of its constituent qubits. Ultimately, such interactions will distort the result of the computation by altering the quantum state of the computer, a process called decoherence. Decoherence can result from qubits interacting with their environment, but also from the qubit interacting with other degrees of freedom of the system comprising the qubits. This favors qubits of microscopic size, such as photons or trapped atoms, because these tend to have few internal

degrees of freedom and to be well isolated from their environment. Of course, in order to operate the computer in the first place, it must be possible to exert control on the individual qubits and establish mutual interactions.

In this regard, superconducting qubits, such as the ones studied in this thesis, outperform the microscopic systems. At sizes that can reach hundreds of square micrometers, they can be designed and embedded in an electronic circuit and manufactured complete with control lines using standard lithograpic means. Inducing interactions between superconducting qubits is as simple as placing an actual wire between them. Unfortunately, all this comes at the price of increased decoherence.

The first experiment showing coherence in a superconducting qubit, published in 1999, saw coherent oscillations lasting up to 2 ns[NPT99]. Step by step, various experimental groups have improved this number, working on multiple fronts. Ever new variants of superconducting qubits have been devised, with very different modes of operation despite being based on the same basic circuit elements (a few examples can be found in section 2.2). By exploiting symmetries and through enhanced shielding, the influence of a noisy electromagnetic environment could be reduced. The coupling to material defects has been lessened by lowering electric fields in the places where it mattered, and the defect densities themselves have been lowered by advancing materials and manufacturing processes. Progress has been so tremendous[Ste11] that an equivalent of Moore's law[1] has been suggested for the decoherence times of superconducting qubits[DiV12]. At the time of this writing, decoherence times have reached 100 µs[RGP+12] (ironically, at some expense of control over the qubit) and further enhancements are expected.

Quantum Error Correction

Current coherence times preclude the execution even of moderately complex algorithms and they are extremely short compared to the inverse error rate of classical computer memory, which is of the order of 5×10^{13} s[SPW09], almost eighteen orders of magnitude more. Even

[1] Gordon Moore predicted in 1965 that the number of components in classical integrated circuits would double every two years[Moo65].

this seemingly enormous time is not good enough – for 1 GB of memory, it translates to one bit flip every other hour – so error correction mechanisms are used to boost it even further.

At first glance, error correction of qubits appears to be impossible for two reasons. First, the destructive nature of the quantum-mechanical measurement process means that it must be done without knowing either their original nor their decohered states. Second, a quantum state is a fundamentally analog quantity, being described by a number of continuous-valued probability amplitudes. Unlike the discrete bit flips in the classical case, errors in these amplitudes grow continuously as time passes. Perhaps surprisingly, quantum error correction is possible nonetheless.

Peter Shor was the first to note this and proposed an encoding scheme of one logical qubit in nine physical qubits[Sho95] that can perfectly restore the original state if one of the physical qubits decoheres. The crucial point of his idea is the realization that measuring the physical qubits to find out if and where an error occured is not a problem – as long as it does not reveal any information about the state of the logical qubit. The measurement then takes care of the second problem by projecting the initially continous-valued error onto one out of four possible discrete outcomes. These correspond to no error and flips (180° rotations) about the x, y or z axes, which can be corrected by applying the appropriate unitary gate. In the following years, improved error correction codes have been developed, of which the most notable ones are the seven qubit code by Andrew Steane[Ste96] which maps many basic gates on the logical qubit to simple operations on the physical qubits[Mer07], and the surface codes based on work by Alexei Kitaev[Kit03], which have a simple structure and are more economic when the state of a large number of qubits is to be protected. The latter accomplish an error tolerance of 0.75% per gate[DiV09], which is in reach of current experimental implementations.

Towards Large-scale Quantum Computers

Having reduced the role of decoherence from a show stopper to a mere inconvenience, the next challenge is to increase the number of qubits

working together in a quantum processor. All devices that have been experimentally realized so far contain no more than a handful of qubits. While this is sufficient to demonstrate basic quantum gates and even simple algorithms, these processors are mere toys in the big picture of quantum computation. To do better than the highly evolved classical computers available today, at least a few tens of interacting qubits (not including the overhead due to error correction) are necessary.

The path to larger quantum computers poses new experimental challenges, concerning the arrangement of many interacting qubits, the placement of the increasing number of control and measurement connections and more. This thesis provides a modest contribution to this large field by demonstrating a method to control and measure multiple qubits simultaneously, that can in principle be used to measure hundreds of qubits through a single pair of wires.

The method is based on circuit quantum electrodynamics, the study of interactions between artificial atoms (the qubits) with photons stored in a microwave cavity. Due to these interactions, the energy required to add a photon to the cavity depends on the state of the qubit, which can hence be determined by scattering electromagnetic waves at the cavity input. Many cavities with slightly different resonance frequencies can be connected in parallel to a common microwave transmission line, allowing an almost arbitrary number of qubits to be measured through the line. Moreover, qubit-cavity interactions can be used to convert the qubit state into a cavity state and back, which enables a cavity to serve as a quantum memory or a means to transfer quantum states between distant qubits. All these features make circuit quantum electrodynamics a powerful architecture for quantum computation. It may become the key element to the realization of large-scale quantum computers.

2 Building Blocks

2.1 Superconductivity and the Josephson Effect

In 2011, the physics community celebrated the 100th anniversary of the discovery of superconductivity by H. Kammerlingh Onnes[Onn11]. Onnes found that the resistance of a number of metals vanished below a certain, material-dependent (critical) temperature T_c. Later experiments on the persistence of circulating currents injected into (macroscopic) superconducting rings found a lower bound of 10^5 years[Tin04], which confirmed that the resistance of a superconductor was indeed exactly zero.

A few years later, in 1933, Meißner and Ochsenfeld discovered the second basic property of a superconductor, perfect diamagnetism[MO33]. While perfect conductance would by itself cancel any change of a magnetic field penetrating the superconductor by induction of eddy currents, they found that in addition to that the superconductor would expell any magnetic field already present when T_c was crossed. The existence of the reversible Meißner effect proved that superconductivity was a distinct thermodynamic state[Tin04]. A description of the superconducting state reproducing these two effects was given by F. and H. London in 1935[LL35], but it was purely phenomenological and did not explain its microscopic origin.

Measurements of the electronic heat capacity of superconductors found an exponential T-dependence, which indicates the presence of an energy gap in the excitation spectrum. This discovery led to the formulation of a microscopic theory of superconductivity by Bardeen, Cooper and Schrieffer in 1957[BCS57], which showed that a weak attractive force between electrons can cause them to form a condensate of bosonic pairs with zero total spin and momentum. The energy 2Δ required to break these so-called Cooper-pairs is equal to the gap energy, and its prediction

by the BCS theory matched the measured value. The finite energy gap also explains the lack of resistivity, because it inhibits scattering of the Cooper-pairs at impurities.

Both the London equations and BCS theory did not take spacial variations of the properties of the material into account. This is considered in the Ginzburg-Landau theory of superconductivity[GL50], which was initially formulated as a phenomenological theory but later derived from a generalized BCS theory[Gor59]. Ginzburg and Landau declared a complex parameter $\psi(\vec{r})$, which serves as a macroscopic wave function of the charge carriers and an order parameter of the superconducting phase transition. It is linked to the local density of Cooper-pairs in the material via $n_s(\vec{r}) = |\psi(\vec{r})|^2$. The theory also introduces the coherence length ξ, the characteristic length scale at which $\psi(\vec{r})$ may vary without excessive increase of the thermodynamic energy of the condensate, typically a few 100 nm.

The finite coherence length implies that at the interface of a superconductor (S) and a normal metal (N) or insulator (I), some Cooper-pairs will be present inside the non-superconducting material. Furthermore, in a sandwich of two superconducting electrodes with a very thin interposed N or I layer, there would be interference of the macroscopic wave functions of the two superconductors. B. Josephson predicted[Jos62] that a supercurrent

$$I_s = I_c \sin(\phi) \tag{2.1}$$

would flow through such a structure even in the absence of an external voltage. I_c is the maximum supercurrent that the structure can support and depends on its geometry. $\phi = \arg(\psi_1) - \arg(\psi_2)$ is the difference of the phases of the wave functions of the superconductors. Josephson further predicted that in the presence of a voltage difference V between the electrodes, their phase difference would evolve according to

$$\frac{\mathrm{d}\phi}{\mathrm{d}t} = \frac{2eV}{\hbar} = \frac{2\pi V}{\Phi_0}. \tag{2.2}$$

Eqns. 2.1 and 2.2 are called the first and second Josephson equations, respectively.

If an alternating current is applied, a Josephson junction can be considered a non-linear inductor. Comparing the Josephson equations to the

response of a linear inductor, $V = -L\,\mathrm{d}I/\mathrm{d}t$, the self-inductance L_J, which depends on the phase drop across the junction, can be derived as

$$L_J(\phi) = \frac{\Phi_0}{2\pi I_c \cos(\phi)}. \tag{2.3}$$

By controlling the phase drop ϕ, the inductance of the junction to be adjusted. Unlike ordinary inductors, Josephson junctions can have a negative inductance. A series junction can thus reduce the total inductance of a circuit.

The Josephson energy stored inside a junction can be derived from $U_J = \int I_s V \mathrm{d}t$, Eq. 2.1 and Eq. 2.2, yielding

$$U_J(\phi) = E_J[1 - \cos(\phi)], \tag{2.4}$$

with $E_J = \hbar I_c/2e$. The constant of integration was chosen such that $U_J(\phi)$ has a minimum of 0 in the case of a vanishing phase difference, corresponding to the situation in a bulk superconductor.

The geometric structure of a junction resembles that of a plate capacitor. Therefore, the total energy stored in the junction must also include the electrostatic energy of the charges stored on the capacitor plates,

$$T = \frac{Q^2}{2C} = E_C(N_C - N_g)^2.$$

Here, $E_C = 4e^2/2C$, is the Coulomb energy of a single Cooper pair stored on the capacitor, called the charging energy. N_C is the integer number of pairs that have tunneled through the junction and N_g is an externally applied charge bias, called gate charge.

2.2 The Flux Qubit

2.2.1 Basic Types of Superconducting Qubits

As we have seen in section 1, a qubit is a quantum system with two states that can be distinguished by measurement. Few microscopic implementations of qubits, such as photonic and nuclear spins, are indeed naturally occuring two-level systems. But natural two-level systems are rare and

all other approaches rely on a nonlinear energy spectrum to isolate two computational basis states. For the realization of a qubit in an electric circuit, Josephson junctions are an evident choice, because they are the only known nonlinear and nondissipative electrical components[ZB07]. The three basic types of superconducting qubits are the charge qubit, the phase qubit and the flux qubit.

The charge qubit or Cooper-pair box[BVJ+98]; [NPT99] was the first experimentally demonstrated superconducting qubit. The computational states of the charge qubits are states with a well-defined number of Cooper-pairs on a superconducting island separated by a Josephson junction. In order to distinguish the charge of a single Cooper-pair, the island must be sufficiently small, such that $E_C \gg E_J$ and the electrostatic term dominates the total energy of the system. The qubit is best operated with a half-integer gate charge, where the states $|N_C = N_g - \frac{1}{2}\rangle$ and $|N_C = N_g + \frac{1}{2}\rangle$ are degenerate. The degeneracy is lifted by the Josephson energy E_J, which sets the frequency of the qubit transition. The Cooper-pair box is very sensitive to charge noise and has largely been replaced by an improved variant, the transmon qubit[SHS+07].

Phase qubits[MNA+02]; [YHC+02] operate in the opposite regime, $E_J \gg E_C$. A phase qubit is realized as a single junction which is current-biased. The bias current skews the $\cos\phi$ potential with a linear term, resulting in the so-called tilted washboard potential. The tilt is adjusted such that only 3–10 states remain in each of the local minima of U_J, which can be approximated as anharmonic oscillators. The computational basis can be formed by the lowest two states in any minimum. Current implementations of the phase qubit provide the bias by enclosing the junction in a flux-biased loop, which allows improved decoupling of the qubit from environmental noise.

Originally, the flux qubit[FPC+00] consisted also of a single junction in a closed loop. The magnetic energy stored in the loop inductance adds a parabolic term to the potential. At a flux bias close to $\Phi_0/2$, U_J has two degenerate minima separated by a tunnel barrier. The tunneling matrix element of the ground states of the two minima lifts their degeneracy, the lowest two states are used as qubit states. In practise, this type of qubit suffers from strong dephasing, because the relatively large loop

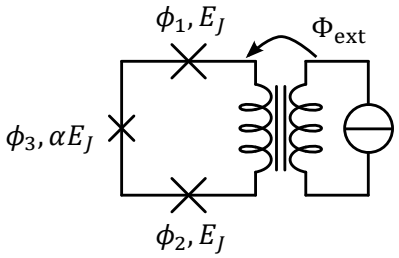

Figure 2.1: Circuit schematic of a magnetically biased three-junction flux qubit. The third junction is called the alpha junction and has an α times lower critial current than the other junctions.

inductance results in strong magnetic fields that couple the qubit to the environment. This problem was solved by the three-junction flux qubit, which essentially uses the additional junctions to replace the loop inductance.

2.2.2 Classical Description of the Three-Junction Flux Qubit

The three-junction flux qubit[MOL+99], commonly simply called the flux Qubit, consists of a superconducting ring interrupted by three Josephson junctions, where one of the junctions is by a factor α smaller than the other two. Since the macroscopic wave function $\psi(\vec{r}) \equiv |\psi(\vec{r})| \exp(i\phi(\vec{r}))$ of the superconductor must be single-valued, the phase $\phi(\vec{r})$ collected when going once around the ring must be an integer multiple of 2π, which imposes the flux quantization condition,

$$\sum_i \phi_i + 2\pi f = 2\pi N, \tag{2.5}$$

where ϕ_i is the phase difference across the i'th junction, $f = \Phi_{\text{ext}}/\Phi_0$ is the frustration of the loop generated by an external magnetic field, and N is the number of flux quanta trapped inside the loop. A circuit schematic of the qubit is shown in Fig. 2.1.

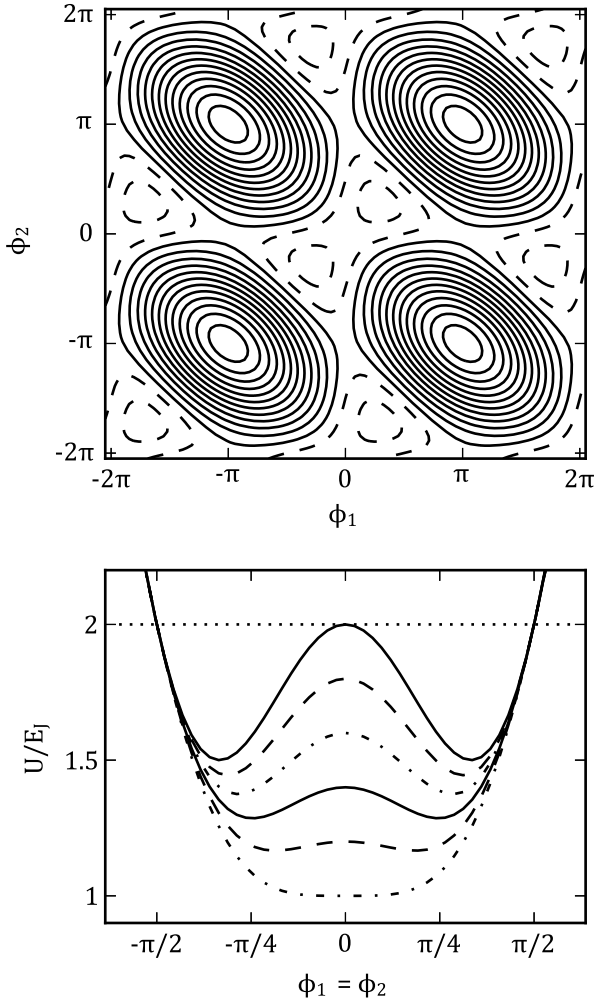

Figure 2.2: Potential energy of a flux qubit at $f = 0.5$. (top) Contour plot at $\alpha = 0.8$. The qubit states are located inside the double well (dashed contours) in the center of the plot. (bottom) Shape of the tunneling barrier in the qubit double well at different values of α. The bottom (dash-dotted) curve is for $\alpha = 0.5$, the top (solid) curve for $\alpha = 1.0$ with steps of 0.1. The height of the barrier between different unit cells, located at $(\phi_1, \phi_2) = (0, \pm\pi)$ and $(\pm\pi, 0)$ and shown for comparison as a dotted line, is independent of α.

Combining the potential energy stored in each junction, Eq. 2.4, with the flux quantization condition, Eq. 2.5, yields the total potential energy of the qubit loop,

$$U_J/E_J = 2 + \alpha - \cos(\phi_1) - \cos(\phi_2) - \alpha\cos(2\pi f - \phi_1 - \phi_2), \quad (2.6)$$

where E_J is the Josephson energy of each of the large junctions. It is assumed that the energy stored in the magnetic field generated by the geometric inductance of the loop is negligible compared to the energy stored inside the junctions. This is equivalent to the junction inductance L_J, Eq. 2.3, being much larger than the geometric inductance L_{geo} of the qubit loop.

The potential is independent of the number of flux quanta trapped in the loop and has two internal degrees of freedom, ϕ_1 and ϕ_2. It is 2π-periodic in both, seen from Eq. 2.6 or Fig. 2.2. A flux qubit is formed for $0.5 < \alpha < 1.0$, where the potential describes a lattice of isolated double-wells, composed of two minima and a tunneling barrier along the $\phi_1 = \phi_2 \mod 2\pi$ axis in each $(2\pi)^2$ unit cell. At $\alpha = 1$, the potential barriers between individual unit cells and the tunneling barrier between the double wells have the same height and the system becomes effectively two-dimensional. For $\alpha < 0.5$, the tunneling barrier vanishes completely, resulting in a crossover from a lattice of tunneling systems to a lattice of ordinary anharmonic oscillator potentials.

Classically, the two lowest states of the flux qubit are located at the minima of the double wells, which are degenerate at half frustration, $f = 0.5$. At the minima, the phase difference across the junctions is $(\phi_1, \phi_2) = \pm(\phi^*, \phi^*)$, where ϕ^* can be calculated[MOL+99] to be

$$\cos\phi^* = \frac{1}{2\alpha}. \quad (2.7)$$

This results in a supercurrent flowing around the loop, which differs in sign between the two wells. Its magnitude can be calculated by plugging Eq. 2.7 into the first Josephson relation Eq. 2.1,

$$I_p = I_c \sin(\phi^*) = I_c\sqrt{1 - \frac{1}{4\alpha^2}}. \quad (2.8)$$

At f different from 0.5, the magnetic moment generated by the current circulating in the loop couples to the external magnetic field used to bias the circuit and tilts the double well potential. In this case, the two persistent current states are no longer degenerate and their energy difference is

$$\hbar\epsilon = 2I_p(\Phi_{\text{ext}} - \Phi_0/2) = 2I_p\Phi_0(f - 0.5). \tag{2.9}$$

To describe the dynamics of the flux qubit system, the kinetic energy of the circuit has to be taken into account. The second Josephson relation, Eq. 2.2, hints that this is equal to the energy of the charges stored on the islands between the Josephson junctions. If the capacitances of the islands to ground can be neglected in comparison to the capacitances across the junctions, the kinetic energy term becomes simply

$$T = \frac{1}{2}\sum_i C_i V_i^2 = \frac{1}{2}\left(\frac{\Phi_0}{2\pi}\right)^2 \begin{pmatrix}\dot{\phi}_1 & \dot{\phi}_2\end{pmatrix} \cdot \mathbf{C} \cdot \begin{pmatrix}\dot{\phi}_1 \\ \dot{\phi}_2\end{pmatrix}.$$

A coordinate rotation from ϕ_1 and ϕ_2 to $\phi_p = (\phi_1 + \phi_2)/2$ and $\phi_m = (\phi_1 - \phi_2)/2$, diagonalizes the $\mathbf{C}$ matrix without complicating U_J,

$$U_J/E_J = 2 + \alpha - 2\cos(\phi_p)\cos(\phi_m) - \alpha\cos(2\pi f - 2\phi_p).$$

2.2.3 Quantum-Mechanical Description

From T and U_J, the classical Lagrangian and Hamiltonian are derived, and by considering the classical phases and their conjugate momenta as operators, the transition to a quantum mechanical description of the system is made[OMT+99]. This results in the quantum Hamiltonian

$$H = \frac{P_p^2}{2M_p} + \frac{P_m^2}{2M_m} + U_J, \tag{2.10}$$

where the momentum operators can be written as $P_p = -i\hbar\partial/\partial\phi_p$ and $P_m = -i\hbar\partial/\partial\phi_m$, the mass terms are $M_p = 2C(\Phi_0/2\pi)^2$ and $M_m = 2C(1+2\alpha)(\Phi_0/2\pi)^2$, and C is the capacitance of one of the large junctions.

The eigenenergies and eigenstates of this Hamiltonian can be found in a phase basis by truncating H to a discrete grid of points in (ϕ_p, ϕ_m)

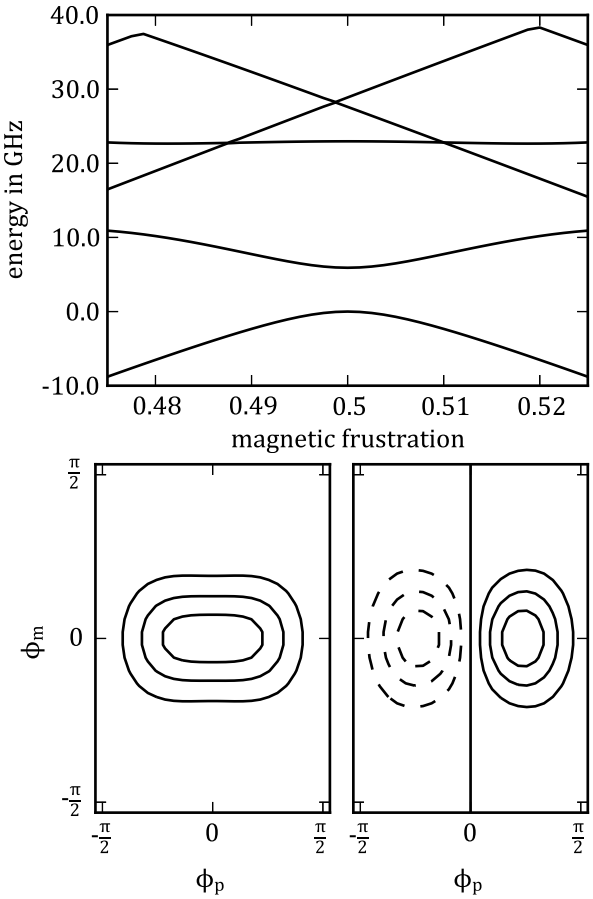

Figure 2.3: Numerical simulation of the steady-state properties of a flux qubit. The parameters are $E_J = 140\,\mathrm{GHz}$, $E_C = 2.8\,\mathrm{GHz}$ and $\alpha = 0.645$. (top) Energies of the five lowest-lying states of the Hamiltonian. At half frustration, the transition energy between the ground state and the first excited state reaches a minimum of $\Delta = 5.9\,\mathrm{GHz}$. The second excited state is $17\,\mathrm{GHz}$ higher than the first excited state, making the truncation to two 'qubit' states very accurate. (bottom) Wave functions of the qubit ground and first excited states at half frustration. The ground state is a symmetric combination of the two persistent current states, the first excited state is an asymmetric combination. Both states have zero net circulating currents. Solid contours denote $\Re\psi > 0$, dashed contours $\Re\psi < 0$. The distance between contours is 0.025.

space and numerical diagonalization of the resulting Hamiltonian matrix, where effects of the other unit cells are included by considering periodic boundary conditions. Alternatively, the problem can be treated in the charge basis by limiting the number of charges that can be on each island, which are naturally discrete. In this case, the basis states are plane waves in ϕ_p and ϕ_m. The phase basis solutions are plotted vs. magnetic frustration of the qubit loop in Fig. 2.3, for the design parameters of one of the manufactured qubits.

At half frustration, the qubit potential is symmetric and the two classical persistent current states are degenerate. In the quantum-mechanical description, this degeneracy is lifted by hybridization of the persistent current states due to the finite height of the tunneling barrier. The height of the tunneling barrier is defined by the geometry of the qubit junctions, and so the hybridization energy, which is at the same time the minimum transition energy between the qubit states, is fixed during device fabrication. This energy is commonly called the qubit gap and labelled $\hbar\Delta$, in reference to the terminology used in the description of tunneling systems.

Not too far from half frustration, the coupling of the current circulating in the loop adds an additional term called the asymmetry energy $\hbar\epsilon$. This is essentially the same as the classical asymmetry, Eq. 2.9, with the classical I_p replaced by the expectation value of the circulating current for the relevant states.

Far from half frustration, multiple quantum states are allowed in the lower well that are energetically below the ground state of the higher well, and the classical persistent current states can no longer be identified with the two qubit states.

2.2.4 Truncation to two Levels

From Fig. 2.3, it can be seen that the energy required to access the second excited state is several times larger than the transition energy between the ground and first excited states in the vincinity of half frustration. Thus, a flux qubit is approximated very well by its two lowest states. A two-level Hamiltonian can be constructed from the gap and asymmetry

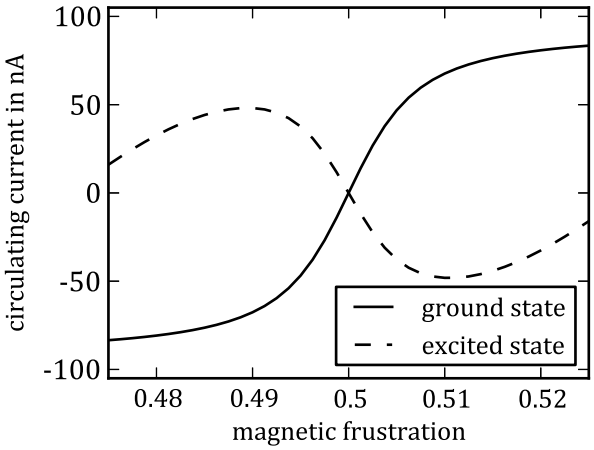

Figure 2.4: Numerical simulation of the persistent current in the qubit loop for the ground and first excited states of a flux qubit. At $f = 0.5$, both states are an equal superposition of the classical clockwise and counter-clockwise states and the net circulating current vanishes. The parameters are $E_J = 140\,\mathrm{GHz}$, $E_C = 2.8\,\mathrm{GHz}$ and $\alpha = 0.645$.

parameters derived in the previous section, taking the persistent current states as the basis states. It reads

$$\tilde{H} = \frac{\hbar}{2}\Delta\tilde{\sigma}_x + \frac{\hbar}{2}\epsilon\tilde{\sigma}_z = \frac{\hbar}{2}\begin{pmatrix}\epsilon & \Delta\\ \Delta & -\epsilon\end{pmatrix}, \tag{2.11}$$

where σ_x and σ_z are the first and third Pauli matrices.

This Hamiltonian is diagonalized by a unitary rotation around the y axis,

$$U = \exp(i\theta\tilde{\sigma}_y) = \begin{pmatrix}\cos\theta & \sin\theta\\ -\sin\theta & \cos\theta\end{pmatrix}, \tag{2.12}$$

by an angle of $\tan 2\theta = \Delta/\epsilon$. In the rotated basis, the Hamiltonian becomes

$$H = U^\dagger\tilde{H}U = \frac{\hbar}{2}\sqrt{\Delta^2+\epsilon^2}\,\sigma_z \tag{2.13}$$

where the qubit transition frequency is identified as $\omega_q = \sqrt{\Delta^2+\epsilon^2}$.

The qubit states, written in the circulating current basis, are

$$|\uparrow\rangle = \quad \cos\theta|l\rangle + \sin\theta|r\rangle \tag{2.14}$$
$$|\downarrow\rangle = -\sin\theta|l\rangle + \cos\theta|r\rangle. \tag{2.15}$$

At the symmetry point, $\theta = \pm\pi/4$ and both qubit states are superpositions of the clockwise and counter-clockwise persistent current states with equal probability amplitudes, resulting in zero net current flowing in the loop in both states. At large asymmetries, $\theta \to 0$ and the qubit states become equal to the persistent current states. In Fig. 2.4, the expectation values of the circulating current for the two lowest state of the full Hamiltonian, Eq. 2.10, are plotted.

2.2.5 Driven Qubit

An external drive can be introduced to the qubit by inductive coupling to a microwave field. The microwave signal presents an oscillating magnetic field to the qubit, which periodically perturbes the asymmetry energy. It is thus proportional to a σ_z operator in the basis of the persistent current states,

$$\tilde{H}_{\text{drive}} = \frac{A}{2}\cos(\omega_d t + \varphi)\tilde{\sigma}_z, \tag{2.16}$$

where A is the amplitude of the drive. The drive is rotated into the qubit eigenbasis by application of the unitary transformation Eq. 2.12,

$$H_{\text{drive}} = U^\dagger \tilde{H}_{\text{drive}} U = \frac{A}{2}\cos(\omega_d t + \varphi)\left[\frac{\Delta}{\omega_q}\sigma_x + \frac{\epsilon}{\omega_q}\sigma_z\right].$$

The qubit+driving Hamiltonian can be further simplyfied by a transformation into a frame rotating with the drive, by $U = \exp(i\omega_d t\sigma_z)$. Due to the explicit time-dependence of this transformation, an additional term in the transformed Hamiltonian is required to preserve the time-evolution of the system in the rotating basis, $H' = U^\dagger(t)HU(t) + i\hbar U^\dagger(t)dU(t)/dt$.

After simplification, the transformed Hamiltonian of the driven system becomes

$$\begin{aligned} H' = & \frac{1}{2}\hbar(\omega_q - \omega_d)\sigma_z + \\ & \frac{A}{4}\frac{\Delta}{\omega_q}\left[\cos(2\omega_d t + \varphi) + \cos(\varphi)\right]\sigma_x + \\ & \frac{A}{4}i\frac{\Delta}{\omega_q}\left[\sin(2\omega_d t + \varphi) - \sin(\varphi)\right]\sigma_y + \\ & \frac{A}{2}\frac{\epsilon}{\omega_q}\cos(\omega_d t + \varphi)\sigma_z, \end{aligned}$$

which is still explicitly dependent on time.

If the driving frequency is close to the qubit frequency, it can be argued that the time-dependent terms in H' will average out over one period of the slow dynamics of the qubit in the rotating frame and can thus be dropped. This is simplification is called the rotating wave approximation and yields

$$H^{\mathrm{RWA}} = \frac{1}{2}\hbar(\omega_q - \omega_d)\sigma_z + \frac{A}{4}\frac{\Delta}{\omega_q}\left[\cos(\varphi)\,\sigma_x + i\sin(\varphi)\,\sigma_y\right].$$

The Schrödinger equation associated with this time-independent Hamiltonian is solved by $U(t) = \exp(-iHt/\hbar)$, which is nothing more than a rotation of the qubit state vector in three dimensions,

$$U(t) = \exp(-i\vec{\Omega}t \cdot \vec{\sigma}/2), \qquad \vec{\Omega} = \begin{pmatrix} \frac{A\Delta}{2\hbar\omega_q}\cos(\varphi) \\ \frac{A\Delta}{2\hbar\omega_q}\sin(\varphi) \\ \omega_q - \omega_d \end{pmatrix}, \tag{2.17}$$

where $\vec{\Omega}$ defines the rotation axis and $\hbar\vec{\sigma}/2$ is the angular momentum operator of a spin 1/2 system.

When the drive is resonant with the qubit transition frequency, the state vector describes rotations around the x or y axis depending on the starting phase of the drive. The rotation frequency,

$$\Omega = |\vec{\Omega}| = A\Delta/2\hbar^2\omega_q \tag{2.18}$$

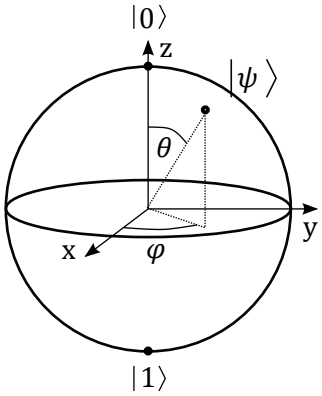

Figure 2.5: The Bloch Sphere. Pure ensembles are represented by a point on the surface of the sphere, mixed ensembles by a point in its interior. The azimuthal angle θ describes the energy content of the system, the polar angle ϕ the relative phase between the ground and excited state components.

is known as the Rabi frequency. When the drive is off-resonant, the state vector additionally precesses around the quantization axis of the rotating frame, and the rotation frequency is increased to

$$\Omega = \sqrt{\left(A\Delta/2\hbar^2\omega_q\right)^2 + \left(\omega_q - \omega_d\right)^2}, \tag{2.19}$$

called the generalized Rabi frequency. A qubit initially in its ground state $|\uparrow\rangle$ that is driven off-resonantly will never reach the excited state $|\downarrow\rangle$, because the rotation axis is tilted towards the z axis. By explicitly evaluating the rotation matrix corresponding to $\vec{\Omega}$, the minimum projection on the z axis can be found to be,

$$\langle\sigma_z\rangle_{\min} = \frac{(\omega_q - \omega_d)^2 - \left(\frac{A\Delta}{2\hbar\omega_q}\right)^2}{(\omega_q - \omega_d)^2 + \left(\frac{A\Delta}{2\hbar\omega_q}\right)^2}. \tag{2.20}$$

2.2.6 Bloch Sphere

The Bloch sphere[NC04] is an intuitive tool to visualize the evolution of the state vector of a two-level quantum system. Any such state can be

described by a superposition $|\psi\rangle = \alpha|\uparrow\rangle + \beta|\downarrow\rangle$, where α and β are complex numbers. Because $|\alpha|^2 + |\beta|^2 = 1$ must hold to insure normalization and because global phase factors of a wave function have no physical meaning, only two parameters remain,

$$|\psi\rangle = e^{-i\varphi/2}\cos(\theta/2)|\uparrow\rangle + e^{i\varphi/2}\sin(\theta/2)|\downarrow\rangle,$$

which can be understood as the azimuthal and polar angles of a point on the surface of a sphere, Fig. 2.5. The Bloch vectors corresponding to the eigenstates $|\updownarrow, x\rangle$ and $|\updownarrow, y\rangle$ of the σ_x and σ_y operators point, quite naturally, along the x and y axes.

The Bloch sphere can also visualize the density operator of an ensemble of two-level systems. The density operator of an ensemble of pure states is constructed $\rho = \sum_i p_i |i\rangle\langle i|$, where p_i is the probability of finding the system in state $|i\rangle$. Because this operator is Hermitian and the sum of the probabilities of finding the system in any of the states must be one, the operator can be decomposed into

$$\rho = \frac{1}{2}\left(\sigma_0 + \vec{r}\cdot\vec{\sigma}\right), \tag{2.21}$$

where σ_0 is the identity operator of a two-state system and $\vec{r}$ is a vector in $\mathbb{R}^3$ with $\vec{r}^2 \leq 1$, known as the Bloch vector. ρ describes a pure state, $\rho^2 = \rho$, if and only if $\vec{r}$ is a unit vector and consequently represents a point on the sphere. Mixed states are associated with points in the interior of the sphere. The components r_i of $\vec{r}$ are equal to the ensemble averages $\langle\sigma_i\rangle = \mathrm{Tr}\,(\rho\sigma_i)$ of the spin vector.

2.2.7 Qubit in a Dissipative Environment

In a closed system, the time-evolution of the density operator of a quantum-mechanical system is governed by the von Neumann equation[Sha94]

$$\frac{\partial\rho(t)}{\partial t} = -\frac{i}{\hbar}\left[H(t), \rho(t)\right]. \tag{2.22}$$

For a two-level system (qubit) with a density operator in the form Eq. 2.21 and the general time-dependent Hamiltonian $H(t) = \vec{\Omega}(t) \cdot \hbar\vec{\sigma}/2$, the von Neumann equation simplifies to

$$\left(\frac{\partial \vec{r}}{\partial t}\right) \cdot \vec{\sigma} = \left(\vec{\Omega} \times \vec{r}\right) \cdot \vec{\sigma}, \tag{2.23}$$

where the identity $(\vec{a} \cdot \vec{\sigma})(\vec{b} \cdot \vec{\sigma}) = (\vec{a} \cdot \vec{b})\sigma_0 + i\vec{\sigma} \cdot (\vec{a} \times \vec{b})$ was used and both sides were multiplied by 2. If $\vec{r}^2 = 1$ (ρ describes a pure state), Eq. 2.23 generates a rotation of the state vector identical to the rotation induced by the propagator Eq. 2.17.

The most general way to model a qubit coupled to its environment is by including the environmental and interaction terms in the system density operator ρ_{tot} and Hamiltonian H_{tot}. In most, if not all, interesting cases the solution of this task is infeasible both analytically and numerically. Under a number of conditions[Kos72]; [Lin76], this problem can be solved in a less computationally expensive way by explicitly adding dissipation terms to Eq. 2.22. The resulting equation is known as the Kossakowski–Lindblad equation or Lindblad master equation,

$$\frac{\partial \rho(t)}{\partial t} = -\frac{i}{\hbar}\left[H(t), \rho(t)\right] + \frac{1}{2}\sum_n L_n \rho(t) \tag{2.24}$$

where $\rho = \text{Tr}_{\text{env}}(\rho_{\text{tot}})$, $H = \text{Tr}_{\text{env}}(H_{\text{tot}})$, and

$$L_n \rho(t) = 2C_n \rho(t) C_n^\dagger - \rho(t) C_n^\dagger C_n - C_n^\dagger C_n \rho(t).$$

Coherent processes introduced by the environment are included in the reduced Hamiltonian H, incoherent processes are described by the L_n. The operators $C_n = \sqrt{\gamma_n} A_n$ are called collapse operators, with A_n being the operators through which the system interacts with its environment and γ_n being interaction rates.

In the case of a qubit, energy relaxation is modeled by the lowering operator, $C_1 = \sqrt{\gamma_1}\sigma_-$ and dephasing, being caused by fluctuations of the

level splitting, is modeled by $C_\phi = \sqrt{\gamma_\phi}\sigma_z$. Explicit evaluation of the L_n for a density matrix in the form Eq. 2.21 yields, after some algebra,

$$L_1\rho = -\gamma_1\left[\frac{1}{2}r_x\sigma_x + \frac{1}{2}r_y\sigma_y + (r_z - 1)\sigma_z\right]$$
$$L_\phi\rho = -\gamma_\phi\left[r_x\sigma_x + r_y\sigma_y\right].$$

From these expressions, one can already see that relaxation affects all three spin components while dephasing affects only the x and y components.

In the case of the qubit Eq. 2.23, the Lindblad master equation reads

$$\left(\frac{\partial\vec{r}}{\partial t}\right)\cdot\vec{\sigma} = \left(\vec{\Omega}\times\vec{r}\right)\cdot\vec{\sigma} - \left[\left(\frac{\gamma_1}{2}+\gamma_\phi\right)r_x\sigma_x + \left(\frac{\gamma_1}{2}+\gamma_\phi\right)r_y\sigma_y + \gamma_1(r_z-1)\sigma_z\right]. \quad (2.25)$$

When separated into the three spacial components by calculating the ensemble averages $\langle\sigma_i\rangle$, Eq. 2.25 reduces to the Bloch equations[Blo46],

$$\begin{aligned}\frac{\partial M_x}{\partial t} &= \gamma(\vec{M}\times\vec{B})_x - \frac{M_x}{T_2}\\ \frac{\partial M_y}{\partial t} &= \gamma(\vec{M}\times\vec{B})_y - \frac{M_y}{T_2}\\ \frac{\partial M_z}{\partial t} &= \gamma(\vec{M}\times\vec{B})_z - \frac{M_z - M_0}{T_1},\end{aligned} \quad (2.26)$$

of a spin 1/2 particle in a magnetic field if $\vec{M} = \gamma\vec{L} = \gamma\hbar\langle\vec{\sigma}\rangle/2$ and $\vec{B} = -\vec{\Omega}/\gamma$, where γ is the gyromagnetic ratio, are identified. The effect of the dissipation terms is obvious in this form. The $1/T_2$ terms in the first two equations result in an exponential decay of the x and y components of the spin expectation value towards 0 with a time constant of T_2. After an infinite time, a single measurement in these directions will return $\pm\hbar/2$ with equal probability. The $1/T_1$ term in the last equation results in a decay of the z component of the spin towards M_0/γ with time constant T_1. By not including excitation terms in the Lindblad equation zero temperature and a T_1 decay towards the spin up state was assumed,

and thus $M_0 = \gamma\hbar/2$. Further comparison of Eqns. 2.25 and 2.26 shows that the longitudinal relaxation time T_1 is the inverse of the interaction rate γ_1 and the transversal relaxation time $T_2 = \gamma_2^{-1} = (\gamma_1/2 + \gamma_\phi)^{-1}$ is a combination of both rates. In the absence of pure dephasing γ_ϕ is zero and the transversal relaxation time becomes $T_2 = 2T_1$.

2.3 Microwave Resonators

Microwave resonators are the second basic component used in this work. Resonators are linear resonant circuits built from resistors, inductors and capacitors that form an harmonic oscillator. In electrical circuits, their main use is filtering – close to resonance, they pass or block signals in a chosen frequency range. In qubit circuits, this property can be used to reject environmental noise. Resonators also store energy in their inductor and capacitor. This is exploited in quantum information devices to store qubit states and transfer them between different qubits that are connected to the same resonator. In this section, the steady-state electronic properties of microwave resonators will be reviewed from a classical point of view. The dynamics of qubit-resonator systems in the quantum regime will be discussed in the following section 2.4.

2.3.1 Series and Parallel Resonant Circuits

Close to its resonant frequency, the electrical response of any resonator can be modeled by either a serial or a parallel combination of a resistor R, inductor L and capacitor C. Schematics of these two cases are shown in Fig. 2.6 a) and b).

The impedance Z seen at the terminals of a series RLC circuit depends on the frequency of the input signal according to

$$Z = R + i\omega L - i\frac{1}{\omega C}. \tag{2.27}$$

The expression for parallel RLC circuits is very similar if the admittance $Y = Z^{-1}$ instead of the impedance of the device is considered,

$$Z^{-1} = \frac{1}{R} - i\frac{1}{\omega L} + i\omega C \tag{2.28}$$

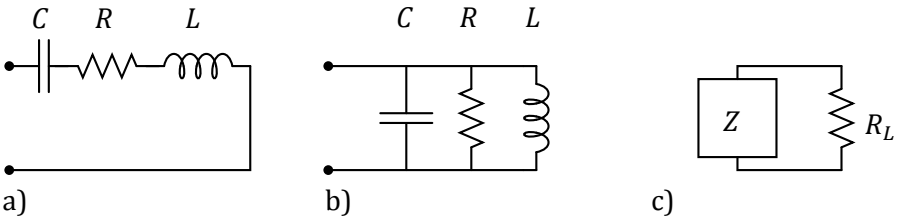

Figure 2.6: Schematics of a) a series RLC circuit, b) a parallel RLC circuit and c) a circuit connected to an external load.

In both cases, resonance occurs at $\omega_0 = 1/\sqrt{LC}$, where Z becomes real.

An important parameter of a resonant circuit is its quality factor Q. Higher Q means lower loss and increased lifetime of photons inside the resonator. It is defined as[Poz05]

$$Q = \omega \frac{\text{energy stored in the resonator}}{\text{rate of energy loss from the resonator}}.$$

To be useful in applications, the resonator must be coupled to some external circuitry, depicted as a load resistor R_L in Fig. 2.6 c). One distinguishes between loss caused by dissipation inside the resonator and loss due to the coupling. Loss caused by dissipation inside the resonator is characterized by the ''internal'' or ''unloaded'' quality factor Q_0. Loss caused by the coupling is characterized by the ''external'' quality quality factor Q_e. The combined loss is characterized by the ''loaded'', quality factor Q_L. Evidently, Q_L can be calculated from $Q_L^{-1} = Q_0^{-1} + Q_e^{-1}$. The ratio between Q_0 and Q_e the is known as the coupling factor κ. Using κ, the conversion between the various Qs is achieved by $Q_0 = \kappa Q_e = (\kappa + 1)Q_L$. In the cases of $\kappa < 1$, $\kappa = 1$ and $\kappa > 1$, the resonator is called undercoupled, critically coupled and overcoupled, respectively.

At resonance, the average energy stored in the inductor and capacitor are equal and their total equals $E = L\langle I_L^2 \rangle = C\langle V_C^2 \rangle$. In the model circuits of Fig. 2.6, internal loss is affected by dissipation inside the internal resistor, $W = R\langle I_R^2 \rangle = \langle V_R^2 \rangle / R$, and external loss by dissipation inside the load

resistor. In the case of series RLC circuits, the currents I_L and I_R are equal, and the internal and external quality factors and the coupling factors are

$$Q_0 = \frac{\omega_0 L}{R} = \frac{1}{\omega_0 RC}, \qquad Q_e = \frac{\omega_0 L}{R_L} \qquad \text{and} \qquad \kappa = \frac{R_L}{R}. \tag{2.29}$$

In the case of parallel RLC circuits, the voltages V_C and V_R are equal, resulting in

$$Q_0 = \frac{R}{\omega_0 L} = \omega_0 RC, \qquad Q_e = \frac{R_L}{\omega_0 L} \qquad \text{and} \qquad \kappa = \frac{R}{R_L}.$$

For $|\omega - \omega_0| \ll \omega_0$, the expressions 2.27 and 2.28 can be simplified to

$$Z \approx R\left(1 + 2iQ_0\frac{\omega - \omega_0}{\omega_0}\right) = R(1 + 2iQ_0\delta) \tag{2.30}$$

in the case of series circuits and

$$Z^{-1} \approx \frac{1}{R}\left(1 + 2iQ_0\frac{\omega - \omega_0}{\omega_0}\right) = \frac{1}{R}(1 + 2iQ_0\delta) \tag{2.31}$$

in the case of parallel circuits. In these expressions, the normalized frequency deviation from resonance $\delta = (\omega - \omega_0)/\omega_0$ was introduced. In both cases, the expression for lossy resonators can be obtained from the corresponding expressions for lossless resonators (not explicitly shown) through the substitution of ω_0 by $\omega_0(1 + i/2Q_0)$. It is often useful to express Eqns. 2.30 and 2.31 in terms of the load impedance R_L and the quality factors Q_0 and Q_e, as these quantities are more easily accessible by measurement,

$$Z \approx R_L\left(\frac{Q_e}{Q_0} + 2iQ_e\delta\right), \tag{2.32}$$

$$Z^{-1} \approx \frac{1}{R_L}\left(\frac{Q_e}{Q_0} + 2iQ_e\delta\right). \tag{2.33}$$

2.3.2 Transmission Lines

In DC electronics, a wire is just a conductor that connects two components, equalizing the voltages on both ends wire. At high frequencies, this is no

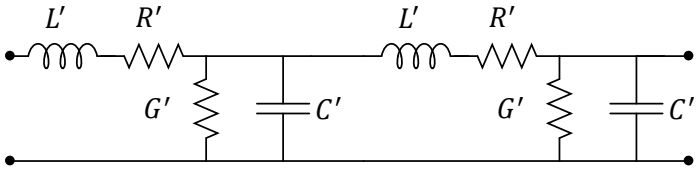

Figure 2.7: Lumped element model of a piece of transmission line. L' and C' define the characteristic impedance of the line, R' and G' introduce conductor and dielectric loss.

longer true: once the length of a wire becomes a considerable fraction of the wave length of the electrical signal it carries, the variation of current and voltage along it must be considered, it becomes a circuit component. In microwave engineering, a wire (or rather a pair of wires where one is the voltage reference for the other) is called a transmission line and has a variety of uses apart from simply carrying a signal between components. Among other things, it can be used as a phase shifter, impedance converter, filter and, as we will see, a resonator. In fact, the lowest-loss resonators that can be realized in planar circuits are based on superconducting transmission lines.

Electromagnetic waves propagate along a transmission line according to the Telegrapher's equations[Poz05],

$$\begin{aligned}\frac{dV(z)}{dz} &= -(R' + i\omega L')I(z),\\ \frac{dI(z)}{dz} &= -(G' + i\omega C')V(z),\end{aligned}$$

where R' and L' are the resistance and inductance of the line per unit length, and C' and G' are the capacitance and conductance of the signal conductor to the reference conductor of the line, as shown in Fig. 2.7.

These two equations are solved simultaneously by plane waves

$$\begin{aligned}V(z) &= V_0^+ \exp(-\gamma z) + V_0^- \exp(\gamma z),\\ I(z) &= I_0^+ \exp(-\gamma z) - I_0^- \exp(\gamma z),\end{aligned} \tag{2.34}$$

where

$$\gamma = \alpha + i\beta = \sqrt{(R' + i\omega L')(G' + i\omega C')}$$

is called the complex propagation constant. Its real part α represents voltage loss through dissipation in the resistors R' and leakage of current to the ground conductor through G'. Its imaginary part β is the wave vector of the electromagnetic radiation on the line. In the case of a lossless line

$$\frac{\omega}{v_p} = \beta = \omega\sqrt{L'C'} \quad \Rightarrow \quad v_p = 1/\sqrt{L'C'} \tag{2.35}$$

yields the phase velocity on the line.

The ratio of voltage to current that the line requires a wave travelling in a certain direction to have is its characteristic impedance,

$$\frac{V_0^+}{I_0^+} = \frac{V_0^-}{I_0^-} \equiv Z_0 = \sqrt{\frac{R' + i\omega L'}{G' + i\omega C'}}. \tag{2.36}$$

If a load with an impedance of Z_L is attached to the end of the line, it defines a boundary condition for the wave which can cause reflections. The amplitude of these reflections is given by the voltage reflection coefficient,

$$\frac{V_0^-}{V_0^+} = \Gamma = \frac{Z_L - Z_0}{Z_L + Z_0}, \tag{2.37}$$

which can be derived from Kirchhoff's laws. In the special cases of an open or shorted line, the voltage reflection coefficient will be $+1$ or -1 respectively, indicating perfect reflection with a phase shift of zero or π. A load that satisfies $Z_L = Z_0$ is called a matched load and does not cause any reflections.

The superposition of the waves travelling forward and the reflected waves travelling backward results in an impedance that varies with the length l of line between the source and load according to the transmission line impedance equation,

$$Z(l) = Z_0 \frac{Z_L + Z_0 \tanh \gamma l}{Z_0 + Z_L \tanh \gamma l}. \tag{2.38}$$

2.3.3 Transmission Line Resonators

If multiple boundary conditions are introduced on a line, standing waves form between the points of reflection. Transmission line resonators with

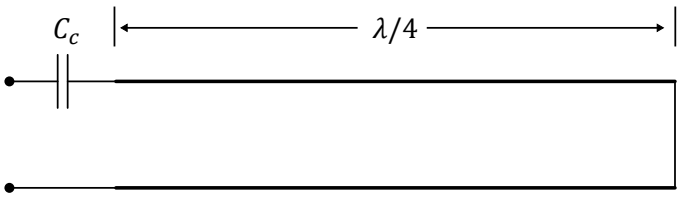

Figure 2.8: Schematic of a capacitively coupled $\lambda/4$ resonator.

high quality factors are built from a piece of line which is either open or shorted on both ends, insuring a voltage reflection coefficient very close to ± 1. Half-wave resonators have two identical boundary conditions, both ends shorted to ground or open, allowing standing waves with a length of $\lambda_k = 2l/(k+1)$, $k \in \mathbb{N}_0$. Quarter-wave resonators have converse boundary conditions, one open and one shorted end, supporting $\lambda_k = 4l/(2k+1)$.

Consider a piece of transmission line with propagation constant $\gamma = \alpha + i\beta$ that is shorted to ground at one end, similar to Fig. 2.8 but not coupled to external circuitry. A shorted end corresponds to a load impedance $Z_L = 0$ in Eq. 2.38, simplifying the normalized input impedance $z = Z(l)/Z_0$ to

$$\begin{aligned} z &= \tanh(\gamma l) \\ &= \frac{\tanh(\alpha l) + i\tanh(\beta l)}{1 + i\tanh(\alpha l)\tan(\beta l)} \\ &= \frac{1 - i\tanh(\alpha l)\cot(\beta l)}{\tanh(\alpha l) - i\cot(\beta l)}. \end{aligned}$$

We take the length l of the line to be $\lambda/4$ and study the response close to its first resonance ω_0. Using the dispersion relation Eq. 2.35 we can rewrite βl in terms of ω and $\omega_0 = \pi v_p/2l$,

$$\beta l = \frac{\omega l}{v_p} = \frac{\omega_0 l}{v_p} + \frac{(\omega - \omega_0)}{v_p} l = \frac{\pi}{2}\left(1 + \frac{\omega - \omega_0}{\omega_0}\right),$$

which allows an expansion of $\cot(\beta l) \approx -\pi(\omega - \omega_0)/2\omega_0$. In the case of a low-loss line $\alpha \ll 1$ and $\tanh(\alpha l) \approx \alpha l$ hold additionally, and therefore

$$z \approx \frac{1}{\alpha l + i\pi(\omega - \omega_0)/2\omega_0}.$$

This has the same form as the impedance of a lumped parallel RLC resonator. The parameters of the equivalent circuit can be found by comparing the above equation with Eq. 2.31 and using Eqns. 2.35 and 2.36:

$$R = \frac{Z_0}{\alpha l}, \qquad L = \frac{4Z_0}{\pi\omega_0} = \frac{8L'l}{\pi^2}, \qquad C = \frac{\pi}{4\omega_0 Z_0} = \frac{C'l}{2}. \tag{2.39}$$

Consider now a $\lambda/4$ piece of transmission line that is shorted at one end and coupled to a driving circuit through a capacitor C_c at the other end. To simplify the presentation, the line is assumed to be lossless. The normalized impedance of the series connection of capacitor and transmission line is

$$z = \frac{Z}{Z_0} = i\left[\tan\frac{\omega l}{v_p} - \frac{1}{b_c}\right],$$

where we introduced the normalized admittance $b_c = \omega C_c Z_0$ of the coupling capacitor and used the dispersion relation Eq. 2.35. Resonance occurs when $\operatorname{Im} z = 0$, at the solutions ω_n of $\tan(\omega l/v_p) = b_c^{-1}$. The response close to resonance can be found by expanding z in a Taylor series around ω_n,

$$z = z(\omega_n) + \left(\frac{dz}{d\omega}\right)_{\omega=\omega_n} (\omega - \omega_n) + O(\omega^2).$$

For the lowest resonant frequency,

$$\left(\frac{dz}{d\omega}\right)_{\omega=\omega_0} = i\left[\frac{l}{v_p}\left(1 + \tan^2\frac{\omega_0 l}{v_p}\right) + \frac{1}{\omega_0 b_c}\right] = i\frac{\pi}{2\omega_0}\left[b_c^{-2} + \frac{2}{\pi}b_c^{-1} + 1\right],$$

where a weak coupling of the resonator to the circuit, $b_c \ll 1$, corresponding to a nearly open end, and consequently $\omega_0 \approx \pi v_p/2l$ was assumed. Keeping only the b_c^{-2} term, the normalized impedance simplifies to

$$z \approx i\frac{\pi}{2b_c^2}\frac{\omega - \omega_0}{\omega_0},$$

which is equal to the impedance of a series RLC circuit, Eq. 2.30. In contrast to the uncoupled resonator, which looks like a parallel RLC circuit at resonance, the capacitively coupled resonator loads the driving circuit like a series RLC circuit.

As mentioned in section 2.3.1, internal loss can be added for high-Q resonators by replacing $\omega_0 \rightarrow \omega_0(1 + i/2Q_0)$,

$$z \approx \frac{\pi}{4Q_0 b_c^2} + i\frac{\pi}{2b_c^2}\frac{\omega - \omega_0}{\omega_0}, \tag{2.40}$$

which is equal to the Eq. 2.30, if R in that equation is identified with $\pi/4b_c^2 Q_0$.

2.3.4 Circuit Characterization using S Parameters

The behavior of linear electrical networks with multiple two-terminal pairs, called ports, can be described in a variety of ways. In the previous section, a description using the impedance seen at the terminals of a single-port network, relating voltage to current at the input, was used. Using the definition $V_i = Z_{ij}I_j$, this concept extends naturally to a network with multiple ports. By inverting this relation, $I_i = Y_{ij}V_j$, one can also characterize the network in terms of admittances. These two definitions are equivalent, and the impedance and admittance matrices are linked by $Y = Z^{-1}$. While the Z and Y matrices provide an intuitive understanding of the network, their accurate measurement poses difficulties at microwave frequencies.

An alternative characterization of a multiport network that can be more easily measured is through its scattering parameters. The scattering description ties the amplitudes and phases of waves originating from the network to waves incident on the network and can be formulated in terms of voltage waves, current waves or a mixture of both. The complex voltage amplitudes V_i^- of waves originating from port i are tied to the amplitudes V_j^+ incident on port j of the network by the scattering matrix S via $V_i^- = S_{ij}V_j^+$. Matrix element S_{ij} is found by measuring V_i^+ while driving V_j^- and making sure that there are no incident waves on the other ports. This also means that waves originating from the other ports must

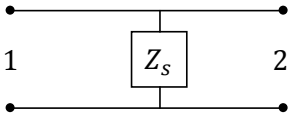

Figure 2.9: Schematic of an impedance Z_s shunting a transmission line to ground.

not be reflected back to the port, which is realized by terminating them with matched loads.

In the simple case of a single-port network,

$$V_1^- = S_{11} V_1^+,$$

S_{11} is equal to the voltage reflection coefficient Γ, Eq. 2.37, introduced in the previous section. In case of a two-port network,

$$\begin{pmatrix} V_1^- \\ V_2^- \end{pmatrix} = \begin{pmatrix} S_{11} & S_{12} \\ S_{21} & S_{22} \end{pmatrix} \begin{pmatrix} V_1^+ \\ V_2^+ \end{pmatrix}.$$

S_{11} and S_{22} are the reflection coefficients at port one and two when the other port is terminated with a matched load and S_{21} and S_{12} are the transmission coefficients from port one to port two and vice versa. It can be shown that S matrices of reciprocal networks are symmetric and those of lossless networks are unitary.

The Z, Y and S parameters are equivalent inasmuch as any of these matrices can be calculated from any other one. Our theoretical models are typically formulated in terms of impedances, but the measurement equipment records the S parameters. In the case of two-port networks, the conversion from Z to S is realized by[Poz05],

$$\begin{aligned} S_{11} &= \left[(Z_{11} - Z_0)(Z_{22} + Z_0) - Z_{12}Z_{21}\right]/\Delta Z \\ S_{12} &= 2Z_{12}Z_0/\Delta Z \\ S_{21} &= 2Z_{21}Z_0/\Delta Z \\ S_{22} &= \left[(Z_{11} + Z_0)(Z_{22} - Z_0) - Z_{12}Z_{21}\right]/\Delta Z \\ \Delta Z &= (Z_{11} + Z_0)(Z_{22} + Z_0) - Z_{12}Z_{21} \end{aligned} \tag{2.41}$$

An interesting special case is the response of a transmission line with a shunt impedance to ground. The characteristic impedance of the line is

Z_0 and the shunt impedance is Z_s. The Z matrix of this network is simply $Z_{11} = Z_{12} = Z_{21} = Z_{22} = Z_s$. Using Eqns. 2.41, the scattering matrix of the shunt becomes

$$S_{11} = S_{22} = \frac{-1}{1 + 2Z_s/Z_0} \tag{2.42}$$

$$S_{12} = S_{21} = \frac{1}{1 + Z_0/2Z_s}. \tag{2.43}$$

2.3.5 Resonator Characterization

A circuit topology involving a single feedline with multiple resonant shunts is very suitable to characterize a large number of high-Q resonators simultaneously. For our experiments, we designed a series of $\lambda/4$ transmission line resonators capacitively coupled to a common line. The response of a single such resonator coupled to a feedline can be derived by combining Eq. 2.30 with Eqns. 2.42 and 2.43,

$$S_{21} = 1 + S_{11} = 1 + \frac{-1}{1 + 2r + 4irQ_0\delta}, \tag{2.44}$$

where $r = R/Z_0$ is the loss resistance normalized to the impedance of the feedline. Using Eq. 2.29, this can be expressed in terms of the loaded and internal quality factors,

$$S_{21} = \frac{Q_0^{-1} + 2i\delta}{Q_L^{-1} + 2i\delta}. \tag{2.45}$$

These expressions for S_{11} and S_{21} could be fitted against measured data to find the quality and coupling factors of each resonator. However these factors can also be extracted from the measurements of only a few points on the response curve[KG83]; [BR04].

A measurement of the amplitude of the minimum of transmission at resonance yields κ,

$$S_{21_r} = \frac{2r}{1 + 2r} = \frac{1}{1 + \kappa} \Leftrightarrow \kappa = \frac{1 - S_{21_r}}{S_{21_r}}, \tag{2.46}$$

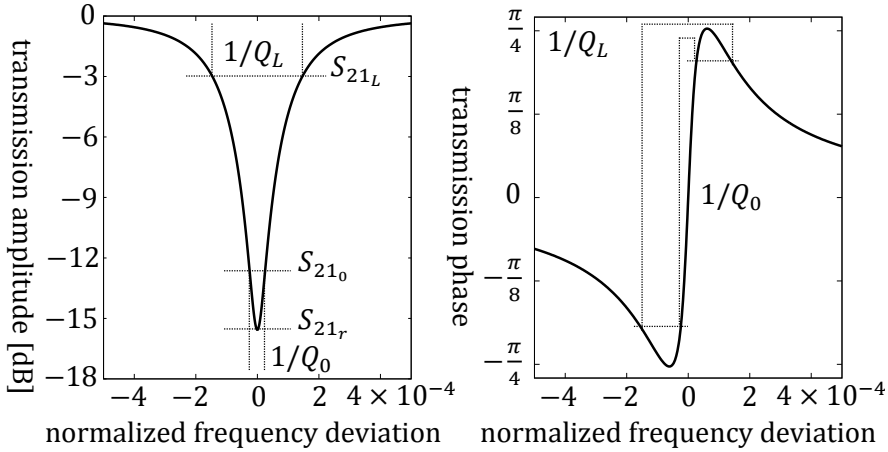

Figure 2.10: Transmission amplitude and phase response of a feedline shunted by a resonator. If $\kappa \gg 1$, the loaded (unloaded) quality factor can be determined by measuring the 3 dB bandwidth from the top (bottom) of the amplitude graph. The transmitted phase at the loaded and unloaded 3 dB points is equal. Plot parameters are $Q_0 = 20000$, $Q_e = 4000$, resulting in $Q_L = 3333$ and $\kappa = 5$.

where Eq. 2.29 was used and R_L was identified with $Z_0/2$ because the shunt is connected to two parts of the feedline in parallel.

The internal quality factor Q_0 is equal to the inverse normalized bandwidth of the resonance curve at the point where the dissipated power in the internal resistance is half of its value at resonance. The half-power points are found when the reactance (the imaginary part of Eq. 2.30) of the resonator is equal to its loss resistance (the real part of Eq. 2.30), and hence at

$$|S_{21_0}| = S_{21_r}\sqrt{\frac{2}{1+S_{21_r}^2}}, \qquad \arg S_{21_0} = \pm \arctan\left(\frac{1-S_{21_r}}{1+S_{21_r}}\right). \quad (2.47)$$

In the case of overcoupled resonators with $\kappa \gg 1$ the $S_{21_r}^2$ term in the denominator can be neglected and the bandwidth measured at $\sqrt{2}$ times or 3 dB above the minimum $|S_{21_r}|$.

The loaded quality factor is found as the inverse normalized bandwidth at the points where the reactance of the resonator is equal to $R + R_L$, at

$$|S_{21_L}| = \sqrt{\frac{1 + S_{21_r}^2}{2}}, \qquad \arg S_{21_L} = \pm \arctan\left(\frac{1 - S_{21_r}}{1 + S_{21_r}}\right). \tag{2.48}$$

In the case of overcoupled resonators, the S_{21_r} term in $|S_{21_L}|$ is again negligible and the bandwidth can be measured at $1/\sqrt{2}$ times or 3 dB below the baseline of unity transmission. The loss rate Q_e^{-1} to the external circuit is best determined from

$$Q_e^{-1} = Q_L^{-1} - Q_0^{-1} \tag{2.49}$$

and is equal to the total loss rate Q_L^{-1} in the limit of strongly overcoupled resonators.

The points where the various quality factors are measured are shown schematically in Fig. 2.10. Analog expressions can be derived for S_{11} if the resonators are to be measured in reflection instead of transmission.

2.3.6 Parameters of Superconducting Transmission Lines

The most common transmission line geometries used in qubit circuits are the microstrip, stripline and coplanar types.

The microstrip[Poz05], is built just from a single conducting strip which is backed by a ground plane at a controlled distance, typically at the back side of the chip substrate. The signal and ground conductors being on different sides of the substrate allows layouts of many circuit elements, such as branches and couplers, on a single signal layer. Because width is roughly equal to the thickness of the substrate at an impedance of 50 Ω on silicon, microstrips tend to be bulkier than other geometries. This also increases the spatial extent of their electric and magnetic fields, favoring crosstalk and making the housing a part of the circuit.

The latter two handicaps are avoided by the stripline, which adds a second substrate and groundplane to the circuit, confining the fields between the two grounds. Due to the second substrate, it is more complex to manufacture.

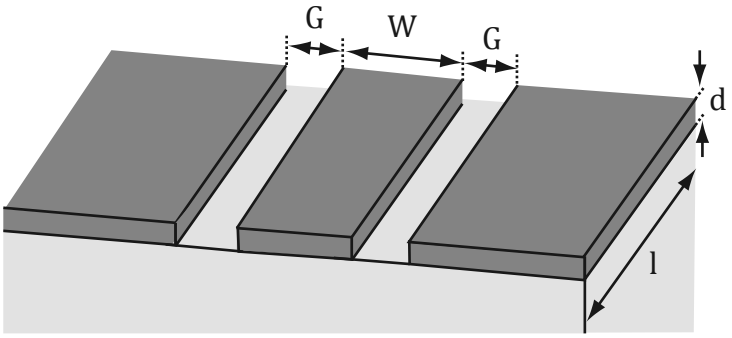

Figure 2.11: Sketch of a coplanar waveguide geometry.

In a coplanar geometry, shown in Fig. 2.11, the signal and two ground strips reside in the same layer. The structures can be made arbitrarily small by reducing the lateral distance between the signal and ground strips, which keeps the electromagnetic fields local although they are not explicitly confined. Because of these features, all our resonators are based on coplanar transmission lines.

Assuming that the signal strip is narrow compared to the height of the substrate and the distance to the housing, the parameters of a coplanar line are approximated by[Sim01],

$$\begin{aligned} C' &= 4\epsilon_0\epsilon_{\text{eff}}\frac{K(k_0)}{K(k_0')}, \\ L' &= \frac{\mu_0}{4}\frac{K(k_0')}{K(k_0)}, \\ Z_0 &= \sqrt{\frac{L'}{C'}} = \frac{\mu_0 c}{4\sqrt{\epsilon_{\text{eff}}}}\frac{K(k_0')}{K(k_0)}, \end{aligned} \tag{2.50}$$

with $k_0 = W/(W + 2G)$, $k_0' = \sqrt{1 - k_0^2}$ and K being complete elliptic integrals of the first kind, and $\epsilon_{\text{eff}} = (\epsilon_r + 1)/2$ being the effective dielectric constant defining the speed of signal propagation along the line.

A typical CPW used in our experiments may have a center strip width of $W = 20$ µm and gap widths of $G = 11$ µm between the center strip and

ground planes and be situated on top of a Silicon substrate with $\epsilon_r = 11.9$. This results in $C' = 155\,\mathrm{fF/mm}$, $L' = 425\,\mathrm{pH/mm}$ and a characteristic impedance of $50\,\Omega$.

The above geometric inductance and capacitance store energy in magnetic and electric fields and a polarization of the substrate. Additionally, energy can be stored in the motional degrees of freedom of the charge carriers. In normal metals, the scattering time of the carriers is too short to store and retrieve a significant amount of kinetic energy. In superconductors, however, scattering of the Cooper pairs is suppressed by a lack of low-energy states due to the energy gap, giving rise to an additional "kinetic" inductance term.

Inserting a harmonic time dependence into the first London equation[LL35] yields

$$\vec{E} = i\omega\mu_0\lambda_L^2\vec{j}_s,$$

where λ_L is the London penetration depth. Integrating this equation over a slab of superconductor with length l and cross-section Wd results in

$$V = i\omega\frac{\mu_0\lambda_L^2 l}{Wd}I_s = i\omega L_k I_s.$$

Since the current is delayed by 90° with respect to the voltage, the fraction can be interpreted as an inductance[Wün05].

For Nb films and at Millikelvin temperatures, a typical value for λ_L is 90 nm[Hyp08]. For the above geometry, kinetic inductance contributes an additional $L_k' = L_k/l = 3\,\mathrm{pH/mm}$ at a film thickness of 150 nm. This affects a relative frequency shift of $3\cdot10^{-3}$ of transmission line resonators, which is not significant for the design of our circuits.

The penetration depth changes with the temperature of the sample, following $\lambda(T) = \lambda(0)/\sqrt{1-(T/T_c)^4}$[EH00]. This causes a noticeable frequency difference between LHe temperature ($\approx T_c/2$) and Millikelvin measurements but does not affect temperature resolved measurements below $1\,K$.

2.4 Circuit Quantum Electrodynamics

2.4.1 Interaction of Light and Matter

Quantum electrodynamics, QED for short, is the quantum version of classical electrodynamics. It describes the interaction of particles with an electromagnetic field. QED is best known for its extremely accurate predictions of atomic properties such as the gyromagnetic ratio of the free electron[KF48] and the Lamb shift of the Hydrogen atom[LR47].

Cavity QED is a subset of QED that is concerned with the interaction of matter with light confined in a cavity. The presence of the cavity walls selects an infinite but discrete set of modes that can interact with a trapped atom. Choosing the right parameters, a single relevant mode of the field and a single relevant atomic transition can be selected, resulting in a system characterized by the Jaynes-Cummings model[JC63].

For a cavity QED system to be interesting for quantum information processing, it must reach the so-called strong coupling limit. In this limit, the lifetimes of the atomic state, the photonic state and the strength of the atom-cavity interaction are large enough so that the atomic and photonic states can be coherently exchanged through a process called vacuum Rabi oscillations. Using this process, an entanglement of the atom and cavity can be created and transferred to a second atom passing through the cavity at a later time. Also, the non-resonant interaction allows a weak measurement of the cavity state by observing the state of the atom and vice versa[RH01].

Finally, circuit QED is a special realization of cavity QED. Where cavity QED employs a three dimensional cavity and a beam of single atoms flying through it, circuit QED uses a (typically two dimensional) cavity realized by patterning a superconducting thin film and a superconducting qubit next to it. This approach generally makes it easier to reach large coupling strengths and therefore faster operation times, but suffers from the lower lifetimes of artificial atoms in a solid-state environment when compared to free single atoms[BHW+04]. In princple however, cavity QED could also be used as a bridge between superconducting qubits and natural atoms, if both were coupled to the same cavity mode.

2.4.2 Coupling of Transmission Line Resonators to Flux Qubits

The most straightforward way to couple a flux qubit to a transmission line resonator is by coupling the magnetic fields generated by the qubit and resonator. Viewed from the perspective of the qubit, the coupled resonator introduces a driving field that is proportional to σ_z in the basis of the persistent current states. The treatment of this interaction is similar to the discussion of section 2.2.5, with the difference that the driving field is itself a quantized field generated by the current operator of the relevant mode of the resonator instead of a classical field.

An inductive qubit-resonator coupling is a magnetic dipole interaction of the magnetic moment μ_q of the persistent current flowing around the qubit loop with the magnetic field B_r generated by the resonator at the qubit site. This adds a potential energy term $U_{\text{int}} = -\mu_q B_r = I_p A_q B_r$ to the system, where I_p is the persistent current flowing around the qubit loop and A_q is the loop area. In terms of the mutual inductance $M_{r,q} = B_r A_q / I_r$, defined as the magnetic flux that enters the qubit loop per unit current in the resonator, it becomes $U_{\text{int}} = -M_{r,q} I_p I_r$.

Each mode of the resonator, represented by its lumped element model, is described as a separate linear harmonic oscillator with Hamiltonian $H_r = \hbar\omega_k(a_k^\dagger a_k + 1/2)$. The charge on the lumped capacitor is defined by the position operator $x = Q_{0,k}(a_k^\dagger + a_k)$ and the current in the inductor by the momentum operator $p_k = iI_{0,k}(a_k^\dagger - a_k)$. $Q_{0,k}$ and $I_{0,k}$ are the zero-point charge and current fluctuations and can be calculated classically from

$$Q_{0,k}^2/2C = I_{0,k}^2/2L = \hbar\omega_k/2. \tag{2.51}$$

$M_{r,q}$ and $I_{0,k}$ are sufficient to determine the coupling to a lumped element resonator, but in the case of the transmission line resonator the mode-dependent distribution of the zero-point current has to be taken into account. The solutions for the voltage and current waves, Eq. 2.34, on a quarter-wave resonator in a lossless line shorted at $z = 0$ are

$$V_{0,k}(z) = Z_0 I_{0,k} \sin\left[(2k+1)\beta z\right],$$
$$I_{0,k}(z) = -I_{0,k} \cos\left[(2k+1)\beta z\right].$$

Any mode shows a current maximum at the shorted end at $z = 0$ and a minimum at the open end at $z = \lambda/4$, and the harmonics show k

additional current minima and maxima. Typically, qubits are placed close to a maximum of the current distribution for maximum coupling, but other locations may be desired for example to realize a certain hierarchy of coupling strengths to different modes of the resonator.

Taking only a single relevant mode into account and identifying I_0 with the zero-point current at the qubit site, the interaction Hamiltonian between the qubit and resonator takes the form

$$\tilde{H}_{\text{int}} = M_{r,q} I_p I_0 \, i(a^\dagger - a) \, \tilde{\sigma}_z$$

in the persistent current basis of the qubit. The unitary rotation described by Eq. 2.12 transforms $\tilde{H}_{\text{int}}$ into the energy eigenbasis of the qubit,

$$H_{\text{int}} = M_{r,q} I_p I_0 \, i(a^\dagger - a) \left[\frac{\Delta}{\hbar\omega_q} \sigma_x + \frac{\epsilon}{\hbar\omega_q} \sigma_z \right]. \tag{2.52}$$

Using the mixing angle θ, defined in 2.12, the Hamiltonian becomes

$$H_{\text{int}} = M_{r,q} I_p I_0 \, i(a^\dagger - a) \left[\sin(2\theta)\sigma_x + \cos(2\theta)\sigma_z \right].$$

At the qubit symmetry point $\theta = \pm\pi/2$ and the coupling is purely transversal, allowing a photon exchange between the qubit and the coupled system. With increasing asymmetry, the coupling acquires an additional longitudinal component, which allows the realization of a controlled phase gate. For large asymmetries, the transversal coupling diminishes and only the longitudinal coupling is relevant. The product of constants

$$\hbar\tilde{g} = M_{r,q} I_p I_0 \tag{2.53}$$

is called the bare coupling energy. The actual transversal coupling is

$$\hbar g = \hbar\tilde{g} \sin(2\theta) \tag{2.54}$$

and changes with the asymmetry of the qubit.

2.4.3 The Jaynes-Cummings Hamiltonian

The quantum Hamiltonian of a cavity QED system is[SZ97],

$$\begin{aligned} H &= H_{\text{cavity}} + H_{\text{qubit}} + H_{\text{int}} + H_\kappa + H_\gamma, \\ H_{\text{cavity}} &= \hbar\omega_r(a^\dagger a + \frac{1}{2}), \\ H_{\text{qubit}} &= \hbar\omega_q\sigma_z, \\ H_{\text{int}} &= \hbar g(\sigma_+ - \sigma_-)(a - a^\dagger). \end{aligned} \tag{2.55}$$

Here, ω_r is the angular oscillation frequency of the relevant cavity mode, $\hbar\omega_q$ is the energy difference of the two qubit levels and $\hbar g$ describes the strength of interactions between the cavity and qubit subsystems. The terms H_κ and H_γ mediate relaxation and dephasing of the cavity and qubit, respectively, through coupling to an external bath. The transversal component of the interaction term Eq. 2.52 found for the flux qubit can be transformed into H_{int} of the Jaynes-Cummings model using the identity $\sigma_x = \sigma_+ + \sigma_-$ and a rotation. The interaction Hamiltonian is commonly simplified using the rotating wave approximation, equivalent to dropping the $\sigma_+a^\dagger$ and σ_-a terms of the product, with the same arguments made for a driven qubit in section 2.2. The resulting interaction term $H_{\text{int}} = \hbar g(\sigma_+a + \sigma_-a^\dagger)$ can be interpreted as a coherent exchange of excitations between the qubit and cavity.

Exact diagonalization of the Jaynes-Cummings Hamiltonian in the rotating wave approximation and with the decoherence terms H_κ and H_γ neglected yields the gound state $|\uparrow, 0\rangle$ and dressed states[BHW+04]

$$\begin{aligned} |+, n\rangle &= \cos\vartheta_n|\downarrow, n\rangle + \sin\vartheta_n|\uparrow, n+1\rangle, \\ |-, n\rangle &= -\sin\vartheta_n|\downarrow, n\rangle + \cos\vartheta_n|\uparrow, n+1\rangle. \end{aligned}$$

Here, $|\updownarrow, n\rangle = |\updownarrow\rangle \otimes |n\rangle$ are the basis states of the bare qubit and cavity system(s) and

$$\tan(2\vartheta_n) = \frac{2g\sqrt{n+1}}{\omega_{rq}}$$

is a mixing angle between the two subsystems. The parameter $\omega_{rq} \equiv \omega_q - \omega_r$ is the detuning of the atom from the cavity and is a key parameter

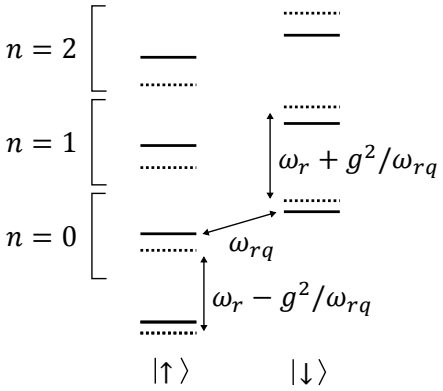

Figure 2.12: Energy levels of the Jaynes-Cummings Hamiltonian in the dispersive regime, $\omega_{rq} \gg g$. The transition frequency between two adjacent cavity levels is increased or decreased by the coupling to the qubit depending on the qubit state. The energy difference between the qubit states also changes linearly with increasing cavity photon numbers.

of the dynamics of the system. The eigenenergies corresponding to these states are

$$\begin{aligned} E_{\uparrow,0} &= -\frac{\hbar\omega_{rq}}{2}, \\ E_{\pm,n} &= (n+1)\hbar\omega_r \pm \frac{\hbar}{2}\sqrt{4g^2(n+1)+\omega_{rq}^2}. \end{aligned} \tag{2.56}$$

In the limit of vanishing detuning, $\omega_{rq} = 0$, of the uncoupled system, the $|+,n\rangle$ and $|-,n\rangle$ states would be degenerate, but in the interacting system this degeneracy is lifted by $\Omega = 2g\sqrt{n+1}$. At the same time, the basis states dressed states $|\pm,n\rangle$ are equal superpositions of the $|\downarrow,n\rangle$ and $|\uparrow,n+1\rangle$ states with opposite phases and vice versa. Therefore, an initial state prepared as $|\downarrow,n\rangle$ will evolve into $|\uparrow,n+1\rangle$ and back at a rate of $\Omega/2\pi$, which is called the vacuum Rabi frequency. Because of the $\sqrt{n+1}$ term in the Rabi frequency, the time required to exchange the one excitation becomes smaller with increasing number of excitations inside the cavity.

In the opposite limit of large detuning, $\omega_{rq} \gg g$, the dressed states become equivalent to the basis states of the uncoupled system with first

order corrections in g/ω_{rq}. The expansion of the energy levels, 2.56, to first order in ω_{rq}, provides more insight into this regime.

On one hand, the coupling term renormalizes the transition frequency between the qubit ground and excited states[AT55],

$$E_{+,n} - E_{-,n-1} = \hbar\omega_q + \frac{\hbar g^2}{\omega_{rq}}(2n+1), \tag{2.57}$$

which is called the ac Stark or ac Zeeman shift depending on whether g arises from electric or magnetic interaction, respectively. A fit of the qubit transition frequency versus the driving power of the cavity can be used to calibrate the driving necessary to occupy the cavity with a desired average photon number. Because the photon loss rate of the cavity is proportional to the number of photons inside the cavity, the relation between the two is linear.

On the other hand, the term also introduces a shift of the transition frequency between successive cavity levels,

$$\begin{aligned} E_{+,n} - E_{+,n-1} &= \hbar\omega_r + \frac{\hbar g^2}{\omega_{rq}}, \\ E_{-,n} - E_{-,n-1} &= \hbar\omega_r - \frac{\hbar g^2}{\omega_{rq}}, \end{aligned} \tag{2.58}$$

which depends on the state of the qubit.

2.4.4 Dispersive Readout

The state-dependent shift Eq. 2.58 of the cavity transition frequency can be used to determine the qubit state. This so-called dispersive readout is realized by driving the cavity with microwave radiation and observing the reflected or transmitted waves.

From the classical treatment of resonators in section 2.3, it is clear that the amplitude and phase of microwaves scattered at a cavity depends strongly on the normalized frequency difference δ of the driving and resonance frequencies. To determine whether the resonator is shifted up or down in frequency, that is, to determine the state of the qubit, it is thus sufficient to measure the amplitude or phase of a single element of the

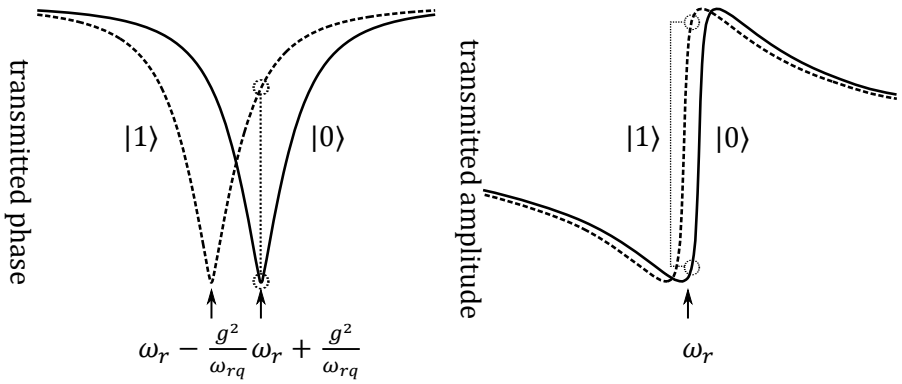

Figure 2.13: Classical interpretation of dispersive readout. The cavity is probed by a microwave signal and the amplitude or phase of an element of the transmitted or reflected signal is measured. If the dispersive shift is of the order of a line width or more, an amplitude measurement at one of the dispersively shifted frequencies gives the largest contrast. If the dispersive shift is much smaller than the line width, the phase signal at the bare cavity frequency is measured instead.

scattering matrix at a fixed frequency. Which type of measurement yields the best readout contrast depends on the coupling layout of the resonator to the readout line and the loss rates of the resonator. The case of a resonator connected to the readout line in series is treated in [BHW+04]. Here, we consider instead the case of a resonant shunt connected to a feedline.

The response of the feedline measured in reflection is essentially equal to the response of a series connected resonator measured in transmission. The width of the resonance peak is determined by the total loss rate $\kappa_L = \omega/Q_L$ (not to be confused with the dimensionless coupling factor κ). If $\kappa_L < g^2/\omega_{rq}$, the peaks representing the two qubit states are separated. Measuring at one of the shifted frequencies gives close to perfect reflection in one state and low reflection in the other state. If $\kappa_L > g^2/\omega_{rq}$, the two peaks overlap and the amplitude contrast diminishes. In this case, a measurement of the reflected phase at the bare resonator frequency ω_r is more appropriate. If the feedline is measured in transmission, the width of the transmission dip is $\kappa_0 = \omega/Q_0$, which is much smaller than κ_L in

the case of an overcoupled resonator, so that an amplitude measurement at one of the shifted frequencies is optimal. These amplitude and phase measurements are compared schematically in Fig. 2.13.

The driving of the cavity can be modeled quantum-mechanically by plugging

$$H_{\text{drive}} = \frac{A(t)}{2}\left[a^\dagger \exp(-i\omega t) + a\exp(i\omega t)\right] \tag{2.59}$$

into the total Hamiltonian. Here, $A(t)$ is the amplitude and envelope of the readout pulse and ω is the driving frequency. The rate of state transitions under this driving can be derived by treating H_{drive} as a perturbation to the Jaynes-Cummings Hamiltonian and evaluating the transition matrix elements,

$$|\langle \pm, n+1|H_{\text{drive}}|\mp, n\rangle| \approx \frac{A}{2}\frac{g}{\omega_{rq}},$$
$$|\langle \pm, n+1|H_{\text{drive}}|\pm, n\rangle| \approx \frac{A}{2}.$$

The first transition, describing a bit-flip processes, is suppressed by g/ω_{rq} with increasing detuning. The second transition, corresponding to the addition or subtraction of a photon to or from the cavity, is not suppressed. In both cases, the assumption $n \ll n_{\text{crit}} = \omega_{rq}^2/4g^2$ was used when expanding $\cos\theta_n$ and $\sin\theta_n$.

In this limit, the Hamiltonian Eq. 2.55 can be expanded[BHW+04] in g/ω_{rq},

$$H \approx \hbar\left(\omega_r + \frac{g^2}{\omega_{rq}}\sigma_z\right)a^\dagger a + \frac{\hbar}{2}\left(\omega_q + \frac{g^2}{\omega_{rq}}\right)\sigma_z. \tag{2.60}$$

Dispersive readout probes σ_z via the dispersive shift $(g^2/\omega_{rq})\sigma_z \cdot a^\dagger a$. This term commutes with σ_z, so no uncertainty relation applies and the measurement of one of the quantities does not influence the other. In the absence of disspiation, σ_z additionally commutes with H, so it is a constant of motion. These two properties together insure that repeated measurements give the same result, making dispersive readout a so-called quantum non-demolition readout.

However, any measurement, even a non-demolition measurement, has some backaction on the quantum state of the qubit. When the cavity is

populated with photons in order to determine its shift, the frequency of the qubit transition is modulated and fluctuations of the cavity photon number dephase the qubit. In the standard realization of circuit QED, a serially connected cavity with input and output capacitors, it was shown that the dephasing rate exceeds the quantum limit by a factor of two[BHW+04] if only the photons leaving the cavity through the output capacitor are collected by the detector. This statement also holds in the present case of a cavity shunting a feedline, because the voltage wave emitted by the cavity travels in both directions of the line.

The amplitude of the waves emitted by the cavity is found by considering its power loss $P^-_{\mathrm{res}} = \kappa_e E$ into the feedline, where $E = \hbar\omega_r a^\dagger a$ is the energy stored in the cavity (neglecting zero-point fluctuations) and $\kappa_e = \omega_0/Q_e$ is the loss rate through the coupling capacitor. From the point of view of the resonator, the two halves of the feedline are connected in parallel, presenting an impedance of $Z_0/2$ and making $P^-_{\mathrm{res}} = |V^-_{\mathrm{res}}|^2/(Z_0/2)$. The voltage V^-_{res} output by the cavity can thus be related to the cavity operators,

$$\langle V^-_{\mathrm{res}}\rangle = \sqrt{\hbar\omega_r\kappa_e Z_0/2}\langle a\rangle.$$

If V_1^+ is the driving voltage applied at the feedline input, the total reflected and transmitted voltages emitted from the input and output ports are $V_1^- = V^-_{\mathrm{res}}$ and $V_2^- = V_1^+ + V^-_{\mathrm{res}}$, respectively. In the steady-state of an overcoupled resonator, $V_2^- \approx 0$ at resonance (Eq. 2.46) and thus $V^-_{\mathrm{res}} = -V_1^+$.

The mean steady-state population of the resonator resulting from classical driving voltage can be calculated from $E = L\,|I_{\mathrm{res}}|^2$. Expressing the current $I^+_{\mathrm{res}} = V_1^+/(Z + Z_0/2)$ in terms of the input voltage V_1^+ and using 2.29 to express L in terms of Z_0 and Q_e, the stored energy can be written

$$E = \frac{2|V_1^+|^2}{Z_0\kappa_e}\,\frac{Q_L^2 Q_e^{-2}}{1 + 4\delta^2 Q_L^2},$$

where δ is the normalized detuning of the resonator frequency including any shifts. By solving this expression for $|V_1^+|$, the voltage that must be applied to reach a desired cavity photon number can be determined. It is important to note that the energy stored in the cavity and therefore the number of photons decreases with $(1 + 4\delta^2 Q_L^2)^{-1}$ as the drive is detuned

from the center frequency of the cavity. Additional drives present on the feedline that are a few loaded linewidths from the center frequency do not cause an appreciable occupation of the cavity and do therefore not contribute to the dephasing of the qubit.

In the absence of relaxation, the Schrödinger equation of Eq. 2.60 including the driving term Eq. 2.59 can be solved analytically to find the time evolution the expectation value of $V_{\mathrm{res}}^{-}(t)$. In the presence of relaxation $V_{\mathrm{res}}^{-}(t)$ can be calculated by setting up the Master equation of the Hamiltonian and integrating it numerically for a given initial density matrix. Figure 2.14 shows simulated time traces of the cavity occupation numbers, in-phase and quadrature output voltages for the qubit in the ground and excited states.

2.5 Frequency-Division Multiplexing

2.5.1 Comparison of Multiplexing Techniques

Multiplexing is a method to transmit several logical communication channels over a single physical medium. A variety of multiplexing schemes exist, whose applicability depends on the characteristics of the signals to be transmitted, such as their bandwidth and digital or analog nature. The most widely used schemes are time-division multiplexing, frequency-division multiplexing and code-division multiplexing.

For digital signals, time-division multiplexing is the most straightforward approach. Several low-bitrate input channels are switched on and off the output channel in a round-robin fashion, with the rate of switching defining the bitrate on the output channel. To multiplex N inputs onto a single outputs, the switching rate must be at least N times larger than the bitrate of the individual inputs. Obvious drawbacks of time-division are that the signals at the inputs can not be sampled simultaneously without additional data buffers and that it is hard to implement for continuous analog signals, which would involve a compression of the signals in the time-domain.

In contrast, frequency-division multiplexing can easily combine continuous-time signals into a single medium. Frequency-division multiplexing

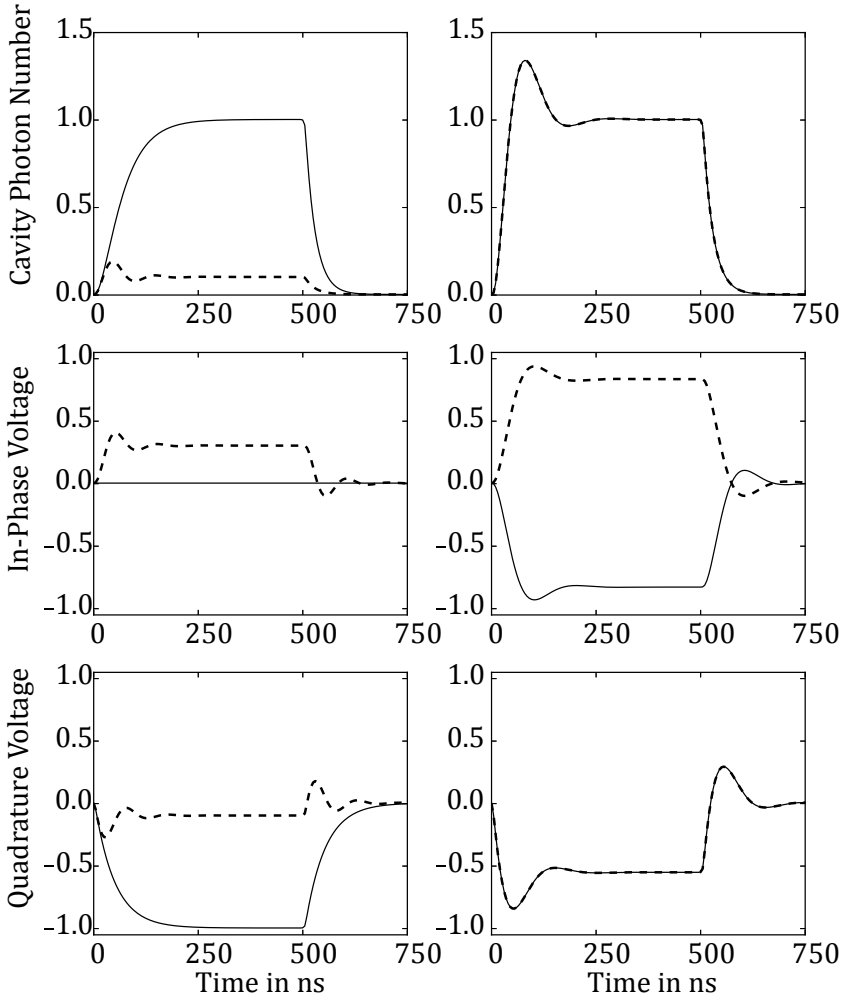

Figure 2.14: Numerical simulation of the Jaynes-Cummings model with driving at the dispersively shifted cavity frequency (left) and the bare cavity frequeny (right). The solid (dashed) lines are the responses for the qubit in the ground (excited) state. The driving pulse starts at 0 ns and ends at 508ns with 4ns tanh rise and fall. System parameters are $\omega_q/2\pi = 8\,\mathrm{GHz}$, $\omega_r/2\pi = 10\,\mathrm{GHz}$, $g/2\pi = 100\,\mathrm{MHz}$ and $Q_e = 1500$. For the simulation, the Lindblad Master equation[Lin76] solver of the QuTiP package[JNN12] was used.

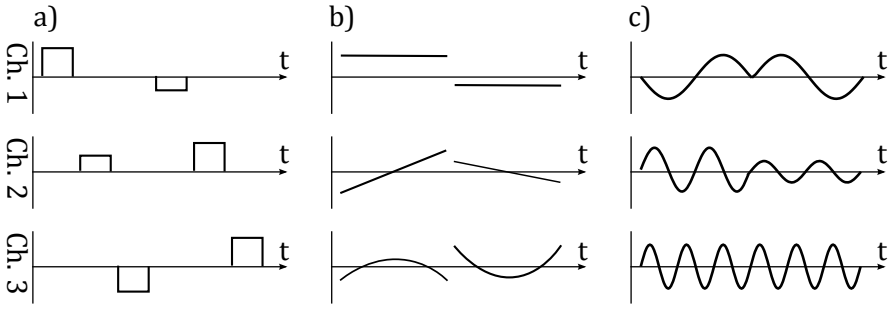

Figure 2.15: Comparison of a) Time-division (TDM), b) Code-division (CDM) and c) Frequency-division (FDM) multiplexing. The channel signals are added and transmitted over a common medium. TDM uses individual time slots for each channel. CDM uses basis functions that are orthogonal with respect to a convenient inner product. FDM uses different frequency sines, equivalent to frequency slots. TDM and FDM can be considered special cases of CDM.

combines several low-frequency inputs by shifting each of the inputs in the frequency domain by a different offset frequency and subsequent summing of the shifted inputs. The channel data is regained by frequency shifting in the reverse direction and filtering out of the frequencies that are associated with the other channels. For frequency-division to work, the bandwidth of the input signals has to be bounded, otherwise the channels are no longer separable. To multiplex all inputs, the bandwidth available in the output medium must be at least the sum of the bandwidths of all input signals. The requirement of bandwidth-limited inputs also restricts the time resolution, which is the main drawback of the system.

Code-division multiplexing combines several analog input channels by multiplication with channel-specific function or digital input channels by multiplication with a channel-specific sequence of bits (code) and subsequent addition. The input data is retrieved by calculating the inner product of the sum signal with each of the channel codes. The design of the code defines the performance of this system. If orthogonal channel codes are used, there is no cross-correlation between the codes and thus no crosstalk between the channels. In this case, the minimum bitrate on the output medium must be the sum of the bitrates of the input channels.

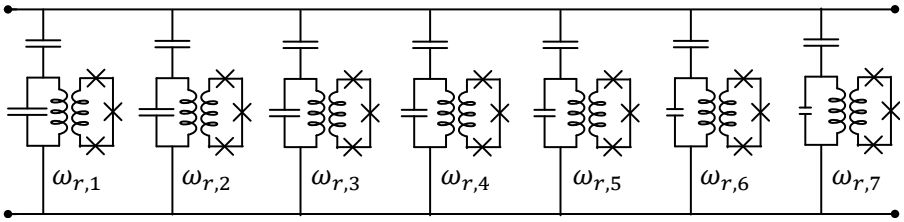

Figure 2.16: Circuit schematic of a frequency-division multiplexing readout system for qubits. Multiple microwave cavities with different center frequencies are shunting a common feedline. Each cavity is coupled to an individual qubit. Dispersive Jaynes-Cummings interaction shifts the cavity, frequency-modulating the state of the qubit onto the cavity.

Other codes can operate with a lower capacity output medium but will sometimes fail to reproduce the input data correctly.

2.5.2 Multiplexed Dispersive Readout System

For qubit readout, we chose to implement a frequency-division multiplexing technique based on circuit QED. A number of microwave resonators with slightly different freuencies are attached to a common feedline, as shown in Fig. 2.16. Each resonator is coupled to a single qubit, forming a Jaynes-Cummings system. The systems are operated in the dispersive regime and the frequency shifts of the resonators are used as qubit readouts. For a single resonator, this technique is explained in detail in section 2.4.4.

This kind of frequency-division multiplexing is very suitable for qubit readout, because being a frequency-domain method, it allows a simultaneous and continuous-time measurement of the states of all qubits multiplexed on the line. In addition, dispersive readout can be used with any type of superconducting qubit and is even the sole readout technique available for transmon qubits[KYG+07].

2.5.3 Crosstalk and Minimum Channel Bandwidth

In a multiplexed transmitter-receiver system, interference between different channels is called adjacent channel interference or simply crosstalk.

Like noise, crosstalk deteriorates the signal-to-noise ratio of a channel, in this context also called signal-to-interference ratio. In extreme cases, the deterioration may be large enough so that the channel data can no longer be decoded correctly, so any multiplexing system must be designed to keep crosstalk at manageable levels. In a frequency-division multiplexing system, crosstalk is caused by spectral components transmitted on a channel that are outside the allocated bandwidth and assigned instead to another channel.

In communications systems, interference is quantified by the ratio of interference power to signal power in a channel. If a multiplexed qubit readout system is measured in reflection, this definition can be used directly. The readout resonators, being passive devices, do not themselves generate a signal, but transmit a part of the externally generated probe power to the receiver due to reflection. Using the scattering matrix, the signal power introduced by readout resonator i probed at frequency ω is

$$P_{\text{signal,i}} = |S_{11}(\omega;\omega_i)|^2 \, P_{\text{probe}}.$$

Assuming that the probe power is the same for all channels, neglecting interference of the reflected waves and multiple reflections, the interference power in channel i is simply the sum of all individual contributions,

$$P_{\text{interference,i}} = \sum_{j\neq i} |S_{11}(\omega;\omega_j)|^2 \, P_{\text{probe}}.$$

The signal to interference ratio is the quotient of the signal and interference powers,

$$(S/I)_{\text{refl,i}} = \frac{|S_{11}(\omega;\omega_i)|^2}{\sum_{j\neq i} |S_{11}(\omega;\omega_j)|^2}.$$

If the channel is probed on resonance, which is typical if a phase-sensitive readout is performed, and the resonator is overcoupled, $S_{11}(\omega_i;\omega_i) \to 1$. The expression simplifies further to

$$(S/I)_{\text{refl,i}} \approx \left(\sum_{j\neq i} |S_{11}(\omega_i;\omega_j)|^2 \right)^{-1}. \tag{2.61}$$

If the multiplexed readout system is measured in transmission, each of the resonators removes energy from the signal seen at the receiver due to reflection or absorption. In this situation, the signal-to-interference ratio can be defined to mean the ratio of the power removed from the signal and the transmitted probe power. Again ignoring multiple reflections and interference of reflected waves, the power remaining after transmission along the off-channel resonators is

$$P_{\text{transmitted,i}} = \prod_{j \neq i} |S_{21}(\omega; \omega_j)|^2 \, P_{\text{probe}}.$$

The power removed from the feedline is $P_{\text{probe}} - P_{\text{transmitted}}$, which yields a signal-to-interference ratio of

$$(S/I)_{\text{trans,i}} = \frac{\prod_{j \neq i} |S_{21}(\omega; \omega_j)|^2}{1 - \prod_{j \neq i} |S_{21}(\omega; \omega_j)|^2}. \tag{2.62}$$

In both cases, calculation of the signal to interference ratio amounts to finding the scattering matrices of the readout resonators. Because of the qubit dynamics, the effective bandwidth of each readout channel may be somewhat larger than what is expected from considering only the resonator in a static situation. In the following, the key factors determining the bandwidth requirement for each channel will be reviewed.

Resonator Quality Factor

Using Eq. 2.46 and the identity $Q_0 = (1 + \kappa)Q_L$ from section 2.3.1, the coefficients Eq. .2.44 of transmission and reflection of the feedline through each coupled resonator can be rewritten as

$$S_{11} = -\frac{1 - S_{21_r}}{1 + 2iQ_L\delta} \qquad \text{and}$$
$$S_{21} = \frac{S_{21_r} + 2iQ_L\delta}{1 + 2iQ_L\delta}.$$

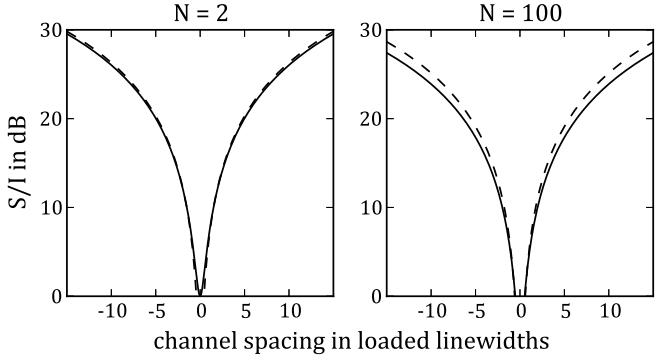

Figure 2.17: Signal-to-interference ratio of a N-channel readout system vs. frequency spacing between the resonators. The solid/dashed line represents a reflection/transmission measurement. A coupling ratio of $\kappa = 10$ was used. In an n-channel system, the S/I ratio scales approximately as $(\sum_{i=1}^{n} 1/i^2)^{-1}$.

For a two-channel device, the interference introduced into the first channel by the second channel, from Eqns. 2.61 and 2.62, is

$$(S/I)_{\text{refl, 2ch}} = |S_{11}(\delta)|^{-2} \approx 1 + 4Q_L^2\delta^2 \qquad \text{or}$$
$$(S/I)_{\text{trans, 2ch}} = \frac{|S_{21}(\delta)|^2}{1 - |S_{21}(\delta)|^2} \approx 4Q_L^2\delta^2.$$

In both expressions, $\delta = \delta\omega/\omega_1$ is the channel spacing normalized to the center frequency of the interfering channel. The summand 1 present only in the reflection case results from the fact that the power reflected from two resonators at identical frequencies is equal, yielding a S/I ratio of 1 (0 dB). In the transmission case, the second resonator removes the signal power completely, resulting in $S/I = 0$ ($-\infty$ dB).

For an n-channel device with equal frequency difference between the resonators, the argument δ becomes $\delta_j = j\delta$. In the limit of $Q_L\delta \gg 1$, the sum of Eq. 2.61 is readily evaluated, yielding

$$(S/I)_{\text{refl, }n\text{ch}} \approx \left(\sum_{j=1}^{n-1} \frac{1}{j^2}\right)^{-1} (S/I)_{\text{refl, 2ch}}.$$

For large n, the sum converges to $\pi^2/6 \approx 1.64$. The product of Eq. 2.62 is more involved. Numerical simulations show a scaling equal to the reflection case. Numerically simulated S/I ratios for $N = 2$ and $N = 100$ are plotted in Fig. 2.17.

Dispersive Shift

The dispersive shift effectively creates two realizations of each resonator, at (angular) frequencies of $\omega_r \pm g^2/\omega_{rq}$ (Eq. 2.58). The channel spacing demanded by the resonator quality factor can simply be increased by g^2/ω_{rq} to accomodate for the shift. In the case of dispersive shifts large compared to the loaded resonator linewidth, a channel may be assigned to each of the realizations, increasing the number of channels to $2N$ for an N qubit system.

Measurement Pulse Duration

The maximum time available to measure the state of a qubit is determined by its energy decay time constant T_1. The uncertainty principle of the Fourier transform[Pin02] and analogous theorems for other time-frequency transforms impose a lower limit on the bandwidth of a limited-time signal. In case of the Fourier transform, the minimum time-bandwith product is obtained by a Gaussian-shaped pulse,

$$V(t) \propto \exp\left(-\frac{t^2}{2\sigma^2}\right)$$
$$\tilde{V}(\omega) \propto \exp\left(-\frac{\sigma^2\omega^2}{2}\right).$$

If the width of the time-domain signal is taken to be equal to be the standard deviation $\sqrt{\langle t^2 \rangle} = \sigma$ of the distribution, the bandwidth in rad·s^{-1} is $1/\sigma$ and the bandwidth in Hz is $1/(2\pi\sigma)$. At a measurement time of only 100 ns, this results in a bandwidth requirement of 1.6 MHz, which does not in practice limit the number of resonators that can be multiplexed.

Frequency Modulation Sidebands

A resonator used for dispersive readout loaded with many photons may be described like a classical harmonic oscillator with a modulated eigenfrequency. The voltage over the capacitor of the resonator must solve

$$\frac{\mathrm{d}^2}{\mathrm{d}t^2}U(t) + 2\gamma\omega_r \frac{\mathrm{d}}{\mathrm{d}t}U(t) + \left[\omega_r + \omega_\Delta \langle\sigma_z\rangle(t)\right]^2 U(t) = 0,$$

where ω_r is the bare resonance frequency, γ is the coefficient of damping and $\omega_\Delta = g^2/\omega_{rq}$ is the magnitude of the dispersive shift. In the limit of an undamped oscillator and under the condition that $\frac{\mathrm{d}}{\mathrm{d}t}\langle\sigma_z\rangle \ll \omega_r(t)$, this differential equation is solved by a frequency-modulated voltage signal,

$$U(t) = U_0 \cos\left[\omega_r t + \omega_\Delta \int_0^t \langle\sigma_z\rangle(\tau) d\tau\right].$$

If we take $\langle\sigma_z\rangle(t)$ to be sinusoidal with frequency ω_m, the spectrum of the frequency-modulated signal shows components at $\omega_r \pm j\omega_m$[Car22],

$$\begin{aligned} U(t) =& J_0(m)\left[\cos(\omega_r t)\right] - \\ & J_1(m)\left[\sin(\omega_r + \ \omega_m)t - \sin(\omega_r - \ \omega_m)t\right] - \\ & J_2(m)\left[\cos(\omega_r + 2\omega_m)t - \cos(\omega_r - 2\omega_m)t\right] + \\ & \cdots, \end{aligned} \tag{2.63}$$

where J_j are Bessel functions of the first kind and $m = \omega_\Delta/\omega_m$ is called the modulation index. The modulation index and thus the bandwidth requirement per channel depends on the frequency of the time evolution of the qubit during readout. If the qubit transition is not driven during the readout, the modulation frequency ω_m is determined by the T_1-decay of the qubit. An exponential decay with time constant T_1 transforms into a Lorentzian with a single-sided half-amplitude bandwidth of $1/T_1$, which can be used as ω_m. The total bandwith requirement can then be found by finding the number of sidebands with an amplitude that is larger than a chosen interference goal.

A first approximation for the bandwidth required per readout channel is a rule of thumb commonly attributed to J. R. Carson[Car22], which

states that 98% of the spectral power contained in $U(t)$ is inside a band of width

$$\Delta\omega = 2(\omega_\Delta + \omega_m)$$

around the carrier frequency ω_r. Because the spectrum is symmetric with respect to ω_r, the interference introduced into a neighboring channel with distance $\Delta\omega$ is smaller than -20 dB.

3 Experimental Setup and Technique

3.1 Sample Design and Fabrication

3.1.1 Sample Design

All measurements presented in this thesis were performed on a single sample, labeled *10J-SPMJ5*.Designed to demonstrate multiplexed readout, it was kept as simple as possible. The $10 \times 5\text{mm}^2$ chip, shown in Fig. 3.1a, contains a single 50 Ω coplanar transmission line of width $W = 150$ µm and $G = 83$ µm along its long edge. Seven $\lambda/4$ transmission line resonators with $W = 20$ µm and $G = 11$ µm are located in the center of the chip with a horizontal spacing of 1 mm. The geometric length of the resonators varies from 3132 µm to 2892 µm in steps of 40 µm. Resonance frequencies range from 9.3 GHz for the longest up to 10.25 GHz for the shortest resonator in steps of approximately 150 MHz. The inductance and capacitance of the equivalent LC circuits (Eqns. 2.50 and 2.39) are $L \approx 1.05$ nH and $C \approx 235$ fF, respectively. At the open (lower) end, the resonators are capacitively coupled to the feedline using elbow couplers, shown in Fig. 3.1d. The couplers have a bend radius of 150 µm, coupling length of 350 µm and a remaining feedline ground plane width of 5 µm. This geometry was simulated to result in an external quality factor of about 1,500. At the upper end, the resonators are tapered to $W = 1$ µm and $G = 8$ µm, and shorted to ground, as seen in Fig. 3.1b and c.

A three-junction flux qubit is located in one of the gaps between the inner conductor and ground plane close to the shorted end of each resonator. The two identical junctions of each qubit have an area of $700 \times 200\ \text{nm}^2$, a design critical current of 280 nA and capacitance of 4.9fF. The qubits were laid out for a minimum transition frequencies Δ from 6.9 GHz to 7.9 GHz, corresponding to α factors between 0.629 and 0.646. The persistent current predicted for this configuration (Eq. 2.8) is 170 nA. The qubits

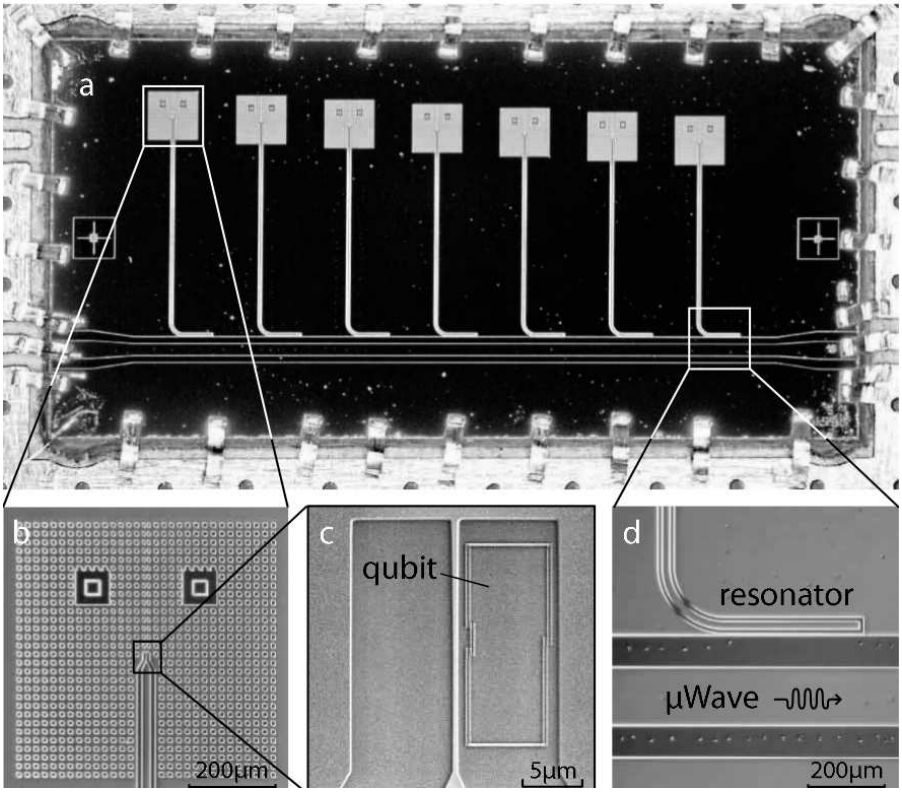

Figure 3.1: Micrograph of the sample used to demonstrate multiplexed readout. (a) The complete chip. Seven $\lambda/4$ resonators are capacitively coupled to a common feedline at the lower edge. The feedline carries combined resonator probe tones and qubit manipulation pulses. (b) Shorted (upper) end of one of the resonators. A grid of holes patterned onto the superconducting film pins Abrikosov vortices[Abr57] to stabilize magnetic bias fields and and reduce dissipation. The two dark squares are markers to align the Nb and Al structures. (c) One of the flux qubits. The qubit are located near the shorted end of the resonator to maximize the mutual inductance between the qubit and resonator. (d) An elbow-shaped capacitor coupling the resonator to the feedline.

are inductively coupled to the resonators, with the qubit loops of size $7 \times 16\,\mu m^2$ and resonator having a mutual inductance of 6 pH. Combined with the resonator zero-point current of $I_{res} = \sqrt{hf/L} \approx 80\,nA$, the estimated bare coupling energy (Eq. 2.53) is about 125 MHz. The qubits are galvanically decoupled from the resonator, making the fabrication of the qubits independent from the fabrication of the feedline and resonators.

The chip does not contain additional microwave inputs to manipulate nor coils to magnetically bias individual qubits. While this minimalistic approach results in a cleaner microwave response, it necessitates the use of external bias coils in the sample holder to control the operating points of the qubits.

Refer to Fig. 2.16 on page 50 for an electrical schematic of the sample.

3.1.2 Fabrication Technique

All samples were fabricated in the cleanroom facilities at IPHT Jena in a two-step process. In the first step, a 200 nm Niobium thin film was deposited on an undoped silicon substrate and patterned using electron beam lithography and CF_4 reactive ion etching. All coarse structures, such as the resonators and the feedline shown in Fig. 3.1(a), were fabricated in this step. The fine structures, the qubit loops and Josephson junctions, were deposted using the two-angle shadow evaporation technique[Nie74]; [Dol77].

In shadow evaporation, a stack of two different layers of photoresist is used to suspend a mask a few 100 nm over the substrate. Subsequently, two layers of metal are evaporated onto the sample at opposite angles to the normal of the substrate. If two holes in the mask are close enough, the projection of the first hole in the first evaporation will overlap with the projection of the second hole in the second evaporation. If oxygen is allowed into the chamber between the evaporations, an oxide layer forms between the metal layers, making the overlapping areas S/I/S tunnel contacts. An electron micrograph of such a contact on one of our chips is shown in Figure 3.2. The shadow evaporation method is very suitable to accurately produce very small Josephson junctions. However, the maximum junction size is limited by the stability of the bridges between the holes in the mask and can not exceed a few µm.

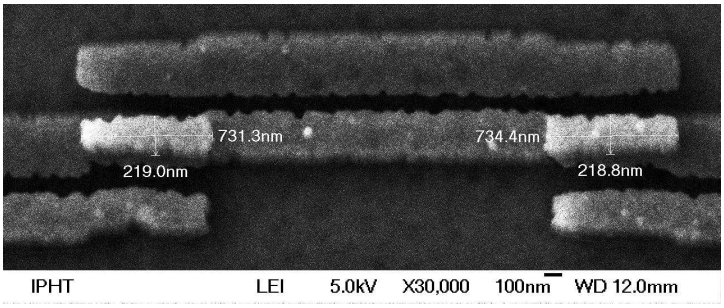

Figure 3.2: Electron micrograph of two $Al/AlO_x/Al$ Josephson junctions fabricated using the shadow evaporation technique. Aluminium was evaporated at angles of $\pm 30^\circ$ to the normal of the plane. The first evaporation was done from the lower edge of the image, the second from the upper edge. The two light squares are the Josephson junctions. The designed junction overlap was $700 \times 200\,\mathrm{nm}^2$.

3.2 Cryogenic Environment

3.2.1 Sample Holder

We use cylindric sample compartments milled from copper with an inner diameter of 28 mm and inner height of 5 mm, shown in Fig. 3.3. Its overall design is similar to the holders used by the quantum information groups at Yale university[Cho10] and ETH Zürich[Qsi]. The compartment features a fixed top part with through-holes for up to eight SMP-type microwave connectors and a groove into which a solenoid can be wound. Samples are installed on printed circuit boards (PCBs) fixed to a removable bottom 'lid' that is screwed to the fixed part of the holder.

The PCBs can be customized for each experiment, and can hold chips up to a maximum total area of approximately 15 mm by 15 mm. The boards used were produced by a commercial foundry[Hug] on RT/duroid 6010[Rog] substrate, which has a nominal dielectric constant of 10.2 at room temperature which is increases by about 20% at 4 K and is in very good agreement with the dielectric constant of the Si substrates, 11.6, used for the samples. This material choice results in matched transitions between the board and chip having similar dimensions on both sides, different only due to the different thicknesses of the conducting layer of

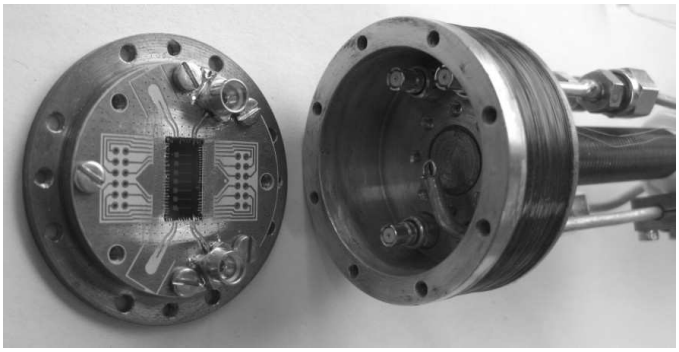

Figure 3.3: Photograph of the cryogenic sample compartment. The external coil wound around the box is used to supply a homogeneous flux bias to the qubits. A ring of holes close to the center holds the gradient coils (see section 3.2.2) which are not installed here. The SMP-type microwave connectors are threepartite to provide a low missmatch even when the PCB is not perfectly aligned. The small loop terminating the microwave cable in the center of the picture, used to supply nanosecond flux pulses to the qubits, was only present in one of the runs.

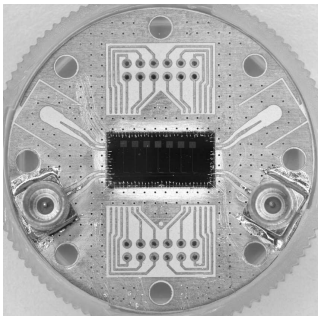

Figure 3.4: Photograph of a PCB with a sample mounted. The PCB has an outer diameter of $29\,\mathrm{mm}$ and a chip mounting area of $10.2 \times 5.2\,\mathrm{mm}$. Four coplanar lines can be used to transmit microwaves to and from the chip, but only two of them are required for this experiment. The coplanar lines are terminated with SMP-type connectors, which mate with connectors at the top of the sample compartment. The regular grid of holes are feedthroughs shorting together the ground planes at the front and back side of the PCB and also the otherwise disconnected ground planes at the top of the PCB. A large number of Al wire bonds from the chip to the PCB insure a low-impedance connection of the chip and PCB ground planes. Additionally, up to 24 DC connections are available, which can be contacted by pin headers soldered the back of the PCB.

35 μm on the PCB and 0.2 μm on the chip. In the coplanar structures used, a change of thickness influences mostly the capacitance between the inner conductor and ground planes, resulting in an a few ohms lower impedance of the same geometry on the PCB compared to the chip, which was corrected by modified trace widths. Microwave signals are coupled to the PCB through surface-mount 90° SMB connectors mating with their counterparts in the top part of the sample holder and additional DC signals are connected by means of header connectors soldered to the back side of the PCBs and routed through holes in the lid. A photograph of the PCB used in this experiment is presented in Fig. 3.4.

To protect the samples from external magnetic fields, a combination of a highly permeable outer shield and a superconducting inner shield was used. The outer shield made from Cryoperm attenuates outside fields, and the inner lead shield freezes the remaining field upon transition through its critical temperature. This ensures that fluctuating external fields does not cause fluctuations of the flux bias of the qubits.

3.2.2 Flux Biasing

In all single qubit experiments, the qubits were biased by a 1,500 turn superconducting NbTi solenoid wound around the exterior of the sample compartment. Each qubit sits in a closed loop formed by the central conductor of its readout resonator and the ground plane. Once the sample is superconducting, flux quantization precludes a net flux from entering the loop. The qubits can still be biased however, if the magnetic field inside the loop is inhomogeneous and the fluxes penetrating different parts of the loop sum up to zero. It is thus no surprise that the observed mutual inductances between the solenoid and qubits do not agree with the magnetic field distribution associated with a free solenoid. The experimentally measured mutual inductances, summarized in Table 4.2 on page 81, increase with increasing distance of each qubit from the edge of the chip, suggesting that they are biased predominantly by screening currents on the ground plane. In addition, each qubit sees a random offset flux that changes each time the temperature of the sample goes through the critical temperature of the Nb film and is likely caused by Abrikosov vortices trapped in the film.

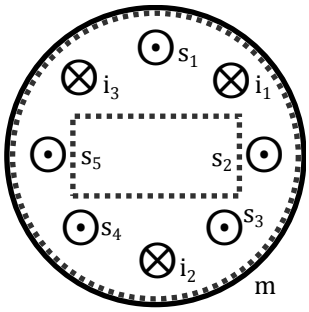

Figure 3.5: Arrangement of the bias coils. The main (m) coil is wrapped around the exterior of the sample box. Intermediate (i) size and small (s) coils are screwed to the fixed part of the sample box between the microwave feedthroughs.

To simultaneously operate multiple qubits at their sweet spot, additional bias coils are required. Three intermediate-size and five small gradient coils were screwed to the inside of the sample compartment to simultaneously bias several qubits at their symmetry points. Their arrangement is sketched in Fig. 3.5. Changing the bias of a single qubit while leaving the others at fixed bias values is complicated by the fact that each coil couples to all qubits. A function to automatically measure the mutual inductance matrix between the coils and qubits was implemented in the measurement software. Using the inverted mutual inductance matrix, the bias of up to four qubits could be individually controlled.

An additional high-frequency bias coil, made from a piece of coaxial cable by cutting back the outer conductor, bending the inner conductor and soldering it to the outer conductor, was used in some of the runs.It was placed in the center of the sample compartment, as shown in Fig. 3.3.

3.2.3 Wiring and Filtering

The experimental wiring inside the dilution refrigerator consists of only three coaxial cables carrying high-frequency signals to and from the sample and up to nine twisted pairs providing static flux biases to the qubits, shown in Figure 3.6.

To reduce the amount of high-frequency noise sent to the sample, the microwave input line feeding the readout resonators and qubits is

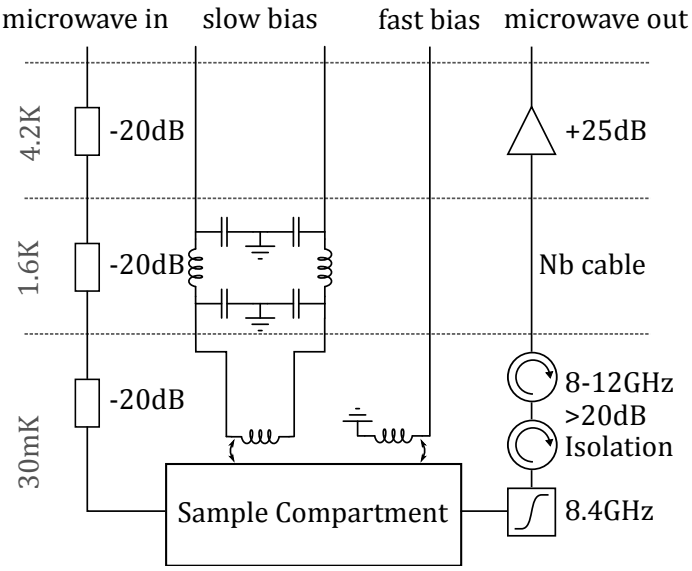

Figure 3.6: Experimental wiring inside the dilution refrigerator.

heavily attenuated. Without attenuation, the noise power fed from a 50 Ω-terminated device at room temperature into the 50 Ω feedline of the sample is equal to $P = k_B T \Delta f$, where Δf is the bandwidth of the line[Joh28]; [Nyq28]. An attenuator placed at one of the lower temperature stages feeds roughly the noise power of such a termination at the lower temperature in addition to the attenuated noise coming from its input. Therefore, at least one attenuator must be installed at the lowest temperature stage and its attenuation should be at least equal to the ratio of the temperature of the input termination and the temperature of the attenuator. We added attenuators of 20 dB at each at the 4.2 K, 1.6 K and 30 mK stages, maintaining this ratio and at the same time dissipating most of the power at the 4.2 K stage where the cooling power of the dilution refrigerator is greatest. Additional attenuation of about 10 dB, dependent on frequency and temperature, comes from the fact that the input line is manufactured from a stainless steel coaxial cable, which trades good high-frequency transmission for low thermal conductivity.

Other than in the input line, attenuation of the output line is not a viable option because the power sent into the output line can not be increased

arbitrarily to counter attenuation. Instead, noise coming through the output line in the reverse direction is removed by a series of two Pamtech XTE1238K cryogenic circulators with an isolation of 20 dB each in the band between 8 and 12 GHz, and lower frequency noise is rejected by a Mini-Circuits VHF-8400+ high-pass filter with a cutoff frequency of 8.4 GHz. The fast bias line does not include any filtering, because it is very loosely coupled to the sample, which translates into a large impedance missmatch between the line and the sample.

Signals coming from the sample are transmitted through a low-loss superconducting coaxial cable to a cryogenic HEMT amplifier at the 4.2 K stage with $G_1 = 26\,\mathrm{dB}$ gain and an equivalent noise temperature of $T_1 = 10\,\mathrm{K}$. The cryogenic amplifier is followed by two Mini-Circuits ZVA-183-S+[Min] room temperature amplifiers with $G_{2,3} = 26\,\mathrm{dB}$ gain each and equivalent noise temperatures of $T_{2,3} = 600\,\mathrm{K}$. The noise temperature of the complete amplification chain, calculated by Friis' formula[Fri44], is

$$T_{\mathrm{noise}} = T_1 + T_2/G_1 + T_3/(G_1 G_2) = 10\,K + 1.5\,K + 0.01\,K \approx 11.5\,K, \quad (3.1)$$

dominated by the cryogenic amplifier. The amplification chain adds a total thermal noise power of

$$P_{\mathrm{noise}} = k_B T \kappa / 2\pi \approx 1.6 \times 10^{-15}\,\mathrm{W}$$

within the 10 MHz bandwidth of a typical readout cavity. A 10 GHz cavity populated with a single photon on average loses

$$P_{\mathrm{loss}} = \hbar \omega_r \kappa / 2 \approx 0.2 \times 10^{-15}\,\mathrm{W} \quad (3.2)$$

to each half of the feedline. Thus, in the single photon regime, the amplification chain adds 8 noise photons to each signal photon.

Noise in the slow bias lines is reduced by LC lowpass filters in a π configuration, with a cutoff frequency of 250 kHz at 4.2 K.

3.3 Steady-State Readout

The experiments presented in section 4.1 involve the the measurement of the amplitude and phase of a microwave signal transmitted through the

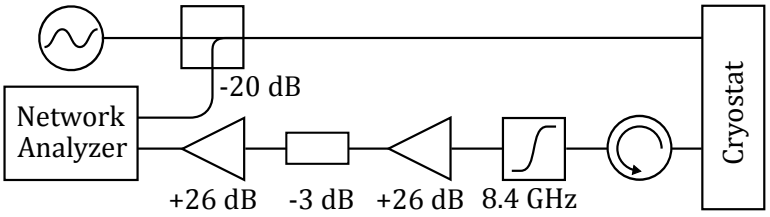

Figure 3.7: Room-temperature microwave setup used for measurements of steady-state properties.

sample with respect to various parameters such as the applied magnetic flux, probe and excitation frequencies and powers. In contrast to the experiments in the following chapters, they do not require time resolution and can thus be performed with little extra hardware. In addition to the general-purpose part of the experimental setup already discussed, we use a commercial Anritsu VectorStar MS4642A[Anr] network analyzer, designed to measure transmission and reflection of continuous wave signals between 70 kHz to 20 GHz through and from a device. Except for probe frequency sweeps, the sweep parameter is controlled by the measurement computer and single data points are retrieved from the network analyzer via a digital interface. Noise in the measured signal can be reduced by choosing appropriate parameters of digital band-pass filters and averaging functions implemented inside the device. Where an additional microwave tone is necessary to manipulate the qubits, it is combined with the signal of the network analyzer using a Narda 4226-20 directional coupler, where the probe tone is sent through the -20 dB coupled port, the manipulation tone is sent through the output port and the refrigerator input is connected to the input port. The complete room-temperature microwave setup is shown in Figure 3.7. This configuration is optimized to yield highest excitation power at the cost of probe power, which is suggested by the fact that at its resonance frequency, which is equal to the probe frequency, even a low excitation power loads the resonator with many photons, but at the qubit transition frequency, which is far from resonance, its small coupling capacitance to the feedline and large impedance isolate the qubit.

3.4 Time-Resolved Readout and Manipulation

The observation of the state evolution of a qubit system is limited by energy relaxation and dephasing. In superconducting circuits, the timescales of relaxation and dephasing are typically microseconds, but can also be tens of nanoseconds. The electronics used to manipulate and read out the qubit state must operate faster than that to resolve qubit dynamics.

Because both qubit manipulation and dispersive readout are based on microwave pulses, the two subsystems are composed of very similar equipment. In the manipulation system, fast digital-to-analog converters (DACs) with sub-nanosecond resolution output pulse envelopes, which are modulated onto continuous-wave microwaves using mixers. In the readout system, DACs provide short multitone bursts up to a few hundred megahertz which are shifted into the resonator band by the same mixers.

3.4.1 Microwave Mixers

A basic frequency mixer is an analog multiplier with two signal inputs and one product output. We use passive, double-balanced diode mixers, which are also known as ring modulators, because their main components are four fast-switching diodes that are arranged in a ring, as shown in Fig. 3.8. Two ports, the ‘‘local oscillator’’ (LO) and the ‘‘radio frequency’’ (RF), are transformer-coupled to the ring, such that two pairs diodes are between the two terminals of each port and only one diode separates one port from the other. The third port, the ‘‘intermediate frequency’’ (IF) port, is connected to a tap in the middle of each transformer. Any port can be an input or output, but because of this construction the LO and RF ports have a high-pass characteristic while the IF port has a low-pass characteristic.

If a frequency mixer is used for pulse modulation, the unmodulated input tone is connected to the LO (or RF) port and the pulse envelope is connected to the IF port. Once the voltage at the IF port exceeds two times the threshold voltage of the diodes, one pair of diodes switches to the conducting state, connecting the LO and RF ports. If the sign of the IF voltage is inverted, the other pair of diodes switches, rotating the phase of the signal passing between LO and RF by 180 degrees. The better

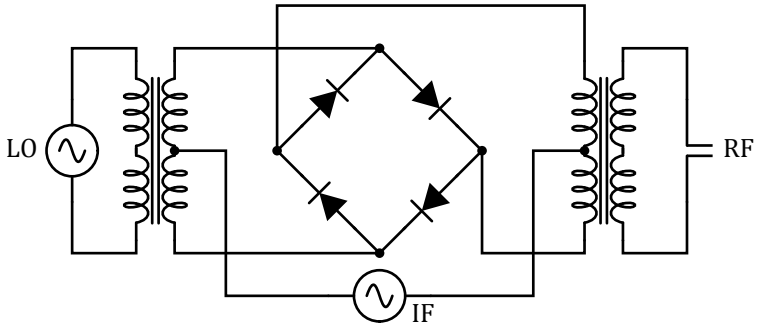

Figure 3.8: Circuit schematic of a double-balanced diode mixer. The inputs at LO and IF are multiplied to produce RF. Mixers can be used for amplitude modulation or frequency conversion. See main text for a detailed description.

the symmetry of the transformers and diodes, the lower the amplitude of unmixed input signals seen at the output port. The Marki Microwave M8-0420[Mar] mixers used for pulse modulation have a typical isolation of 40 dB between the LO and RF ports, equal to a maximum on–off output voltage ratio of 10^2, and a switching time of 250 ps. While other types of switches, such as pin diode switches, reach higher isolations of 60 dB and more, they require switching times of the order of 100 ns, which is too slow for qubit manipulation pulses.

If used for frequency conversion, a microwave tone strong enough to switch the diodes is applied to the LO port. As the phase of the drive evolves over time, the LO signal periodically switches one or the other pair of diodes into the conducting state, inverting the voltage of the signal passed between IF and RF. The output is thus a product of a square wave with fundamental frequency of f_{LO} and the second input applied to either the IF or RF port. Because square waves only show odd harmonics, the spurious frequencies introduced by multiplication start around $3f_{\mathrm{LO}}$ and can easily be filtered. If the mixer is used as an up-converter, the second input is connected to the IF port, producing an output of $f_{\mathrm{LO}} \pm f_{\mathrm{IF}}$ at the RF port. If the mixer is used as a down-converter, the second input is connected to the RF port, producing and output of $|f_{\mathrm{LO}} - f_{\mathrm{RF}}|$ at the IF port. An arbitrary number of frequency components can be applied to the RF and IF ports, but not to the LO port.

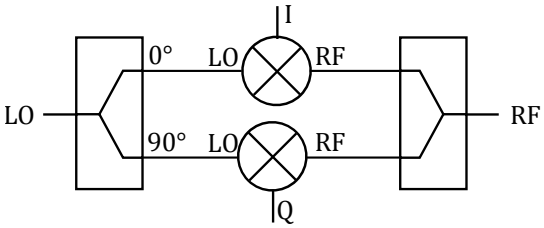

Figure 3.9: Block schematic of a two-quadrature mixer.

A two-quadrature or "IQ"-mixer is a four-port device that is a combination of two mixers and a phase shifter, see Fig. 3.9. The input supplied to the LO port is split and fed to the two mixers with a phase difference of 90 degrees. The first mixer multiplies the signal applied to the "in-phase" (I) port with the unshifted LO signal and the second mixer multiplies the signal at the "quadature" (Q) port with the phase-shifted LO. The sum of the two mixer RF outputs is passed to the RF output of the composite device.

The sum $I\sin(2\pi f_{\mathrm{LO}}t) + Q\cos(2\pi f_{\mathrm{LO}}t)$ of outputs of the two internal mixers can be rewritten as $\sqrt{I^2+Q^2}\sin(2\pi f_{\mathrm{LO}}t + \varphi)$ where $\varphi = \arctan(Q/I)$ $(+\pi)$. An IQ mixer can be thus be used as a phase modulator by applying different amplitude DC inputs to I and Q. It can also be used as a single sideband mixer by applying phase shifted inputs of equal frequency f_{IF} to I and Q, such that either the mixing product $f_{\mathrm{LO}} + f_{\mathrm{IF}}$ or $f_{\mathrm{LO}} - f_{\mathrm{IF}}$ is cancelled from the sum. Like a regular mixer, an IQ mixer can be used in reverse to measure the phase difference of microwaves applied to LO and RF or to separate the upper and lower sidebands of an RF signal.

3.4.2 Qubit Readout

For the dispersive readout of a single qubit, a microwave generator and a two-quadrature mixer are sufficient. The microwave generator provides continuous wave signal at the bare frequency of the readout cavity that is split by a power divider. One part of the signal is provided to the local oscillator port of the mixer mixer as a reference and the other one is transmitted through the sample and input to the RF port of the

mixer. In this so-called homodyne configuration, the I and Q outputs are constant DC voltages, and their ratio encodes the phase difference of the transmitted and reference signals. As the transmitted phase depends on the dispersive shift of the readout cavity and the dispersive shift of the cavity depends on the state of the qubit, I and Q switch between two sets of constant voltages as the qubit switches between its ground and excited states. Because an excited state qubit will inevitably decay to its ground state due to energy relaxation, the I and Q outputs are voltage pulses with a duration of the order of T_1 that decay to the ground state voltages. The voltage pulses can either be recorded using an analog integrator and a low-speed data acquisition system or using a moderately fast ($O(1/T_1)$) analog to digital converter. A setup like this was used for qubit characterization until a high-speed ADC was available.

To read out N qubits, N microwave tones at the frequencies of the readout cavities must be transmitted through the sample and their individual amplitude changes and phase shifts detected. For small N, the homodyne setup for a single qubit could simply be multiplied by the number of qubits, but even for moderate N this quickly becomes impractical. Our readout setup, shown in Fig. 3.10, uses software-defined radio techniques to simultaneously generate an arbitrary number of readout tones.

A measurement computer generates two digital waveforms, the first representing a sum of N sine functions and the second representing a sum of N cosine functions, with equal amplitudes and frequencies of $f_i = f_{\mathrm{res},i} - f_{\mathrm{LO}}$, where f_{LO} is a freely chosen reference frequency. These so-called baseband waveforms are output by a Tektronix AWG7062B 10 bit 6 GS/s DAC[Tek] (2010 and 2011 experiments) or a UCSB GHzDAC 14 bit 1 GS/s DAC[Ghz] (2012 experiments) and fed into the I and Q inputs of a Marki Microwave IQ-0618[Mar] quadrature mixer. The special choice of I and Q waveforms operates the mixer as a single-sideband upconverter, producing mixing products at $f_{\mathrm{res},i} = f_{\mathrm{LO}} + f_i$ and suppressing the image frequencies at $f_{\mathrm{LO}} - f_i$. Any frequency within two times the analog bandwidth of the DACs around f_{LO} can be individually generated. The spurious free bandwidth is two times that achieved which a conventional mixer, which would produce two sidebands that are mirror images of each other.

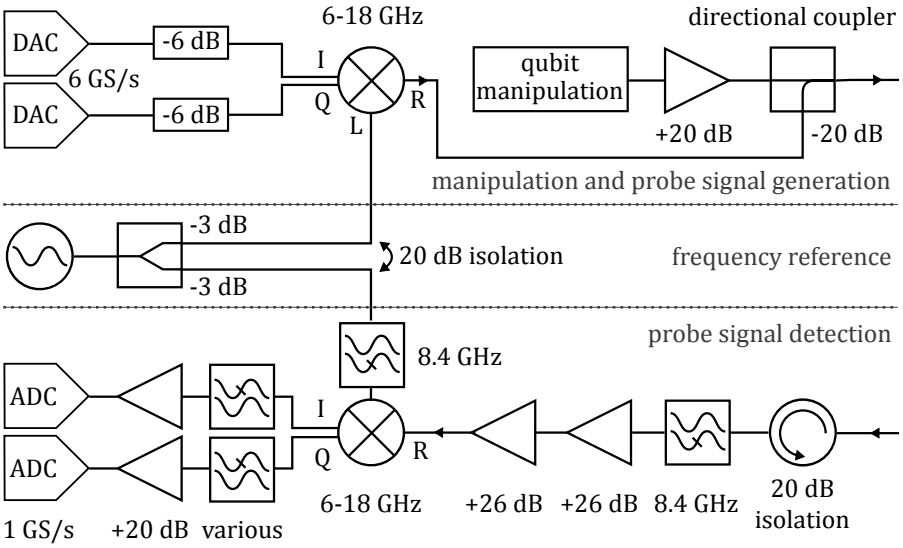

Figure 3.10: Room-temperature microwave setup for simultaneous readout of multiple qubits. A dual-channel digital to analog converter generates a baseband signal with one frequency component per qubit to be read out. This is up-converted to the band of the readout cavity by the first IQ mixer, creating the probe signal. Attenuators between the DAC and mixer dampen reflections from the mixer inputs. The qubit manipulation signal is generated separately and combined with the probe signal using a directional coupler. The directional coupler maximizes the amplitude of the manipulation signal while reducing the amplitude of the probe signal. This is reasonable because the manipulation signal is off-resonant with the readout cavities through which it must pass to reach the qubits. After the combined signal is transmitted through the cryogenic setup including the sample, it returns to the detection section. The detection section starts with an isolator to suppress reflections between the cryogenic and room-temperature amplifiers. The following high-pass filter ensures that the room-temperature amplifiers are not saturated by thermal noise from the cryostat. A second IQ mixer converts the transmitted signal back to baseband frequencies. Low-pass filters in I and Q cut noise above and below the band of the readout cavities and double as anti-aliasing filters. After a final amplification stage, the baseband signal is recorded by a fast two-channel ADC.

After passing through the cryogenic part of the setup, the transmitted signal is high-pass filtered to remove a large part of the (amplified) thermal noise power originating from the cryostat and amplified by two room-temperature amplifiers. A second, identical IQ mixer converts the signal back to baseband frequencies. The local oscillator port of the down-converter is driven from the same source as the up-converter to provide a stable phase reference. The LO is split by a Wilkinson power divider with 20 dB of isolation between its output ports to prevent leakage of the high-frequency probe signal between the generation and detection stages. A high-pass filter installed between the two mixers does the same to the baseband probe signal. Low-pass filters at the I and Q outputs of the down-converter further reduce the total noise power by limiting the detector bandwidth to the minimum required to address all readout cavities. After a final amplification stage, I and Q are sampled by a Spectrum M3i.2132 8 bit 1 GS/s ADC board[Spe] installed in the measurement computer. Software on the measurement computer performs a fast Fourier transform on the sampled data to recover the amplitude changes and phase shifts of all components of the probe signal.

The cryogenic and room temperature amplification chain is the same used for the steady-state measurements and presented in section 3.2.3. At readout powers in the single photon regime, the amplifiers add approximately 8 noise photons per signal photon in the bandwidth of each resonator. The readout signal is sent as a 512 ns burst, limited by the energy relaxation time of the qubits. In this time, approximately 32 signal photons are transmitted from the readout cavity to the output, resulting in a best-case signal-to-noise ratio of $\sqrt{32}/8 = -1.5\,\mathrm{dB}$. It is thus not possible to extract the state of the qubit from a single time trace in this configuration, averaging is required.

With the help of ultra low-noise parametric amplifiers and at larger mean cavity occupation numbers, such a single-shot readout and even real-time monitoring of the time evolution of a qubit's state is possible and has already been demonstrated for a single qubit[VSS11]. Because parametric amplifiers are based on high-quality oscillators, they have narrow gain bandwidths and a separate amplifier is required for each readout cavity. If designed together with the readout cavities and inte-

grated on the same chip, using them may be possible and they may see use in future experiments.

A stable phase reference is a key requirement when averaging the transmitted AC voltage signal. In a homodyne setup, the only phase of interest is the phase of the microwave generator. A stable reference is guaranteed by driving the down-converter from the same source that also generates the probe signal, the mixer output is DC. In the multi-qubit setup, the baseband signal is a sum of several AC components, the phase of which must be taken into account. If the baseband is generated by a DAC, the starting phase of all components is defined by the waveform and the phase found at the detector is constant as long as the DAC and ADC are triggered with a constant delay. If the baseband is generated by free-running oscillators or if the DAC can not be reliably triggered, the baseband signal must be sampled before up-conversion and a reference phase must be calculated from this data.

3.4.3 Qubit Manipulation

For qubit manipulation, a number of different setups were used depending on the experiment and the number of qubits to be manipulated.

If available, a Tektronix AWG5014 14 bit 1.2 GS/s four channel DAC[Tek] was used to generate pulse envelopes. The envelopes were applied to continuous wave microwaves generated by individual microwave sources using various arrangements of standard and quadrature mixers, shown in Fig. 3.11. Simple pulse shapes could also be realized by a pulse generator instead of the DAC, but without the low-frequency noise rejecting averaging described in section 3.4.5.

The simplest setup, Fig. 3.11a, uses a single mixer to gate the output signal of a continuous wave generator. This setup is sufficient for single qubit manipulation with moderate pulse amplitudes. Because of the limited isolation between the ports of mixers, a small driving is always on even when no voltage is applied to the IF port. The Marki Microwave M8-0420[Mar] used are high-isolation mixers providing an excellent LO–RF isolation of 40 dB, or an on–off amplitude ratio of 10^2. Typical on-state Rabi frequencies realized in the experiments were in excess of 100 MHz, resulting in off state Rabi frequencies of the order of a MHz in this setup.

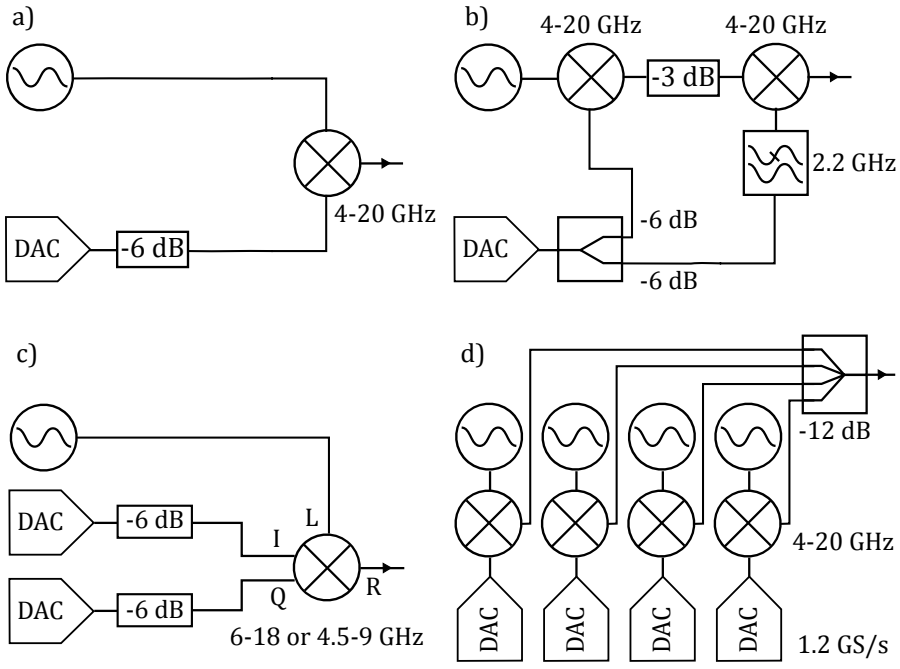

Figure 3.11: Experimental setups for qubit manipulation pulse generation. Each microwave generator provides a single continuous wave tone at the transition frequency of the qubit to be manipulated. The digital to analog converters output DC pulses that are used as amplitude envelopes. 6 dB attenuators between the DACs and mixers are used to dampen double pulses caused by reflections at the mixer inputs. a) The most leightweight setup uses a single microwave mixer as a switch to apply the envelope pulses to the generator output. Because of the limited LO-RF isolation of the mixer, an appreciable qubit drive is present in the off state of the mixer. b) Two mixers can be daisy-chained to lower the driving amplitude in the off state. A low-pass filter in the IF path avoids leakage of the generator tone caused by relatively low LO-IF and IF-RF isolations. c) Using a quadrature mixer and two DAC outputs, the amplitude and phase of the manipulation pulse can be controlled. This allows a free choice of the rotation axis of a Rabi drive in the x/y plane. d) Up to four microwave generators, DAC outputs and mixers are used for the multi-qubit experiments. Attenuators between the DACs and mixers have been omitted from the figure.

This introduces a significant probability of a state flip within the readout window of 512 ns.

The improved setup in Fig. 3.11b cascades two mixers to increase the on–off amplitude ratio to 10^4. The off state Rabi frequency is reduced to a few kHz, which causes negligible errors.

The setup in Fig. 3.11c uses a quadrature mixer to control both the amplitude and phase of the manipulation signal. With a standard mixer, the rotation axis of the qubit drive is fixed to the x axis. The phase control offered by an IQ mixer allows one to choose any rotation axis in the x/y on a per-pulse basis. Rotations around the z axis require a change of the level splitting of the qubit, which can be effected by pulsing the flux bias of the qubit from a third DAC channel.

For simultaneous manipulation of multiple qubits, an extra microwave generator and mixer was used for each qubit, as shown in Fig. 3.11. The outputs of all mixers were combined by an AtlanTecRF BPD-040180-4 four-port power divider[Atl]. In principle, multi-qubit manipulation could also be done using the same SDR techniques used for multiplexed readout. This requires a very fast DAC with an analog bandwidth that is large enough to access the transition frequencies of all qubits. Due to the large spread of our qubits' frequencies from 2 GHz to 6.5 GHz, this was not implemented.

3.4.4 Timing and Synchronization

The timing of the experiments was controlled by an Aglilent 81130A two-channel pulse generator[Agi]. The first channel was used to trigger the DACs creating the qubit excitation signal. The second channel was used to trigger the readout DACs and ADCs. The pulse generator was phase-locked to a 10 MHz reference signal which was common to the DACs and ADCs and the pulse generator.

The excitation and probe pulses were aligned by transmitting a large-amplitude excitation in the readout band, such that it could be acquired without averaging. This was possible because the sample is transparent to microwaves except at the resonance frequencies of the readout cavities. The probe pulse and ADC start were adjusted using a digital trigger delay feature provided by the ADC card.

Experiments were run at a rate of 10^5 averages per second, allowing the qubits approximately $10\,T_1$ to relax to their ground states between repetitions. The readout signal being a 512 ns burst, about 50 MB of data were generated per 8 bit 1 GS/s channel per second. Because Fourier transform and calculation of the mean are both linear operations, they commute and the more compute-intensive FFT was carried out on the averaged time-traces. Finally, the transmitted amplitude and phase were calculated from the complex Fourier coefficients.

3.4.5 Averaging with Low-frequency Noise Rejection

The dilution refrigerator used for all experiments being located in a 4th floor room without air-conditioning, the measured transmission was subject to drifts on timescales of minutes and hours due to temperature changes inside the laboratory affecting the cable delay.

Standard measurement protocols that use a per point averaging approach, where statistics for each data point are aquired before going to the next data point, are susceptible to these low-frequency drifts. Each point is affected by the drift accumulated from the start of the experiment until the measurement of the point.

An alternative is a per trace averaging approach. Here, the experimental parameters are changed on each repetition until a single measurement has been performed for each data point, completing a trace. More traces are recorded until sufficient statistics have been measured for all data points. This approach is more robust to drifts and low-frequency noise, because all points are equally affected.

Per trace averaging is used in all experiments where only pulse parameters need to be changed. Pulse waveforms for each parameter set are loaded into the manipulation DAC, which is set up to advance to the next waveform every time it is triggered, every 10 µs. The readout ADC is synchronized with the DAC, so that each acquisition can be sorted into the correct bin. A complete trace is finished after a few ms, rejecting noise at frequencies below a few hundred Hz.

The measurement software displays the average over all traces in a periodically updated plot. Partial averages over the traces acquired in the course of a few seconds are shown in a separate plot and also saved to

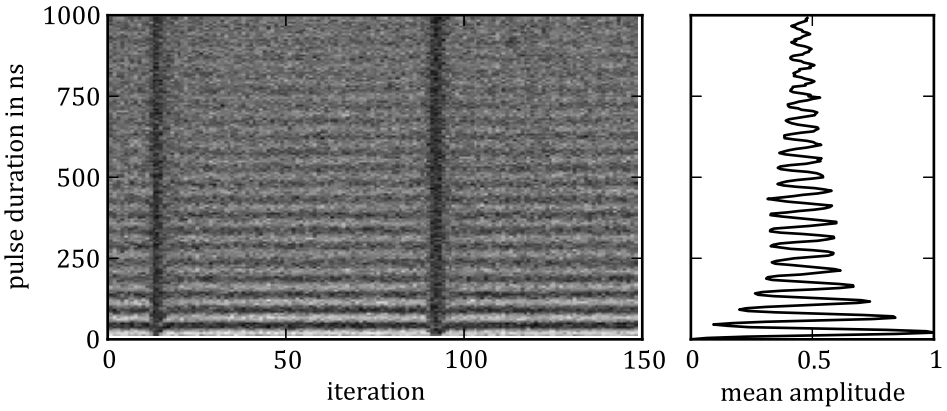

Figure 3.12: Detection of low-frequency drifts and dropouts. Each vertical line of the left plot is a mean over 1,000 traces acquired in the course of a few seconds. Phase drifts, if present, can be detected as a change in color in the x direction of the plot. Around average 15,000 and 90,000, two dropouts of the signal can be seen. The right plot shows the mean over all measurements.

disk. From the partial averages, drifts can be detected and dropouts can automatically be removed. Figure 3.12 shows a plot of partial averages next to the mean over all measurements.

4 Experimental Results

4.1 Steady-State Qubit and Resonator Measurements

4.1.1 Sample Characterization

Readout Resonators

The first measurement performed on any new sample once it has reached its operating temperature of a few Millikelvins is a frequency sweep of the network analyzer at zero external flux bias, shown in Figure 4.1. Due to the design of the resonators as an array of notch filters on a shared feedline, a minimum of transmission is seen at the resonance frequency of each resonator.

From the shape of each resonance peak, losses Q_0 internal to the resonator and the losses Q_{ext} due to the coupling to the feedline can be determined using equations 2.47 and 2.49 from section 2.3.5, as shown in Table 4.1.

device	resonance	Q_{ext}	Q_0 (*run 1*)	Q_0 (*run 3*)
1	9313 MHz	2,000	37,000	39,000
2	9458 MHz	1,500	79,000	19,000
3	9614 MHz	1,500	32,000	200,000
4	9773 MHz	1,500	23,000	61,000
5	9934 MHz	1,500	58,000	35,000
6	10094 MHz	1,000	17,000	72,000
7	10262 MHz	750	7,500	4,300

Table 4.1: Resonance frequencies and quality factors of the readout resonators measured at 30 mK.

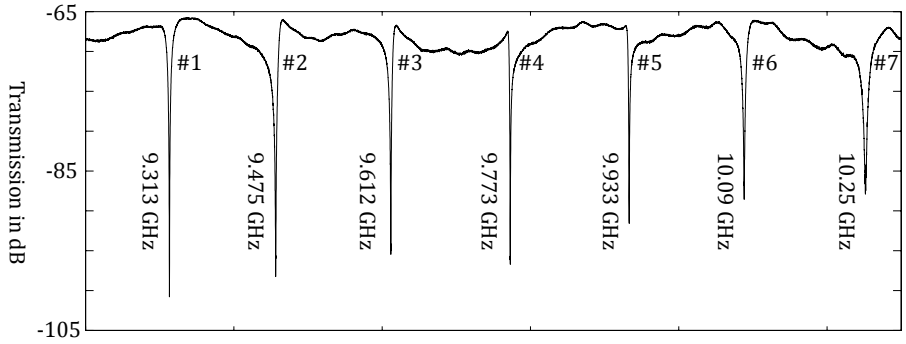

Figure 4.1: Transmission of sample 10J-SPMJ5 at zero flux bias.

The internal quality factors are different each time the sample is cooled down, which can be attributed to Abrikosov vortices trapped close to the resonator. Superconductivity is suppressed in the core of a vortex, and a movement of vortices induced by the radio frequency field of the oscillator leads to dissipation[SHD+09]. The magnitude of this dissipation depends on the vortex count and position. The internal quality factor of resonator #7 is worse than the others, because its resonance frequency is close to a box resonance of the sample holder, which supports a mode at 10.35 GHz into which the resonator can radiate energy.

Bias Calibration

The transition frequencies of flux qubits are far detuned from the cavity frequencies for all fluxes except a narrow range of a few mΦ_0 close to half frustration of the qubit loop. As the dispersive shift, Eq. 2.58, is proportional to $(\omega_r - \omega_q)^{-1}$, the inverse difference between the cavity and qubit frequencies, it becomes negligibly small at zero flux bias and the observed cavity resonance frequencies measured are the bare cavity frequencies. As discussed in section 2.4.4, at these frequencies the qubit state is encoded into the phase of the signal transmitted through the sample. Bias calibration for all qubits is done by measuring transmission at each bare resonance while sweeping the flux bias over a range of several Φ_0 using the external coil wound around the sample holder.

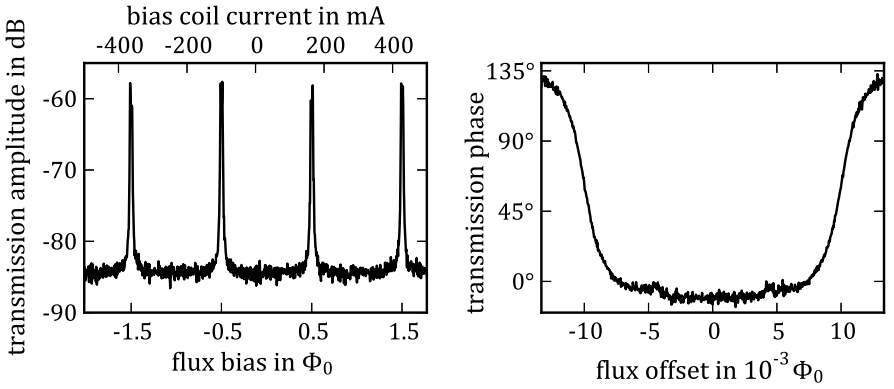

Figure 4.2: Transmission amplitude and phase through the feedline at the resonance frequency of resonator #5. (left) A coarse scan is used to determine the current needed to increase the flux through the qubit loop by Φ_0. (right) From a fine scan, the exact position of the symmetry point can be extracted. The two steep slopes are at the positions of anticrossings between the qubit and its readout resonator.

From a coarse magnetic field scan, shown in Fig. 4.2, the mutual inductance $M_{i,\mathrm{ext}}$ of the bias coil and qubits can be extracted. The transition frequency of the qubits is periodic in flux with a period of Φ_0, and so is the phase of the transmitted probe signal. By calculating the period of the phase response with respect to the current applied to the bias coil, we find that $M_{i,\mathrm{ext}}$ increases by 33% from qubit #1 to qubit #7. The absolute values of $M_{i,\mathrm{ext}}$ can be found in Table 4.2.

device	1	2	3	4	5	6	7	unit
period	398	334	305	281	264	254	252	μA
$M_{i,\mathrm{ext}}$	5.2	6.2	6.8	7.4	7.8	8.1	8.2	pH

Table 4.2: Mutual inductance of each qubit and the external bias coil.

In the absence of a superconducting film, the mutual inductance between the coil and qubits on the chip is expected to be maximum for qubit #4, which is located closest to the symmetry axis of the sample holder, shielding and bias coil, and decrease towards both the higher and lower qubit numbers. In the presence of the superconducting film, however, the

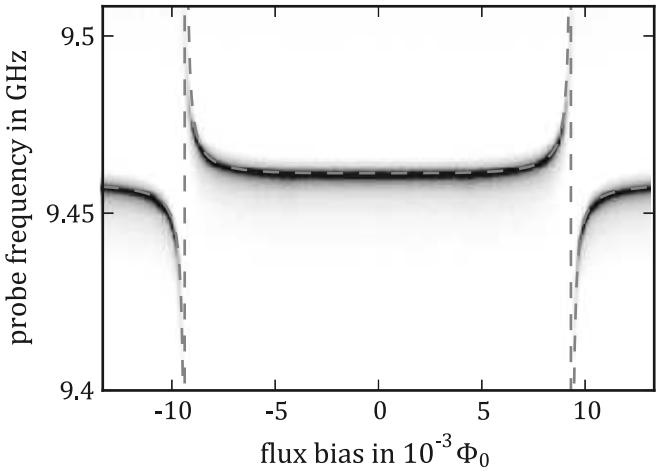

Figure 4.3: Transmission amplitude through the feedline in a range of frequencies close to the resonance frequency of resonator #5. At $\pm 9.4\,\mathrm{m}\Phi_0$, the sign of the dispersive shift changes because of the qubit transition frequency passing through the resonance frequency of the readout cavity.

flux bias is generated by screening currents on the film and depends on the distance of the qubit from the edge of the ground plane.

Zooming in on one of the peaks measured during the measurement of the mutual inductance reveals that they are double-peaks that are symmetric with respect to their central point. This point corresponds to a half-integer frustration of the flux qubit, with respect to which its energy levels are symmetric. The double-peak structure is only present when the minimum transition frequency Δ of the qubit is designed below the resonance of the readout cavity, and marks the points where the qubit transition frequency and cavity resonance cross each other.

Qubit-Resonator Anticrossings

In figure 4.3, the transmission amplitude of resonator #5 vs. the external flux bias and probe frequency is shown. From this plot it can be seen clearly that not only the transmitted phase but the position of the minimum of the absorption dip, which is equal to the resonant frequency of

this cavity, changes with the applied flux. With the qubit being in the ground state during the whole experiment, the microwave tone probes the transitions $|-,n\rangle \leftrightarrow |-,n+1\rangle$ between different resonator photon number states of the Jaynes-Cummings Hamiltonian. The dashed line represents the theoretical prediction Eq. 2.58 of the transition frequency $E_{-,n+1} - E_{-,n}$ in the dispersive limit, $\omega_{rq} \gg g$. It is in close agreement to the experimentally obtained data throughout the plot. In principle, the bias dependence of the resonator frequency provides an indirect measurement of the frequency of the qubit transition and the qubit-resonator coupling energy g. In practice this is complicated by the weak photon-number dependence of the shift and the fact that g decreases from the symmetry point to the anticrossing points according to Eq. 2.54 because of the changing mixing angle.

4.1.2 Two-Tone Qubit Spectroscopy

Low-Power Spectroscopy

The transition frequency of the qubit can be measured directly using two-tone spectroscopy. In addition to the probe tone at the cavity photon number transition, a second microwave (spectroscopy) tone is transmitted to the system. If this tone is close the $|-,n\rangle \leftrightarrow |+,n\rangle$ transition of the Jaynes-Cummings Hamiltonian, it acts as a Rabi drive and causes periodic oscillations between the qubit states. This causes a modulation of the instantaneous frequency of the readout resonator with the Rabi frequency Ω given by Eq. 2.19. The spectrum of the frequency-modulated resonator has sidebands at $\omega_r \pm j\Omega$ with amplitudes of $J_j(m)$, where $m = \omega_\Delta/\Omega$ and ω_Δ is the dispersive shift of the resonator. For $\Omega \lesssim \omega_\Delta$, many closely spaced sidebands are present – the spectrum is spread in the interval $[\omega_r - \omega_\Delta, \omega_r + \omega_\Delta]$. For $\Omega \gg \omega_\Delta$, only $J_0(m)$ is nonzero and the resonator appears at its bare frequency. In both cases, changes of the transmitted amplitude or phase at the dispersively shifted and bare resonance frequencies indicates a coincidence of the qubit transition and spectroscopy tone frequencies. Transitions to higher levels outside the qubit subspace can also be detected this way.

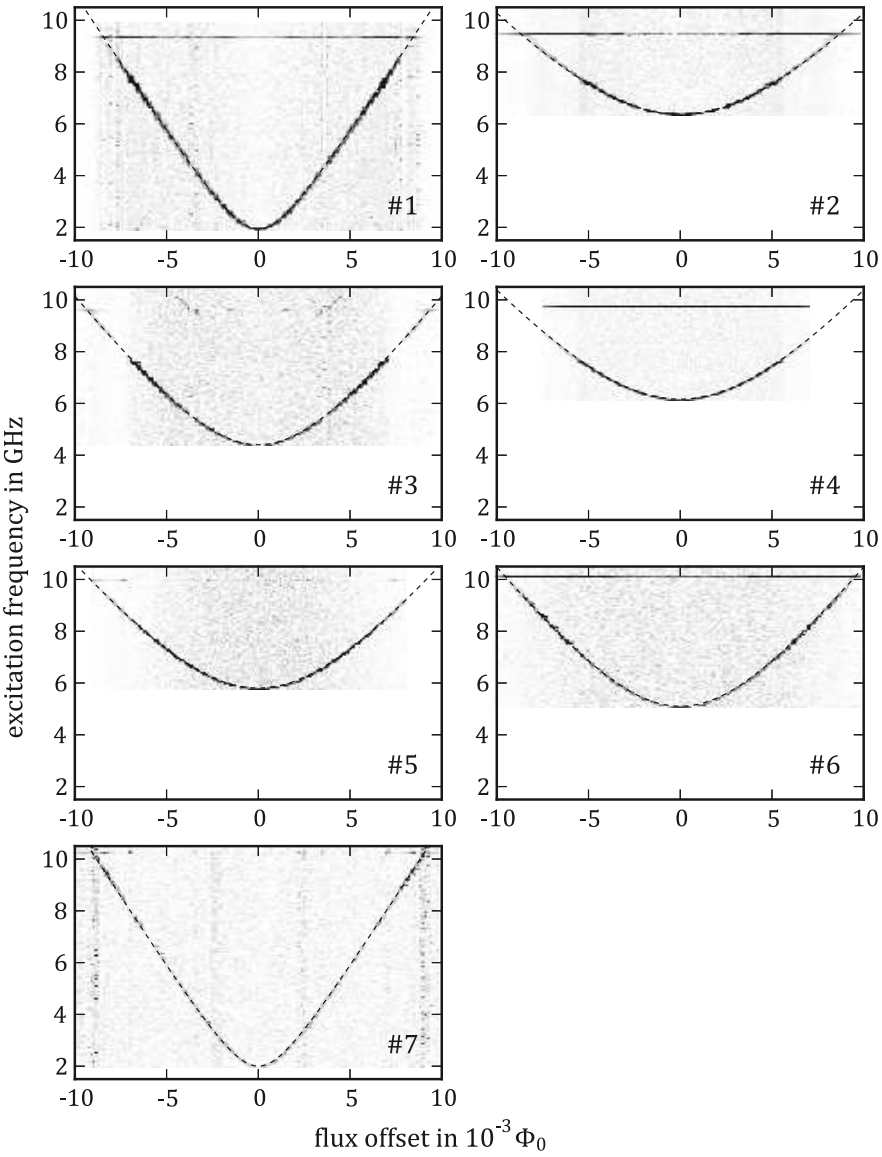

Figure 4.4: Spectra of the seven qubits. Dark color indicates a phase response of the cavity. The dashed black lines represent fits to the expected progression Eq. 2.13. The horizontal lines are caused by the spectroscopy tone exciting the resonator directly.

By sweeping the external flux bias and the spectroscopy tone frequency, the flux dependence of the qubit transition frequency can be mapped out. This curve provides the gap energy Δ and the asymmetry energy ϵ of the qubit, from which the persistent current I_p in the loop can be calculated. Δ depends sensitively on the geometry of the Josephson junctions of the qubit and gives feedback on the quality of the fabrication process. I_p is one of the factors determining the strength of coupling g of the qubit to the resonator. Alternatively, g can be calculated from the separately measured magnitude of the dispersive shift of the resonator and Δ. The parameters of the qubits found on the multiplexed sample are summarized in Table 4.3.

device	1	2	3	4	5	6	7	unit
Δ	1970	6350	4400	6170	5800	5100	2000	MHz
I_p	174	129	146	134	142	147	178	nA
g	51	73	80	85	89	89	51	MHz
T_2	63	114	224	150	286	218	79	ns

Table 4.3: Parameters of the seven qubit extracted from steady-state measurements.

The spectra of all seven qubits including fits of their transition frequencies are plotted in Figure 4.4. In the plot, a dark pixel indicates a phase response of the cavity at the corresponding combination of flux bias and spectroscopy tone frequency. The dark horizontal lines that appear in some plots are caused by the spectroscopy tone directly exciting the readout cavity or interfering with the probe signal detector. Towards the intersection points of the qubit and cavity frequencies, the contrast diminishes. This is caused by the dispersive shift increasing to several line widths, so that the transmission at the bare cavity frequency is no longer affected by the resonator in any of the qubit states. The dashed black lines are fits of the spectral line to the theoretical progression of the qubit transition with flux, given by Eq. 2.13.

In a Jaynes-Cummings system, the interaction between the qubit and cavity not only shifts the frequency of the cavity, but also the frequency of the qubit. This shift is known as the Autler-Townes effect or AC Stark shift and can be calculated using Eq. 2.57. Its magnitude is proportional to the

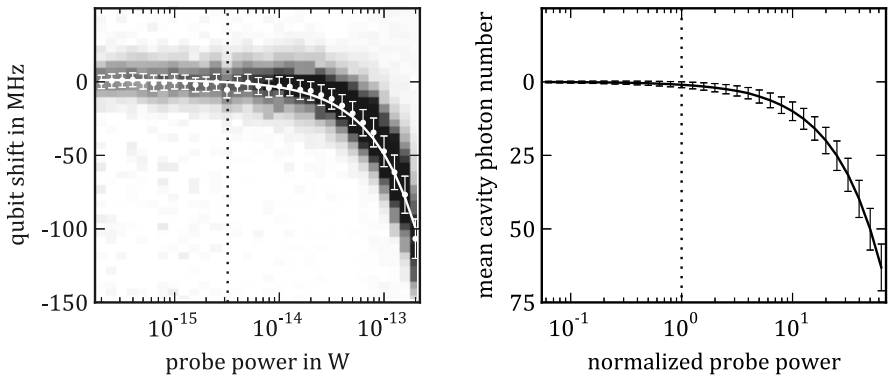

Figure 4.5: (left) AC Stark shift of qubit #6. The dashed vertical line at 3×10^{-15} W indicates the probe power at which the cavity is occupied by one photon on average. The shift is linear in the probe power, and appears exponential only because of the logarithmic power scale used in the plot. The error bars indicate the full width at half maximum of the spectral line. (right) Theoretical mean and standard deviation of the cavity occupation number vs. probe power, assuming the classical probe drives the cavity to a coherent state. The broadening at low probe powers in the experimental plot when compared to the theoretical data is a measure for the dephasing of the qubit.

number of photons n inside the cavity and thus to the probe power applied to the system. The color scale of Figure 4.5 shows the experimentally measured amplitude response of cavity #6 at the symmetry point of the qubit for different probe powers (x axis) and spectroscopy tone frequencies (y axis, offset by Δ). Up to probe powers of approximately 3×10^{-15} W (-115 dBm), the transition frequency is independent of the probe power, because the cavity is occupied by less than one photon on average. This power range is known as the single photon regime. At higher probe powers, a linear shift of the qubit frequency is visible, which appears exponential in this plot because of the logarithmic power scale used on the horizontal axis. Qubit spectra are measured in the single photon regime to avoid distortion.

The width of the qubit resonance line in the spectrum is linked to the dephasing rate of the qubit. This is because dephasing of a qubit is caused by fluctuactions of its transition frequency, which are quantified by the

line width in the spectrum. Deep in the single photon regime, the spectral line width γ is dominated by intrinsic dephasing of the qubit, and T_2 is $4\pi/\gamma$. At higher probe powers, the line is broadened by the variance $\sigma_n^2 = n$ (assuming the cavity is driven to a coherent state) of the mean cavity photon number n, shown as errorbars of the right plot. Because the T_2 broadening follows a Lorentz distribution and the broadening due to n follows a normal distribution, γ and σ_n can be separated in high-resolution data. In lower-resolution data, γ can be approximated by assuming all distributions are gaussian and using propagation of errors,

$$\sigma_{\text{total}}^2 = \frac{\gamma^2}{8 \ln 2} + \left(\frac{g^2}{\omega_q - \omega_r} \right)^2 \sigma_n^2.$$

The T_2 values provided in Table 4.3 were calculated from fits to this equation.

High-Power Spectroscopy

Low-power spectroscopy shows the first-order transitions of the Jaynes-Cummings Hamiltonian, the cavity photon number transition and the qubit transition, revealing qubit parameters and potential spurious couplings to defect states in the sample[SLH+04]. In addition to these, certain higher-order transitions are interesting for quantum information processing, since they may be used to create qubit-qubit[LWT+06]; [PGM+12] and qubit-photon[WSB+07] entanglement without the need to bring the entangled subsystems into resonance. For flux qubits, this has the advantage that they can be left biased at their sweet spots all the time, where they are least sensitive to flux noise. Other types of superconducting qubits, namely single junction transmon qubits, are fixed-frequency on purpose to remove the frequency control as a source of decoherence. Apart from making the cavity frequency tunable, which increases the decoherence of the cavity, exciting sideband transitions is the only way to entangle these qubits with cavity photons.

For quantum information processing, the ''blue'' sideband transition $|-, n-1\rangle \leftrightarrow |+, n+1\rangle$ at a frequency of $\omega_{\text{blue}} = \omega_r + \omega_q$ and the ''red'' sideband transition $|-, n\rangle \leftrightarrow |+, n\rangle$ at $\omega_{\text{red}} = |\omega_r - \omega_q|$ are the most interesting ones.

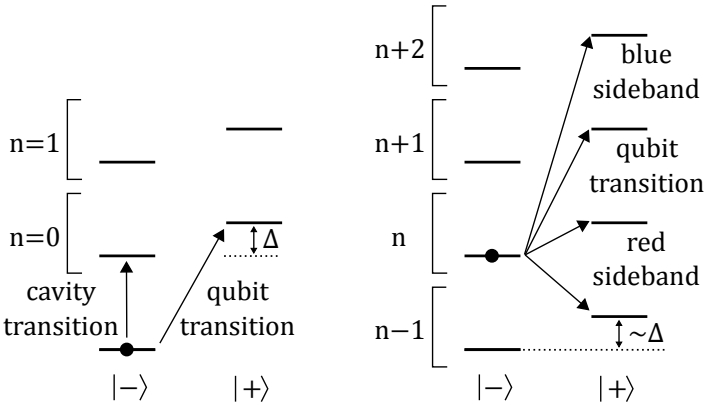

Figure 4.6: Transitions between the energy levels of the Jaynes-Cummings Hamiltonian seen in two-tone spectroscopy. (left) In low-power spectroscopy, the qubit-cavity system is initially in its ground state. The energy required to excite the system is at least $\hbar\omega_r$ or $\hbar\omega_q$, whichever is lower. k-photon transitions are suppressed by a factor of $(g/\omega_{rq})^k$, where $\omega_{rq} = \omega_q - \omega_r$. (right) High cavity probe powers result in a non-zero mean population of the cavity, allowing a cavity photon to combine with a low energy spectroscopy photon to induce a transition. At high spectroscopy tone powers the second order ''red'' and ''blue'' sideband transitions and multi-photon transitions become visible.

The spectrum of qubit #2 shown in Figure 4.7 was recorded at large spectroscopy and probe tone amplitudes, so that the cavity is always populated and the matrix elements of second order transitions become sufficiently large. The red sideband transition, shown as a dashed black line, can be clearly identified. The blue sideband transition starts at probe frequencies of approximately 17 GHz, which is outside the range of the plot. However, the two-photon blue sideband transition can be seen starting from 8.5 GHz and is shown as a dash-dotted black line. The strong driving also enables a number of other transitions, such as the two-photon qubit transition and the two-photon red sideband transition, which have matrix elements of comparable size. A list of identified transitions can be found in the figure caption.

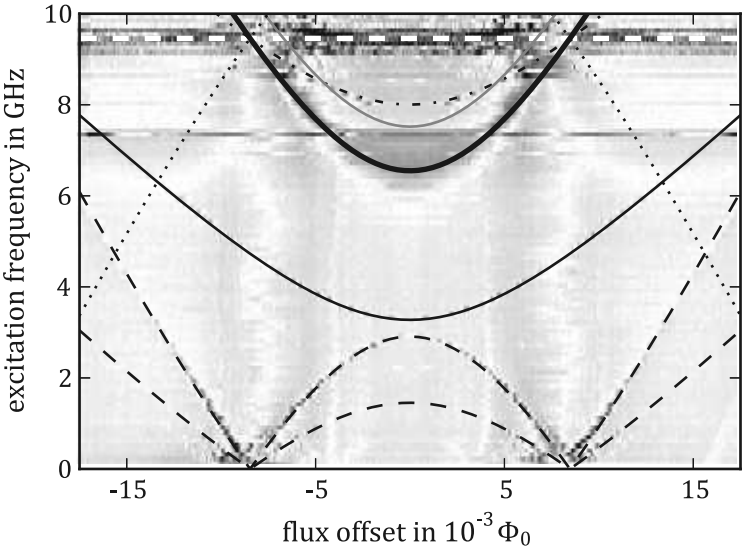

Figure 4.7: Spectrum of device #2 recorded with large spectroscopy and probe tone powers showing sideband transitions. The solid black lines are single and two-photon transitions between $|-,n\rangle$ and $|+,n+1\rangle$. The dashed black lines are single and two-photon red sideband transitions between $|-,n\rangle$ and $|+,n\rangle$. The dash-dotted black line is the two-photon blue sideband transition between $|-,n\rangle$ and $|+,n+2\rangle$. The dotted black line is the $|-,n\rangle \leftrightarrow |+,n-1\rangle$ transition. The origin of the solid gray line is unclear. The horizontal dashed white line indicates the frequency of the readout resonator.

4.2 Serial Measurements of Qubit Dynamics

4.2.1 Single Qubit Gates

Introduction

Among the list of elementary gates required to operate a quantum computer are arbitrary rotations of the state vectors of individual qubits. As shown in section 2.2.5, such rotations can be produced by driving qubits with microwave pulses. If the amplitude and phase of the drive and the detuning between the driving and qubit transition frequencies can be controlled on a per-pulse basis, the general rotation operator Eq. 2.17

can be directly implemented. If only the phase of the drive or only the detuning can be controlled, an arbitrary rotation can be synthesized from a sequence of three rotations[KG01] around two different axes (x-y-x, x-z-x, ...) by expressing the rotation vector in terms of Euler angles. The absence of flux lines allowing fast control of the qubit transition frequencies therefore does not restrict our ability to produce arbitrary single qubit gates.

Solution of the Lindblad Master Equation

Because physical qubits are subject to dissipation and dephasing, experimental results are better described using the time evolution Eq. 2.25 of the density operator instead of the coherent evolution of a pure qubit state represented by Eq. 2.17. Using the fact that the Pauli matrices together with the identity matrix σ_0 form an orthogonal basis of the vector space of 2×2 matrices, the equations for the components of the Bloch vector can be separated and Eq. 2.25 can be reformulated as an inhomogeneous first-order linear matrix differential equation in three dimensions,

$$\begin{aligned}\frac{\partial \vec{r}}{\partial t} &= \begin{pmatrix} -\gamma_2 & -\Omega_z & \Omega_y \\ \Omega_z & -\gamma_2 & -\Omega_x \\ -\Omega_y & \Omega_x & -\gamma_1 \end{pmatrix} \cdot \vec{r} + \begin{pmatrix} 0 \\ 0 \\ \gamma_1 \end{pmatrix} \\ &= M \cdot \vec{r} + \vec{c}.\end{aligned} \tag{4.1}$$

In this equation, $\vec{r}$ is the Bloch vector, Ω_i are the components of the rotation vector $\vec{\Omega}$ defined by Eq. 2.17, γ_1 is the longitudinal and γ_2 is the transversal relaxation rate.

The formal solution of differential equations in the form of Eq. 4.1 is

$$\vec{r}(t) = \vec{r}_* + \exp(Mt) \cdot (\vec{r}(0) - \vec{r}_*),$$

where $\exp(Mt)$ is the matrix exponential of Mt and $\vec{r}_* = M^{-1} \cdot \vec{c}$ is the steady-state solution.

If only resonant driving around the x axis, equivalent to $\Omega_y = \Omega_z = 0$, is considered, the equation for r_x can be separated from the equations for r_y and r_z. The equations for r_y and r_z can then be solved by expanding the 2×2 matrix in Pauli matrices and using the identity $\exp(i\vec{a} \cdot \vec{\sigma}) =$

$\sigma_0 \cos(a) + i\tilde{n} \cdot \vec{\sigma} \sin(a)$, where $a = |\vec{a}|$ and $\tilde{n} = \vec{a}/a$, to evaluate the matrix exponential. Because the readout apparatus can only measure the z component of the Bloch vector and experiments typically start with the qubit in the ground state, we are only interested in the solution of $r_z(t)$ with $r_z(0) = 1$ and $r_x(0) = r_y(0) = 0$,

$$r_z(t) = e^{-\overline{\gamma}t}\left[\cos(\tilde{\Omega}t) + \frac{\gamma_\Delta}{\tilde{\Omega}}\sin(\tilde{\Omega}t)\right](1 - r_{*,z}) + r_{*,z}. \tag{4.2}$$

Eq. 4.2 describes an oscillation decaying towards a relaxation and rotation rate dependent steady-state value

$$r_{*,z} = \frac{\gamma_1\gamma_2}{\gamma_1\gamma_2 + \Omega_x^2}. \tag{4.3}$$

The decay rate is the arithmetic mean of the longitudinal and transversal decay rates,

$$\overline{\gamma} = \frac{\gamma_1 + \gamma_2}{2}. \tag{4.4}$$

The frequency of these oscillations is the Rabi frequency Eq. 2.18, shifted to lower frequencies due to damping,

$$\tilde{\Omega} = \sqrt{\Omega_x^2 - \gamma_\Delta^2},$$

where

$$\gamma_\Delta = \frac{\gamma_2 - \gamma_1}{2}.$$

Due to the relaxation rates of r_x and r_y being equal, the above equations hold for any resonant driving if Ω_x is replaced by $\Omega = \sqrt{\Omega_x^2 + \Omega_y^2}$.

Readout Calibration

For each qubit, the readout apparatus outputs the transmission amplitude and/or phase shift R of the microwave tone scattered at the qubit's associated readout resonator. Due to the nature of the quantum mechanical measurement process, the output takes one out of two values, R_1 for the qubit in the ground state and R_{-1} for the qubit in the excited state.

In the absence of noise, one could perfectly discriminate between the two values and map them to the two qubit states. In a noisy system, the measured values are distributed stochastically with two normalized probability density functions (PDFs) $P_{\pm 1}$ that peak at the output values of the noiseless system, such that

$$\int R P_{\pm 1}(R)\,\mathrm{d}R = R_{\pm 1}.$$

If the PDFs have a small overlap, it is possible to determine the qubit state from a single measurement, a process called single shot readout. In the present case of dispersive readout, the PDFs overlap almost completely because the noise power introduced by the amplification chain exceeds the readout signal power by one to two orders of magnitude, as discussed in section 3.2.3. The system can thus not determine the qubit state from a single measurement, but can only determine its ensemble average value over many repetitions. The outcome of each repetition is drawn from one of the two PDFs with weights equal to the probabilities $p_{-1} = (1 - r_z)/2$ to find the qubit in the excited state and $p_1 = 1 - p_{-1} = (1 + r_z)/2$ to find the qubit in the ground state, where r_z is the z component of the Bloch vector introduced in Eq. 2.21. The ensemble average is thus a linear interpolant between R_1 and R_{-1},

$$\begin{aligned} R &= \int R\left[p_1 P_1(R) + p_{-1} P_{-1}(R)\right]\,\mathrm{d}R \\ &= (1 - p_{-1})R_1 + p_{-1}R_{-1} \\ &= \frac{R_1 + R_{-1}}{2} + \frac{R_1 - R_{-1}}{2}\, r_z, \end{aligned}$$

and it is sufficient to measure the response for any two different qubit states with well known values of r_z to calibrate the whole scale. In particular, the detailed frequency characteristics of the readout resonator do not play a role for calibration.

The first calibration point is attained by not applying any excitation, which amounts to leaving the qubit in its ground state, and identifying the measured value R_1 with $r_z = 1$. The second calibration point could be found by applying a pulse that prepares the excited state of the qubit, and

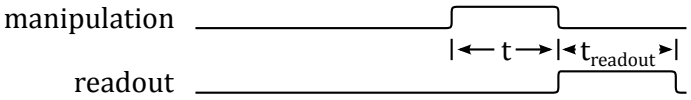

Figure 4.8: Pulse sequence of a Rabi experiment.

identifying the measured value R_{-1} with $r_z = -1$. This requires a careful calibration of the pulse and is not robust against errors. Instead, the qubit is driven for a time $T \gg \gamma_1^{-1}, \gamma_2^{-1}$ such that the measurement ensemble is in the incoherent steady state $r_{*,z}$. The value of $r_{*,z}$ can be calculated from Eq. 4.3 if at least two different driving amplitudes are measured or by making the driving amplitude sufficiently large such that $r_{*,z} = 0$ to a good approximation.

Experimental Observation of Rabi Oscillations

To manipulate a qubit's state, its transition frequency is first found by two-tone spectroscopy. Subsequently, manipulation pulses of variable duration are applied at or close to this frequency. After a few ns delay, the readout signal is sent to the qubit to determine its state at the end of the manipulation. The pulse sequence is depicted in Fig. 4.8 By varying the duration, amplitude, phase and frequency of the manipulation pulses, the qubit's response can be compared to the various theoretical predictions made by equations 2.17 and 4.2.

The data presented in Figure 4.9 shows the pulse duration and pulse amplitude dependence of the response of qubit #2, measured at its symmetry point. Each of the six plots on the top shows the excited state occupation probability $p_{-1} = (1 - r_z)/2$ against the duration of the driving pulse. The solid lines are fits of Eq. 4.2 to the data. While the manipulation pulse is on, the state rotates around the x axis of the Bloch sphere, oscillating from the ground state to the excited state and back. The total rotation angle is proportional to the duration of the excitation pulse. According to Eq. 2.18, the oscillation frequency and therefore the total rotation angle is also proprotional to the amplitude of the excitation pulse. Linear regression of the oscillation frequency vs. probe amplitude, shown in the bottom plot of Fig. 4.9, confirms this.

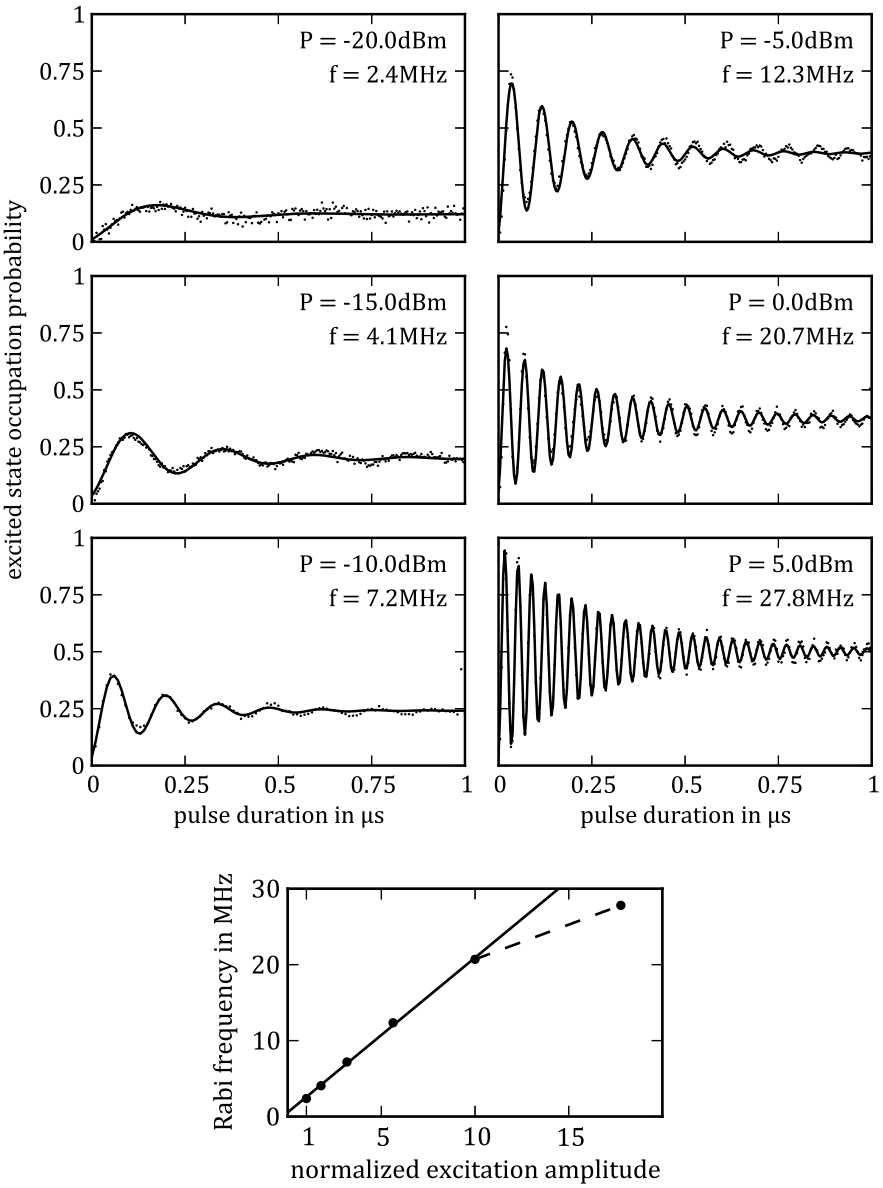

Figure 4.9: Excitation power dependence of Rabi oscillations of Qubit #2. (top) Individual Rabi curves for various powers. (bottom) Fit of the observed Rabi frequency to Eq. 2.18. Up to a mixer input of 0 dBm, the Rabi frequency increases linearly with excitation power, at larger powers the mixer saturates and the amplitude delivered to the qubit is reduced.

device	2	3	4	5	6	unit
$\omega/2\pi$	6.370	4.414	6.164	5.808	5.094	GHz
$\overline{\gamma}^{-1}$	309	717	220	748	388	ns
$\delta\overline{\gamma}^{-1}$	9	59	12	62	43	ns

Table 4.4: Decay times of Rabi oscillations of qubits #2–#6 at their symmetry points. Best result out of several measurements. See also section 4.2.2.

Due to decoherence effects, the oscillations decay with a time constant of $\overline{\gamma}^{-1}$, where $\overline{\gamma}$, defined by Eq. 4.4, is the arithmetic mean of the transversal and longitudinal decay rates. While it is not possible to individually determine the values of γ_1 and γ_2 from this type of measurement alone, it puts an upper limit of $2\overline{\gamma}$ on both. The decay times $T_{\mathrm{Rabi}} = \overline{\gamma}^{-1}$ are summarized in Table 4.4.

Figure 4.10a shows the response of qubit #2 to driving at different frequencies. If the microwave drive is not resonant with the transition frequency of the qubit, the rotation vector acquires an additional component Ω_z equal to the difference of the transition and driving (angular) frequencies. In Rabi oscillations, this manifests itself in an increased rotation frequency, the generalized Rabi frequency Eq. 2.19. The experimentally measured oscillation frequencies as well as a fit to the hyperbolic dependence expected from Eq. 2.19 is plotted in Fig. 4.10b. Furthermore, the rotation axis is now tilted with respect to the x-y plane. Therefore the qubit, initially in the ground state, can not reach the excited state. The minimum of r_z increases towards 1 as the frequency difference is increased, plotted in Fig. 4.10c including a fit of the expected minimum Eq. 2.20 to the experimental data. The decay rate of the oscillations is found to be lowest at resonance and fall off to a constant value for large detunings, as shown in Fig. 4.10d.

Quantum State Tomography

Since both the equations of motion Eq. 4.1 and the initial state, the ground state, are invariant under rotations around the z axis, changing the phase of the microwave drive does not affect the Rabi oscillations presented in

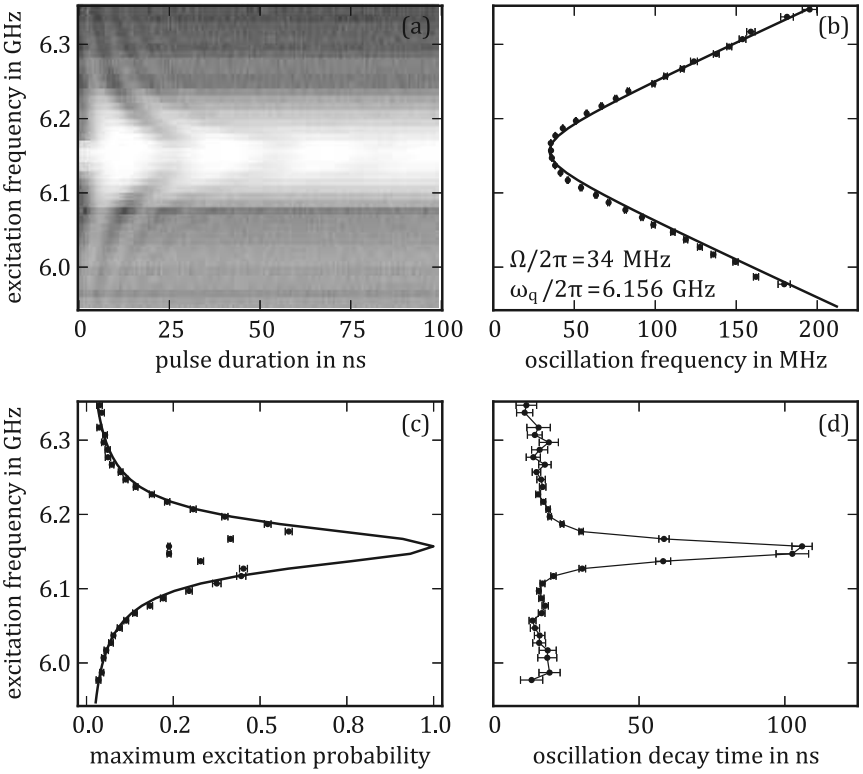

Figure 4.10: Off-resonant Rabi driving of qubit #2. a) Phase response of resonator #2 while driving qubit #2 close to its transition frequency. Darker (lighter) color indicates a lower (higher) excited state occupation probability. b) Frequency of the oscillations vs. driving frequency. The oscillation frequency is minimum when the driving frequency is resonant with the qubit transition and grows as $\left(\Omega^2 + (\omega_q - \omega_d)^2\right)^{1/2}$ with increasing detuning. c) The theoretically expected oscillation amplitude is maximum at zero detuning (rotation around the x axis) and decreases with increasing detuning (rotation axis tilted towards the z axis). The lower amplitude that was experimentally observed close to resonance is due to residual driving during qubit reset and readout. d) The oscillations decay faster towards larger detunings as the influence of $\gamma_2 \gg \gamma_1$ increases.

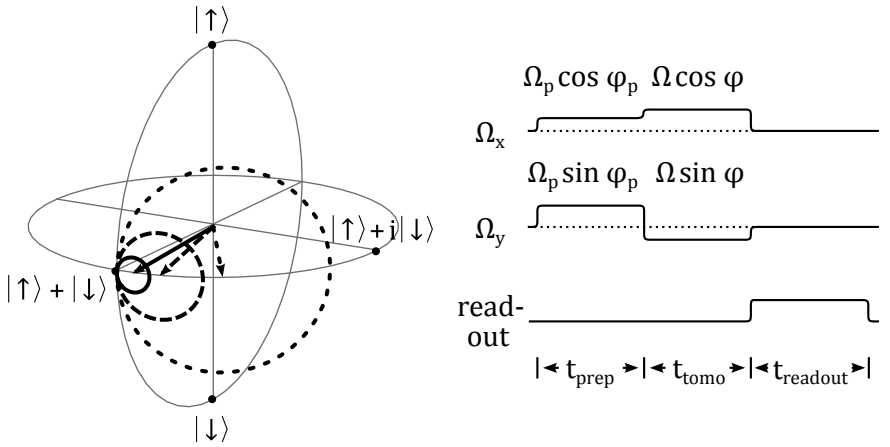

Figure 4.11: (left) Illustration of the evolution of the initial state $(|\uparrow\rangle + |\downarrow\rangle)/\sqrt{2}$ during radial state tomography. (right) Pulse sequence of the tomography process.

the previous section. Only when a sequence of at least two pulses with different phases is applied, this symmetry can be broken. The first pulse defines the (rotating) reference frame of the qubit and is typically set to be a rotation around the x axis. The second pulse rotates the spin vector around a different axis within this reference frame.

A pulse sequence to demonstrate the effect of changing the relative phase between two pulses is shown on the right-hand side of Figure 4.11. To control the phase, the I and Q inputs of a two-quadrature mixer (see section 3.4.1) are supplied with DC pulses of variable amplitude. The reference frame is chosen such that the I input of the mixer controls $\Omega_x = \Omega \cos\varphi$ and the Q input controls $\Omega_y = \Omega \sin\varphi$. The first pulse, with a duration of $t_{\mathrm{prep}} = 10\,\mathrm{ns}$, prepares the qubit by rotating it from the ground state to the desired initial state. The total rotation angle Ωt_{prep} is set by varying the amplitude on the I and Q inputs rather than the duration of the pulse. The amplitudes required for certain Ω_x and Ω_y are separately calibrated for the I and Q channels by measuring Rabi oscillations. The second pulse, also with a duration of $t_{\mathrm{tomo}} = 10\,\mathrm{ns}$, rotates the state around a different axis in the x-y plane.

The left-hand side of Figure 4.11 illustrates the evolution of the Bloch vector $\vec{r}$ corresponding to the initial state $|\uparrow, x\rangle = (|\uparrow\rangle + |\downarrow\rangle)/\sqrt{2}$ for different rotation axes. If direction of $\vec{r}$ and $\vec{\Omega}$ coincide, $\vec{r}$ is invariant under the rotation. The larger the angle (acutally $|\vec{r}/r \times \vec{\Omega}/\Omega|$) between $\vec{r}$ and $\vec{\Omega}$, the larger is the circle described by $\vec{r}$ on the Bloch sphere.

Figure 4.12 demonstrates the effect of varying the amplitude and phase of the second pulse, or, equivalently, of varying the orientation of its rotation axis and total rotation angle for different initial states. The polar angle represents the phase φ of the second pulse and the radius represents the total rotation angle generated by the pulse, subject to calibration. The grey scale indicates the excited state occupation probability at the end of the second pulse, with dark colors indicating low excitation probabilities and light colors indicating high excitation probabilities. The plots on the left-hand side show experimentally measured data, the plots on the right-hand side show the response expected from theory.

In Figs. 4.12a and 4.12d the qubit is initialized in the ground state and excited state, respectively. In these cases, the angle between $\vec{r}$ and $\vec{\Omega}$ is independent of φ, and the plots are expected to be rotationally symmetric. The experimental data does not completely measure up to this expectation, showing an increased Ω towards 270°. This is indicative of the mixer producing an amplitude error in the microwave pulse, which can be compensated for by calibrating the mixer for a larger number of angles instead of just 0° and 90°, as done here. In Figs. 4.12b and 4.12c the qubit is initialized in the $|\uparrow, y\rangle$ and $|\uparrow, x\rangle$ states along the y and x axis, accordingly. In these plots, the dependence of the oscillations on the relative angle between $\vec{r}$ and $\vec{\Omega}$ can be seen.

Because the readout system can only measure the projection of the Bloch vector on the z axis, rotations around the x and y axes are used to find the other projections. A $\pi/2$ rotation around the x axis exchanges the y and z axes, enabling the measurement of r_y. A $\pi/2$ rotation around the y axis exchanges the x and $-z$ axes, enabling the measurement of r_x. The process of measuring all components of the Bloch vector $\vec{r}$ is called quantum state tomography[SAM+06].

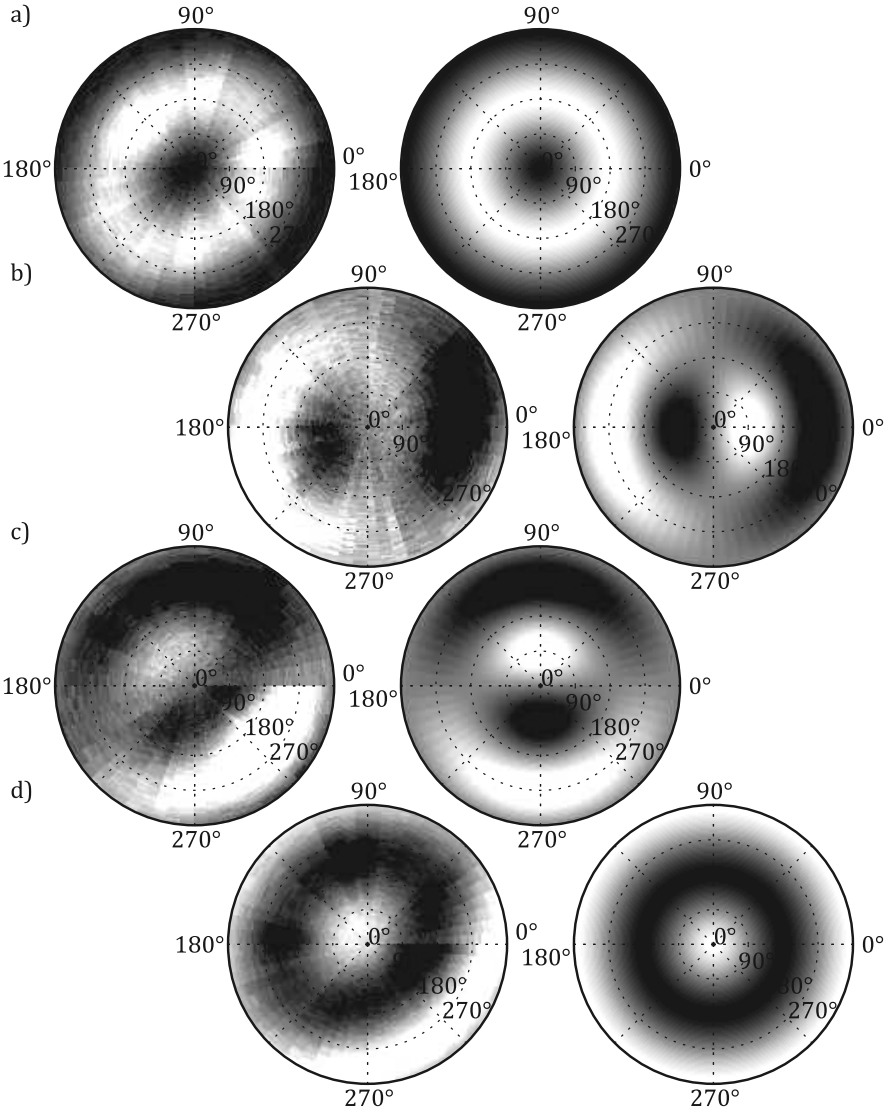

Figure 4.12: Radial state tomography of qubit #2. After preparing the qubit state, rotations around different axes in the x-y plane are performed. Prepared states are a) $|\uparrow\rangle$, b) $(|\uparrow\rangle + |\downarrow\rangle)/\sqrt{2}$, c) $(|\uparrow\rangle + i|\downarrow\rangle)/\sqrt{2}$, d) $|\downarrow\rangle$. Left-hand plots show experimental data, right-hand plots are simulated. The color scale indicates the excited state occupation probability (dark = low), the polar angle indicates the direction of the rotation axis, and the radius indicates the rotation angle.

4.2.2 Measuring Decoherence

Introduction

The longitudinal and transversal relaxation rates γ_1 and γ_2 or their inverses, the coherence times T_1 and T_2, are the two key dynamical parameters characterizing the fitness of a qubit for quantum computation. γ_1 is a measure of how fast the excited qubit relaxes to its ground state. γ_2 is a measure of how fast the knowledge of the phase, the crucial difference between quantum and classical information, is lost. The experimental determination of γ_1 will be detailed in the next section, different methods to determine γ_2 are found in the following sections.

In our case, γ_2 is what counts for quantum computation, because it limits the time available for operations. T_1 is also is important for two reasons: First, it limits the duration of a dispersive readout, shown in section 2.4.4, and therefore the maximum density of a frequency-division multiplexing system. This is discussed in section 2.5.3. Second, it limits T_2 due to the inequality $T_2 \leq 2T_1$ derived in section 2.2.7.

Longitudinal Relaxation

T_1 is measured by applying a π pulse to the qubit and varying the delay between the excitation and readout pulses, as shown in Fig. 4.13. Subsequently, Eq. 4.1 is fitted to the acquired $r_z(t)$ to extract T_1. If the parameters of the π pulse are not known, because Rabi oscillations have not been measured before, any initial state except the ground state can be used to measure T_1. The choice of a π pulse is simply a matter of convenience, because it maximizes the contrast of the decay curve.

We measured the decay times of qubits #2 to #6 at their symmetry points by applying a π pulse to each qubit and recording the amplitude response of its readout resonator. Qubits #1 and #7 were not measured

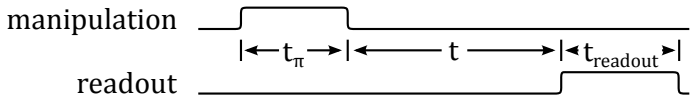

Figure 4.13: Pulse sequence of a T_1 measurement.

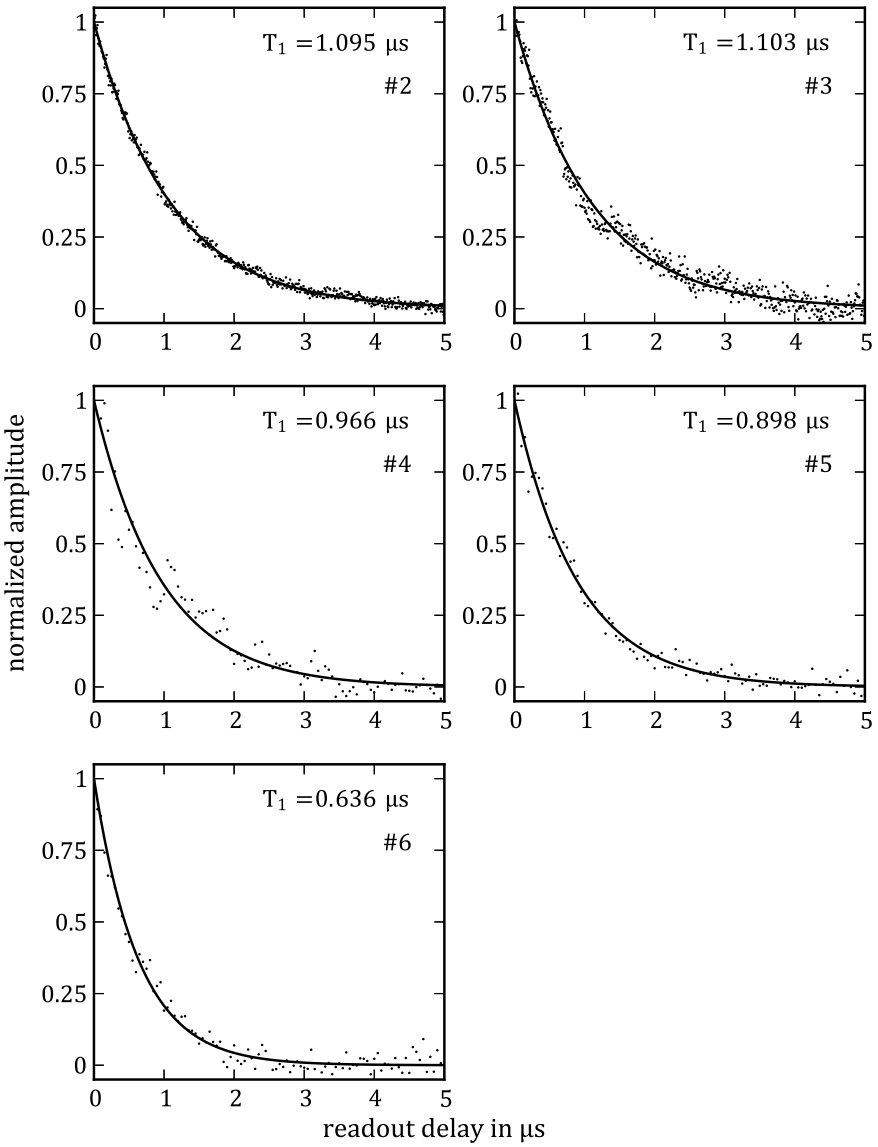

Figure 4.14: Measurements of the T_1 times of qubits #2 to #6 at their symmetry points. The x axis indicates the delay between the end of a π pulse exciting the qubit and the start of the readout process.

due to their low readout contrast which is a result of their smaller coupling to the readout resonator and large detuning from the resonator. The T_1 times of all measured qubits are about 1 μs, which is a typical value for similarly fabricated flux qubits. The measured decay curves are presented in Figure 4.14, and the T_1 values extracted from the curves are listed in Table 4.5.

device	2	3	4	5	6	unit
$\omega/2\pi$	6.370	4.414	6.164	5.808	5.094	GHz
T_1	1.095	1.103	0.966	0.898	0.636	μs

Table 4.5: Longitudinal relaxation times of qubits #2 to #6 measured at their symmetry points. The values are fits to the curves presented in Fig. 4.14.

Transversal Relaxation: Rabi Experiment

The result Eq. 4.4 for the decay rate $\overline{\gamma}$ of (resonant) Rabi oscillations allows the setting of an upper bound of the transversal relaxation rate γ_2, $\gamma_2 \leq 2\overline{\gamma}$. If the longitudinal relaxation rate has been separately measured, γ_2 can be calculated from $\overline{\gamma}$ and γ_1. The advantages of this method are its simplicity and robustness. Both measurements, Rabi and γ_1, require only a single gate operation on the qubit. Pulse amplitude and duration errors do not influence the measured $\overline{\gamma}$ and γ_1. The T_2 times of qubits #2 to #6 extracted this way are summarized in Table 4.6.

The measured γ_2 were not well reproducible and varied by a factor of up to three between different measurements taken within a span of one hour. At the same time, variations of the qubit transition frequency of the order of a few MHz could be seen, indicating an unstable flux bias. Any bias offset from the symmetry point results in net circulating currents around the qubit loop, which is opposite for the two basis states, as shown in Figure 2.4. External magnetic fields couple asymmetrically to the two states, changing their energy difference and causing dephasing.

In [KMS+07], $1/f$ noise in the bias flux was found to give the main contribution to dephasing in a flux qubit. The authors found that γ_ϕ was proportional to the bias offset $\Delta\Phi$ from $\Phi_0/2$. Adopting their treatment

device	2	3	4	5	6	unit
$\omega/2\pi$	6.370	4.414	6.164	5.808	5.094	GHz
$\overline{\gamma}^{-1}/2$	155	358	110	274	194	ns
$T_2 = \gamma_2^{-1}$	180	531	124	641	278	ns
Ω	8.7	58.9	11.6	62.0	42.9	MHz
$\overline{\gamma}^{-1}/2$	155	244	110	165	131	ns
$T_2 = \gamma_2^{-1}$	180	313	124	202	164	ns
σT_2	∞	173	1	186	92	ns

Table 4.6: T_2 times of qubits #2 to #6 at their symmetry points, calculated from the longitudinal and Rabi decay rates in Tables 4.5 and 4.4. The first set of values are the best results out of several measurements, the second set of values are the mean of these measurements.

to the parameters (geometric size and persistent current) of our qubits, a dephasing rate $\gamma_\phi = 15\,\mathrm{MHz/m}\Phi_0 \cdot \Delta\Phi$ is expected. At an offset of $250\,\mu\Phi_0$, causing an increase of the qubit transition frequency by 4 MHz from its minimum, this limits T_2 to 250 ns. These numerical values assume that the spectral density of flux noise is equal in [KMS+07] and our experiments. The high sensitivity to small offsets could very well explain the variance of γ_2 observed, and it emphasizes the necessity to optimize the magnetic shielding of the qubits.

A more in-depth study of decoherence of flux qubits[BGY+11] shows that $\overline{\gamma}$ is not a constant, but depends on the Rabi frequency Ω. As the driving amplitude is varied, the qubit samples the noise power spectral density of critical current noise $S^\Delta(\Omega)$ and of flux noise $S^\epsilon(\Omega)$. γ_2 extracted from this measurement is thus only unambiguously defined if the Rabi frequency at which it was measured is also given. It should be noted that the standard Ramsey and echo experiments presented in the following sections and more general dynamical decoupling sequences are likewise sensitive to different parts of the noise spectrum, depending on the overall time of the pulse sequences.

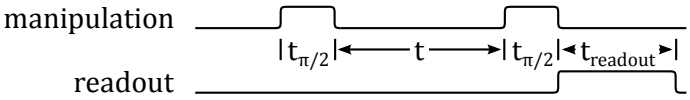

Figure 4.15: Pulse sequence of a Ramsey T_2 measurement.

Transversal Relaxation: Ramsey Experiment

The transversal relaxation rate can be measured directly using a sequence of two rotations, by means of a so-called Ramsey experiment[Ram50], sketched in Fig. 4.15. First, a $\pi/2$ pulse around the y axis (or any other axis in the x-y plane) is applied to the qubit. The pulse turns the Bloch vector $\vec{r} = \tilde{z}$ of the inital state into $\vec{r} = \tilde{x}$, on the equatorial plane of the Bloch sphere. After some time, during which decoherence processes take place, a second $\pi/2$ rotation around the same axis is applied. The second pulse transforms the x component of $\vec{r}$ into the $-z$ component and the z component into the x component. When finally r_z is measured, it contains information on the evolution of r_x in the time interval between the two pulses, which is an exponential decay with rate γ_2, as can be found from Eq. 4.1.

If the rotation pulses are detuned from the qubit transition, an additional precession of the state around the z axis takes place, which is seen as an oscillation in the r_x projection. A fixed detuning is often employed in this measurement, because slow oscillations, introduced by an accidential detuning, are hard to separate from γ_2 when fitting the experimental curve.

Figure 4.16 shows the results of a Ramsey measurement performed on qubit #6.The qubit was resonantly driven at 5070 MHz with a Rabi frequency of $\Omega/2\pi$ = 95.5 MHz, resulting in a duration of $\pi/2$ pulses of 2.6 ns. The low measured T_2^{Ramsey} time compared to Table 4.6 is a result of noise coupled by the unattenuated high-frequency bias line used in this measurement run.

Figure 4.17 shows Ramsey measurements performed on qubit #2 at various detunings of the drive from the qubit transition frequency. The expected linear dependence of the oscillation frequency on the detuning can be seen. Discrepancies from the theoretical curve at are due to bias instabilities.

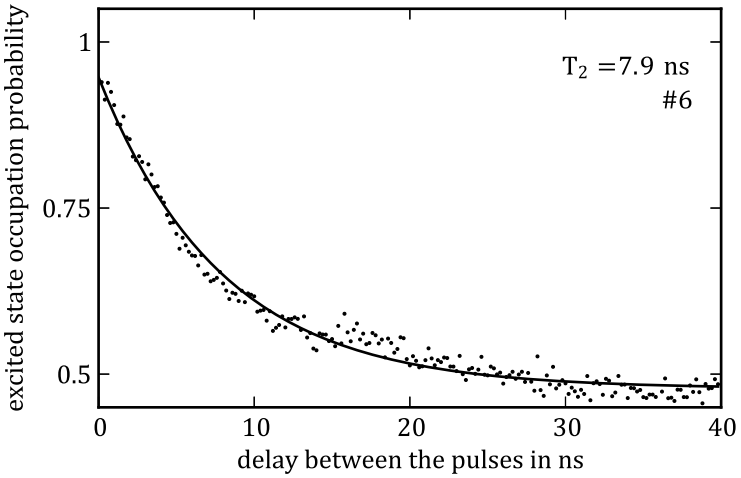

Figure 4.16: Ramsey experiment on qubit #6 at its symmetry point. The duration of a $\pi/2$ pulse was 2.6 ns.

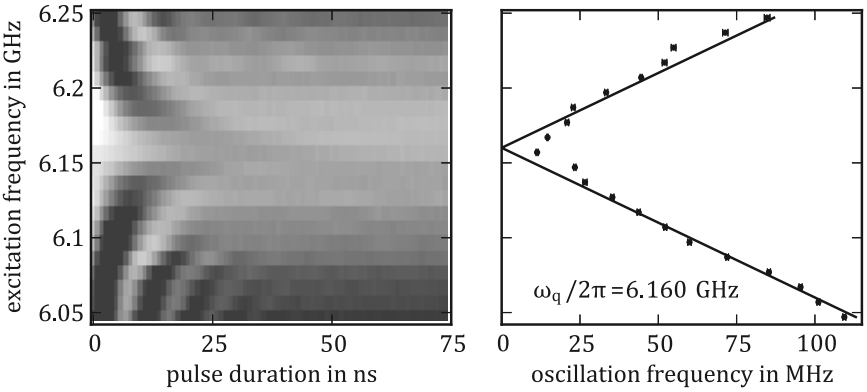

Figure 4.17: Off-resonant Ramsey experiment on qubit #2.a) Excited state occupation probability of qubit #2 vs. driving frequency. Lighter colors indicate higher probabilities. b) Frequency of the oscillations vs. driving frequency. The oscillation frequency is equal to the detuning between the qubit and drive.

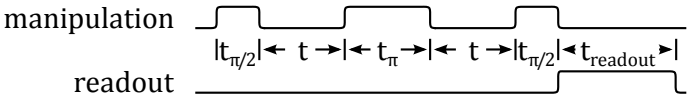

Figure 4.18: Pulse sequence of an echo T_2 measurement.

Transversal Relaxation: Spin Echo Experiment

A Hahn spin echo measurement[Hah50] is an improved method of measuring the transversal relaxation rate of a qubit that suppresses low-frequency noise. It uses a sequence of three pulses, shown schematically in Figure 4.18. As in the Ramsey experiment, the first pulse, initializes the Bloch vector to $\vec{r} = \tilde{x}$, and the last pulse projects r_x onto the z axis. The second pulse, a π pulse, inverts the sign of r_x but not of r_y, effectively inverting the sign of the polar angle of the Bloch vector. A phase acquired during the evolution between the first and second pulses is canceled by the evolution between the second and third pulses, given that the evolution time and precession frequencies are the same. The echo sequence will thus cancel the effect of fluctuations of the qubit transition that are slow on the time scale of a single repetition of the experiment, that would otherwise degrade the average over many repetitions. It has no effect on fluctuations on shorter time scales.

Figure 4.19 shows the results of a spin echo experiment performed on qubit #6.The qubit was resonantly driven at 5070 MHz with a Rabi frequency of $\Omega/2\pi$ = 95.5 MHz, resulting in a duration of 2.6 ns of the $\pi/2$ pulses and 5.2 ns of the π pulse. The $T_2^{\text{echo}} = 41.4$ ns measured using the spin echo technique is about five times larger than the $T_2^{\text{Ramsey}} = 7.9$ ns measured using the simple Ramsey technique. This indicates that low frequency noise contributes significantly to the total dephasing in this setup. For comparison, $T_2^{\text{Rabi}} = 11.9$ ns was also measured, and found to coincide with T_2^{Ramsey} reasonably well.

Figure 4.20 shows a spin echo experiment performed on qubit #2 at various detunings of the driving and qubit transition frequencies. Like in the detuned Ramsey experiment in Figure 4.10, the oscillation frequency is equal to the detuning. The oscillations decay slower than in the Ramsey

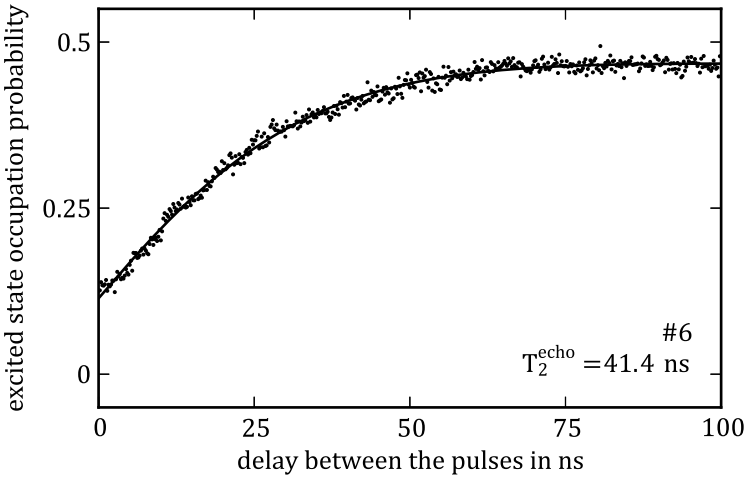

Figure 4.19: Spin echo experiment on qubit #6 at its symmetry point.Because the total duration of the experiment is two times the delay between the pulses, the decay is proportional to $\exp(-2t/T_2^{\text{echo}})$. T_2^{echo} is substantially longer than the T_2 extracted from the Ramsey measurement Fig. 4.16, indicating that low frequency noise significantly contributes to the total dephasing.

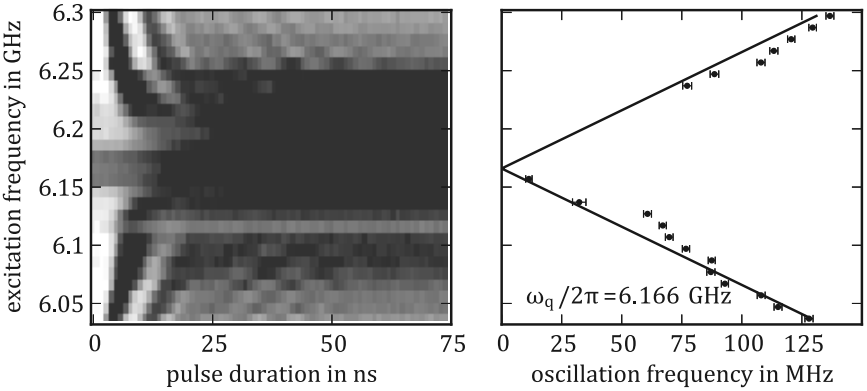

Figure 4.20: Off-resonant spin echo experiment. a) Excited state occupation probability of qubit #2 vs. driving frequency. Lighter colors indicate higher probabilities. b) Frequency of the oscillations vs. driving frequency. The oscillation frequency is equal to the detuning between the qubit and drive.

experiment, indicating that the echo sequence also counteracts dephasing in the off-resonant case.

4.3 Parallel Qubit Measurements

4.3.1 Setup and Steady-State Measurements

Setup of the Readout System

Parallel dispersive readout of multiple qubits amounts to simultaneous probing of multiple resonators. Our readout system handles this in a scalable manner, using a high-speed DAC combined with a conventional microwave generator and a two-quadrature mixer (see Fig. 3.10 on page 71 for details about the hardware setup). The DAC is setup to synthesize a burst containing the baseband frequencies $\omega_r/2\pi - f_{\mathrm{LO}}$ of all resonators to be probed. The following two-quadrature mixer shifts the frequencies up by the generator frequency f_{LO} to the actual resonance frequencies.

Probing of all seven resonators on the sample requires a readout bandwidth of $\omega_r(\#7)/2\pi - \omega_r(\#1)/2\pi = 949\,\mathrm{MHz}$. By following the relative phase of the I and Q quadratures, a two-quadrature mixer can distinguish between positive and negative baseband frequencies, so two channels with a bandwidth of 475 MHz each are necessary. This is easily handled by the 6 GS/s DAC, but the analog frontend of the 1 GS/s ADC used has a somewhat lower bandwidth, which limits the number of resonators that can be probed simultaneously to six out of the seven on the sample. Since the ADC used can acquire two channels only up to 500 MS/s (250 MHz), only the I quadrature was recorded when faster sampling rates were required. In the latter case, the receiver can no longer discriminate the signs of the baseband frequencies, so their moduli have to be different.

To test the parallel readout, we performed a flux sweep similar to Fig. 4.2, but acquired by the multiplexing readout setup instead of a network analyzer. The reference generator was set to $f_{\mathrm{LO}} = 9720.3\,\mathrm{MHz}$, and the DAC was programmed to output tones at -405.7 MHz, -259.7 MHz, -104.2 MHz, 55.3 MHz, 216.08 MHz and 375.7 MHz. After up-conversion, this translates to the resonance frequencies of resonators #1 to #6, with

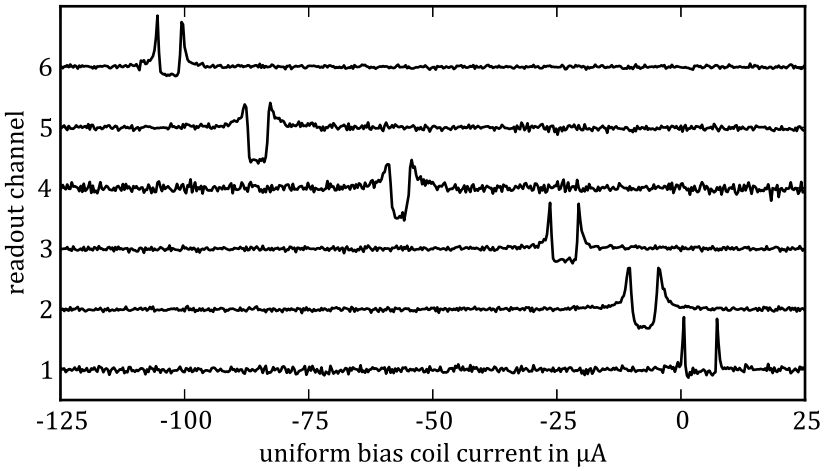

Figure 4.21: Simultaneous measurement of the response of resonators #1 to #6 to a sweep of the main bias coil.

the dispersive shift due to every qubit at its symmetry point already taken into account. Figure 4.21 shows the normalized amplitude response of the acquired baseband tones to a sweep of the main bias coil. The amplitude of each tone remains constant as long as the qubit and resonator are far detuned, increases strongly close to the qubit–resonator avoided level crossings, and varies weakly close to the symmetry point of each qubit, where the slope of the transition frequency vs. magnetic flux is small. The curves can be understood as horizontal cross-sections through the equivalents of Fig. 4.3 for each device.

Gradient Coil Calibration

Due to a variable, cooldown-dependent offset of the flux bias seen by each qubit, the main bias coil alone is not sufficient to bias more than one qubit into a working regime at the same time. The simplest solution to this issue is the addition of on-chip bias lines that provide a local flux bias to each qubit. This has been integrated in later chip designs but not in the original multiplexing sample, whose layout was kept as simple

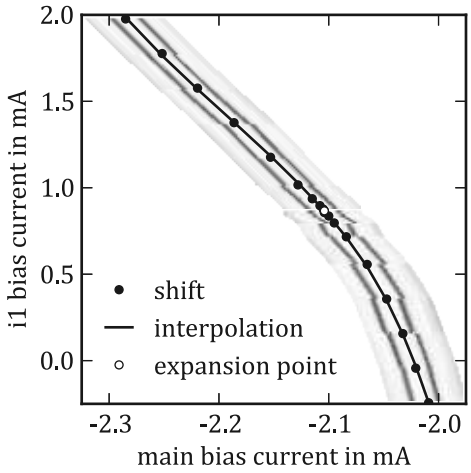

Figure 4.22: Gradient coil calibration via the bias shift of qubit #4 introduced by gradient coil i_1. The grayscale background shows the acquired curves, whose double-peak structure originates from a spectroscopy tone at 6,189 MHz coinciding with the qubit transition frequency. The black markers and solid line indicate the calculated shift between the curves.

as possible. Instead, additional bias coils, arranged as shown in Fig. 3.5, were attached to the inside of the sample compartment.

The additional coils were calibrated by repeatedly sweeping the main bias coil, changing the current through the other coil in between sweeps. A continuous wave spectroscopy tone at a fixed frequency well above the qubit gap was applied to the qubit to introduce a pair of symmetric markers to the measured curve. The measurement software would then calculate the change of the current in the main bias coil necessary to cancel the change of magnetic flux introduced by the other coil through cross-correlation of the traces. The software controls the whole calibration process, automatically choosing the step size between data points depending on the error made in the previous step. This allowed for a precise measurement of the mutual inductances of each (coil, qubit) pair in a minimum amount of time and without sending large currents through the coils, although their absolute values differ by two orders of magnitude. An example calibration run is shown in Figure 4.22.

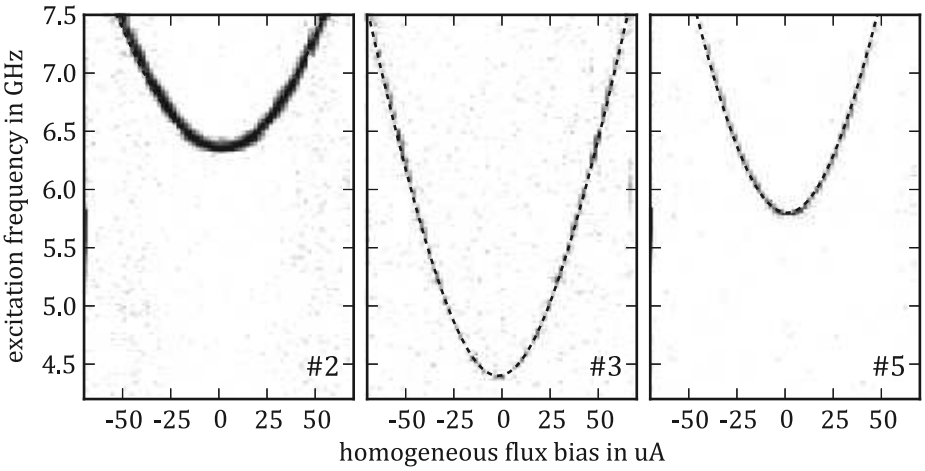

Figure 4.23: Simultaneously measured spectra of multiple qubits. The gradient coils are setup such that the symmetry points of qubits #2, #3 and #5 coincide for a certain field generated by the main bias coil. A single continuous wave microwave tone and the field of the main bias coil are swept. The readout resonators are probed simultaneously every $10\,\mu s$. In each of the plots, dark color indicates an excitation of the corresponding qubit.

Because of the large distance between the coils and qubits, each coil couples to every qubit. Changing the bias of a single qubit while leaving the biases of the other qubits unchanged was done by linearly expanding the mutual inductance functions an solving the linear equation $\vec{\Phi} = M \cdot \vec{I}$. Because the components of M^{-1} also differ by orders of magnitudes, the biasing process had to be iterated. Using this method, it was possible to bias up to three qubits close to their symmetry points at the same time.

Simultaneous Qubit Spectroscopy

Once the electronics for multiplexed readout and the gradient coils are set up, the simultaneous measurement of multiple qubit spectra is as simple as the measurement of a single spectrum, already discussed in section 4.1.2. The spectra of qubits #2, #3 and #5, measured simultaneously, are shown in Figure 4.23.

Data is acquired by the multiplexed readout setup instead of the network analyzer. Because the measurement computer can not sustain the 1 GB/s of data produced by the data converters in the acquisition board, transmission was only measured for 512 ns every 10 µs, reducing the data rate to 51 MB/s. This duty cycle of 5% results in a 20-fold increased measurement duration with the multiplexed readout setup compared to the network analyzer, to obtain the same amount of statistics. Due to the relatively large coupling Q_L^{-1} between the readout resonators and feedline however, the averaging time is negligible compared to the time it takes to sweep the coil and generator, and the overall duration is the same for both acquisition methods.

All qubits were driven through the readout line from the same microwave generator. As long as the drive is not resonant with any of the readout resonators, only a portion of $O(Q_L^{-1})$ of the drive reaches each qubit, and the interaction of the drive with one qubit has no influence on the others.

4.3.2 Dynamics Measurements

Simultaneous Coherent Oscillations

To induce coherent oscillations in multiple qubits, it is necessary to provide microwave drives close to the transition frequency of each qubit. This requirement ensues from Eq. 2.20, which links the σ_z amplitude of Rabi oscillations to the detuning of the drive. For the parallel measurement of qubits #2, #3 and #5 presented in Fig. 4.24, this meant driving pulses at 6365 MHz, 4400 MHz and 5822 MHz. Each frequency was generated by an individual microwave source and gated by a mixer connected to a DAC channel, similar to Fig. 3.11d on page 74.

The combined driving signal was applied through the readout line, so each qubit was simultaneously driven by all three microwave tones. In the frame of each qubit, the off-resonant tones induce rotations around an axis in the x-y plane that is not fixed but rotates itself around the z axis with the frequency of the detuning. The additional drivings thus result in small oscillations at the frequencies of the detunings, superimposed on the oscillation induced by the resonant drive. However, in Figure 4.24

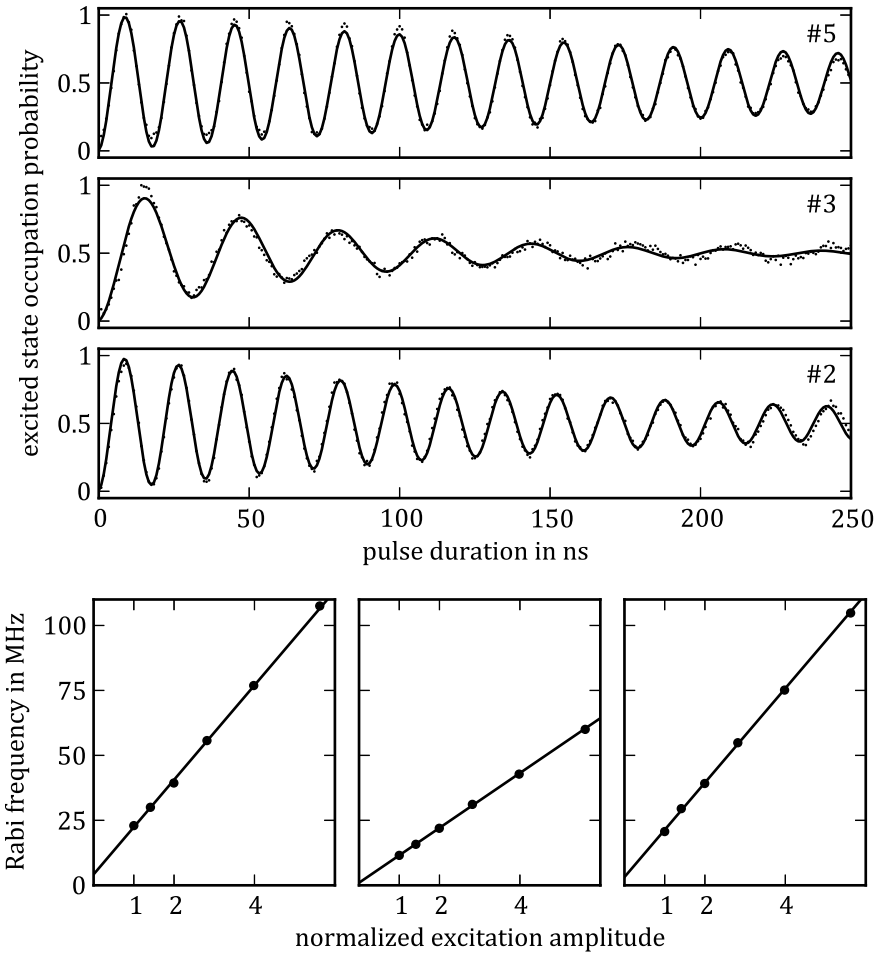

Figure 4.24: Simultaneously measured Rabi oscillations of multiple qubits. Driving pulses at $\omega_2 = 6365\,\mathrm{MHz}$, $\omega_3 = 4400\,\mathrm{MHz}$ and $\omega_5 = 5822\,\mathrm{MHz}$ are applied to all qubits through the common feedline. (top) Time-traces measured at $P_2 = -18\,\mathrm{dBm}$, $P_3 = -9\,\mathrm{dBm}$, $P_5 = -15\,\mathrm{dBm}$ driving power. (bottom) Driving amplitude dependence of the Rabi frequencies.

the superimposed oscillations induced into qubit #2 by the drive of qubit #5 and vice versa can not be seen, even though their frequencies were below the sampling limit of 600 MHz determined by the spacing of the data points. Instead, they average out because the relative phase of the drives is not kept fixed between repetitions.

No significant deviations were observed between the data presented in Fig. 4.24 and the data presented earlier in Fig. 4.9. The expected linear dependence of the oscillation frequencies on the driving amplitudes could be reproduced. The absolute values are larger than before because of an amplifier introduced into the excitation signal path.

Simultaneous Application of Different Sequences to Multiple Qubits

With the largest version of the qubit manipulation setup, shown in Fig. 3.11d on page 74, independent pulse sequences can be generated for all qubits. Figure 4.25 shows the results of such an experiment performed on qubits #2, #3 and #4. Three different manipulation sequences are combined and sent to the sample through the readout line: A Ramsey pulse sequence, Fig 4.15, at a frequency of $\omega_2/2\pi = 6415\,\mathrm{MHz}$, close to the transition of qubit #2. A T_1 sequence, Fig 4.13, at a frequency of $\omega_3/2\pi = 4400\,\mathrm{MHz}$, resonant with the transition of qubit #3. A Rabi sequence, Fig 4.8, was applied at $\omega_5/2\pi = 5822\,\mathrm{MHz}$, resonant with the transition of qubit #5.

The overall shape of the curves is what is expected as the outcome of the individual experiments. The T_1 time of 815 ns measured for qubit #3 is within 30% of the value reported in Table 4.5. The T_2 times of 13.6 ns of qubit #2 and 23.9 ns (extracted using Eq. 4.4) of qubit #5 are much lower than the values obtained previously during this run. In case of qubit #5 the culprit is most likely dephasing resulting from the flux bias being $1.1\,\mathrm{m}\Phi_0$ away from its symmetry point[KMS+07]. In case of qubit #2 an additional effect plays a greater role, as its spectral line, shown in Fig. 4.23, is also widened at its symmetry point. It should be noted that spectra taken previously using the same (parallel) method did not show this widening. Also, the readout system can not disturb the qubit states, as it does not output any signals during the pulse sequences.

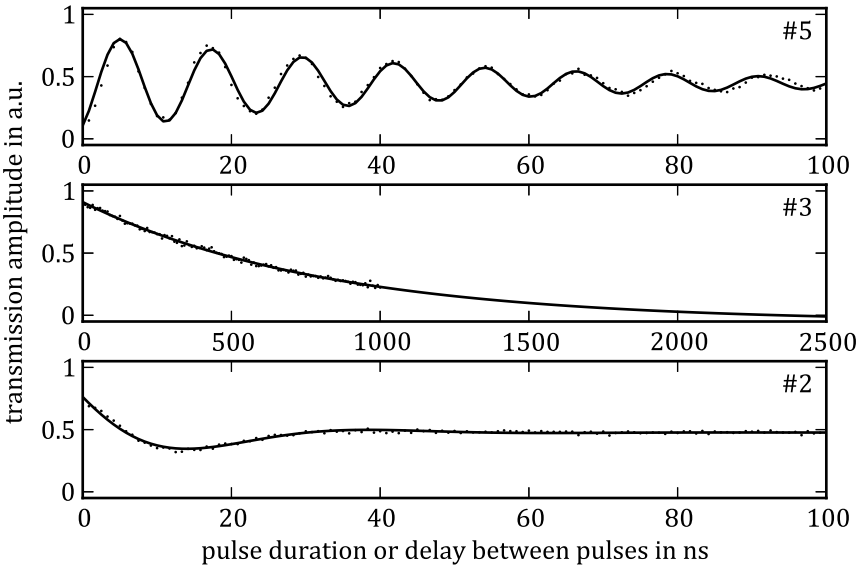

Figure 4.25: Simultaneous execution of different sequences on qubits #2, #4 and #5. A Ramsey T_2 measurement is performed on qubit #2, at $\omega_2 = 6415$ MHz. A T_1 measurement is performed on qubit #3, at $\omega_3 = 4400$ MHz. A Rabi oscillation measurement is performed on qubit #5 at $\omega_5 = 5822$ MHz. Fits to the curves give $T_2 = 13.6$ ns and a detuning of 20.5 MHz for qubit #2, $T_1 = 815$ ns for qubit #3 and a Rabi decay time $\overline{\gamma}^{-1} = 47$ ns for qubit #5.

For many simple experiments, especially for serial characterization of qubits, the approach of sending qubit manipulation sequences through the readout line is sufficient. When going to multi-qubit algorithms, it has its shortcomings, because the sum of all manipulation tones is seen by all qubits. Simultaneously performed gates mutually reduce their fidelity once the frequency separation of the qubits becomes smaller than a few times the Rabi frequency – fast, high-fidelity gates preclude a high packing density and vice versa. It needs to be investigated if ideas from optimal control theory, which have been employed to improve gate fidelity and suppress transitions out of the qubit subspace in weakly anharmonic qubits[CDG+10], can reduce or completely cancel the detrimental effects of the additional drives. A second, rather technical, weakness of the

approach is that broadband circulators are required to stop reflections at the input the readout amplifier from travelling back to the sample and inducing further qubit rotations. By separating the excitation and readout lines, with the excitation line terminating at the sample, this can be easily avoided.

Conclusion and Outlook

This thesis presents a technique to simultaneously measure the state of an arbitrary number of superconducting qubits using minimal resources, by frequency multiplexing the qubit signals on a single transmission line. Each qubit is furnished with an individual microwave resonator, which experiences a state-dependent frequency pull due to the qubit-resonator interaction. All resonators are connected to a common on-chip transmission line, through which their resonance frequencies are probed and hence the states of the qubits are read out.

With a narrow-band homodyne detection setup, which is now standard for groups working in the field, each qubit can be separately measured. This is already very useful, because it allows characterization of many devices in a single refrigerator run, through a single line. Since microwaves travel freely along the line outside the bandwith of the readout resonators, several chips can even be connected in series. Serially performed characterization measurements, such as qubit spectra, decay and dephasing times, are presented in sections 4.1 and 4.2.

However, the full power of the readout system lies in providing simultaneous and independent readouts of all qubits. When multiple frequency components, one for every resonator to be probed, are transmitted through the sample, the state of each qubit is encoded onto the corresponding component. The experimental setup (Fig. 3.10) developed in this thesis borrows ideas from software-defined radio to generate and detect signals with an arbitrary number of frequency components within a bandwidth of about 1 GHz, thus allowing an almost arbitrary number of qubits to be read out simultaneously. In section 4.3, we present measurements performed on up to six qubits in parallel using this technique.

Calculations in section 2.5 show that co-channel interference depends mostly on the frequency difference between adjacent channels and is almost independent of their overall number. The primary parameter

restricting the distance between channels is the loaded linewidth of the readout resonators, which are strongly coupled to the measurement line in order to speed up the measurement. According to the simulation results for $N = 100$ channels (Fig. 2.17), a spacing of 2 linewidths is sufficient for interference to be less than -10 dB, and a spacing of 6.5 linewidths further reduces interference to -20 dB. The resonators realized on our sample have linewidths of approximately 6 MHz, theoretically allowing 80 channels per GHz of bandwidth at -10 dB crosstalk or 25 channels at -20 dB crosstalk.

In its current implementation, the main drawback of the readout is that it is not single shot. With noise temperatures of several Kelvins, commercially available cryogenic amplifiers add several noise photons to each signal photon. For a single resonator, the solution to this problem is the use of parametric amplifiers based on Josephson junctions, which feature a close to the quantum limited noise performance. Our circuit is especially suited to be integrated with such an amplifier, due to the large change of the amplitude ratio and phase of the transmitted signal, which are proportional to the intrinsic instead of the loaded quality factor as in standard setups. Unfortunately, the gain-bandwidth product of typical parametric amplifiers is only a few tens of MHz, so a separate amplifier would have to be included for each readout channel. For many-channel systems, a bifurcation readout similar to what has been demonstrated for transmon qubits[MOPL+09] is a more viable solution. Through the inclusion of a Josephson junction, each readout resonator is made nonlinear and can then be driven such that it latches the state of the qubit. Single-shot readout becomes possible because the duration of the readout is no longer limited by the decay time of the qubits and the bandwidth of the detector can be reduced until the amplifier noise is below the signal. Future improvements of the readout will aim in this direction.

Recently, new samples that include both multiplexed readout and qubit-qubit interactions mediated by an additional high-Q bus resonator have been manufactured. These samples will allow the demonstration of two-qubit quantum gates, and will be the first real quantum computer operated at KIT.

References

[Abr57] A. A. Abrikosov. "On the Magnetic Properties of Superconductors of the Second Group". In: *J. Exp. Theor. Phys.* 5 (1957), p. 1174 (cit. on p. 58).

[Agi] *Agilent Technologies, Inc.* URL: http://www.agilent.com/ (cit. on p. 75).

[Anr] *Anritsu Corporation*. URL: http://www.anritsu.com/ (cit. on p. 66).

[Atl] *Atlantic Microwave Ltd.* URL: http://www.atlantecrf.com/ (cit. on p. 75).

[AT55] S. H. Autler and C. H. Townes. "Stark Effect in Rapidly Varying Fields". In: *Physical Review* 100 (1955), pp. 703–722. DOI: 10.1103/PhysRev.100.703 (cit. on p. 43).

[BCS57] J. Bardeen, L. N. Cooper, and J. R. Schrieffer. "Microscopic Theory of Superconductivity". In: *Physical Review* 106 (1957), pp. 162–164. DOI: 10.1103/PhysRev.106.162 (cit. on p. 7).

[BHW+04] Alexandre Blais, Ren-Shou Huang, Andreas Wallraff, S. M. Girvin, and R. J. Schoelkopf. "Cavity quantum electrodynamics for superconducting electrical circuits: An architecture for quantum computation". In: *Phys. Rev. A* 69.6 (2004), p. 062320. DOI: 10.1103/PhysRevA.69.062320 (cit. on pp. 38, 41, 44–46).

[Blo46] F. Bloch. "Nuclear Induction". In: *Phys. Rev.* 70 (7-8 1946), pp. 460–474. DOI: 10.1103/PhysRev.70.460 (cit. on p. 23).

[BVJ+98] V. Bouchiat, D. Vion, P. Joyez, D. Esteve, and M. H. Devoret. "Quantum coherence with a single Cooper pair". In: *Physica Scripta* T76 (1998), pp. 165–170. DOI: 10.1238/Physica.Topical.076a00165 (cit. on p. 10).

[BR04] J.R. Bray and L. Roy. "Measuring the unloaded, loaded, and external quality factors of one- and two-port resonators using scattering-parameter magnitudes at fractional power levels". In: *Microwaves, Antennas and Propagation, IEE Proceedings* - 151.4 (2004), pp. 345–350. ISSN: 1350-2417. DOI: 10.1049/ip-map:20040521 (cit. on p. 33).

[BGY+11] J. Bylander, S. Gustavsson, F. Yan, F. Yoshihara, K. Harrabi, G. Fitch, D. G. Cory, Y. Nakamura, J.-S. Tsai, and W. D. Oliver. "Noise spectroscopy through dynamical decoupling with a superconducting flux qubit". In: *Nat. Phys.* 7 (7 2011), pp. 565–570. DOI: 10.1038/nphys1994 (cit. on p. 103).

[Car22] J. R. Carson. "Notes on the Theory of Modulation". In: *Proc. IRE* 10 (1922), p. 57. DOI: 10.1109/JRPROC.1922.219793 (cit. on p. 55).

[CDG+10] J. M. Chow, L. DiCarlo, J. M. Gambetta, F. Motzoi, L. Frunzio, S. M. Girvin, and R. J. Schoelkopf. "Optimized driving of superconducting artificial atoms for improved single-qubit gates". In: *Phys. Rev. A* 82 (4 2010), p. 040305. DOI: 10.1103/PhysRevA.82.040305 (cit. on p. 115).

[Cho10] Jerry Moy Chow. "Quantum Information Processing with Superconducting Qubits". PhD thesis. Yale University, 2010 (cit. on p. 60).

[Deu85] D. Deutsch. "Quantum Theory, the Church-Turing Principle and the Universal Quantum Computer". In: *Proc. R. Soc. Lond. A* 400.1818 (1985), pp. 97–117. DOI: 10.1098/rspa.1985.0070 (cit. on p. 2).

[Deu89] D. Deutsch. "Quantum Computational Networks". In: *Proc. R. Soc. Lond. A* 425 (1989), pp. 73–90. DOI: 10.1098/rspa.1989.0099 (cit. on p. 2).

[DiV09] D. P. DiVincenzo. "Fault-tolerant architectures for superconducting qubits". In: *Phys. Scr.* 2009 (2009), p. 014020. DOI: 10.1088/0031-8949/2009/T137/014020 (cit. on p. 4).

[DiV12] D. P. DiVincenzo. "Prospects for Superconducting Qubits". In: International School of Physics Ënrico Fermi" CLXXXIII: Quantum Spintronics and Related Phenomena. 2012. URL: http://static.sif.it:8080/SIF/resources/public/files/va2012/divincenzo_0626a.pdf (cit. on p. 3).

[Dol77] G. J. Dolan. "Offset masks for lift-off photoprocessing". In: *Applied Physics Letters* 31.5 (1977), pp. 337–339. DOI: 10.1063/1.89690 (cit. on p. 59).

[EH00] C. Enss and S. Hunklinger. *Tieftemperaturphysik*. Springer, Berlin, 2000. ISBN: 978-3540676744 (cit. on p. 37).

[Fey82] Richard P. Feynman. "Simulating physics with computers". In: *International Journal of Theoretical Physics* 21 (1982), pp. 467–488. ISSN: 0020-7748. DOI: 10.1007/BF02650179 (cit. on p. 1).

[FPC+00] J. R. Friedman, V. Patel, W. Chen, S. K. Tolpygo, and J. E. Lukens. "Quantum superposition of distinct macroscopic states". In: *Nature* 406 (2000), pp. 43–46. DOI: 10.1038/35017505 (cit. on p. 10).

[Fri44] H. T. Friis. "Noise Figures of Radio Receivers". In: *Proceedings of the IRE*. Vol. 32. 1944, pp. 419–422 (cit. on p. 65).

[GL50] V. L. Ginzburg and L. D. Landau. "On the theory of superconductivity". In: *Zh. Eksperim. i. Teor. Fiz.* 20 (1950), p. 1064 (cit. on p. 8).

[Gor59] L. P. Gor'kov. "Microscopic derivation of the Ginzburg Landau equations in the theory of Superconductivity". In: *Sov. Phys. JETP* 36 (1959), p. 1364 (cit. on p. 8).

[Hah50] E. L. Hahn. "Spin Echoes". In: *Phys. Rev.* 80 (4 1950), pp. 580–594. DOI: 10.1103/PhysRev.80.580 (cit. on p. 106).

[Hug] *Hughes Circuits, Inc.* URL: http://www.hughescircuits.com/ (cit. on p. 60).

[Hyp08] Hypres Inc. *Niobium Integrated Circuit Fabrication Design Rules*. 2008. URL: http://www.hypres.com/foundry/niobium-process (cit. on p. 37).

[JC63] E.T. Jaynes and F.W. Cummings. "Comparison of quantum and semiclassical radiation theories with application to the beam maser". In: *Proc. IEEE 51* 51 (1963), pp. 89–109. DOI: 10.1109/PROC.1963.1664 (cit. on p. 38).

[JNN12] J. R. Johansson, P. D. Nation, and F. Nori. "QuTiP: An open-source Python framework for the dynamics of open quantum systems". In: *Comp. Phys. Comm.* 183 (2012), p. 1760. DOI: 10.1016/j.cpc.2012.02.021 (cit. on p. 48).

[Joh28] J. B. Johnson. "Thermal Agitation of Electricity in Conductors". In: *Phys. Rev.* 32 (1 1928), pp. 97–109. DOI: 10.1103/PhysRev.32.97 (cit. on p. 64).

[Jos62] B. D. Josephson. "Possible new effects in superconductive tunnelling". In: *Physics Letters* 1 (1962), p. 251. DOI: 10.1016/0031-9163(62)91369-0 (cit. on p. 8).

[KMS+07] K. Kakuyanagi, T. Meno, S. Saito, H. Nakano, K. Semba, H. Takayanagi, F. Deppe, and A. Shnirman. "Dephasing of a Superconducting Flux Qubit". In: *Phys. Rev. Lett.* 98 (4 2007), p. 047004. DOI: 10.1103/PhysRevLett.98.047004 (cit. on pp. 102, 103, 114).

[KG01] Navin Khaneja and Steffen J. Glaser. "Cartan decomposition of SU(2n) and control of spin systems". In: *Chemical Physics* 267 (2001), p. 11. DOI: 10.1016/S0301-0104(01)00318-4 (cit. on p. 90).

[KG83] A. Khanna and Y. Garault. "Determination of Loaded, Unloaded, and External Quality Factors of a Dielectric Resonator Coupled to a Microstrip Line". In: *Microwave Theory and Techniques, IEEE Transactions on* 31.3 (1983), pp. 261–264. ISSN: 0018-9480. DOI: 10.1109/TMTT.1983.1131473 (cit. on p. 33).

[Kit03] A. Yu. Kitaev. "Fault-tolerant quantum computation by anyons". In: *Annals of Physics* 303.1 (2003), pp. 2 –30. DOI: 10.1016/S0003-4916(02)00018-0 (cit. on p. 4).

[KYG+07] Jens Koch, Terri M. Yu, Jay Gambetta, A. A. Houck, D. I. Schuster, J. Majer, Alexandre Blais, M. H. Devoret, S. M. Girvin, and R. J. Schoelkopf. "Charge-insensitive qubit design derived from the Cooper pair box". In: *Phys. Rev. A* 76 (4 2007), p. 042319. DOI: 10.1103/PhysRevA.76.042319 (cit. on p. 50).

[Kos72] A. Kossakowski. "On quantum statistical mechanics of non-Hamiltonian systems". In: *Rep. Math. Phys* 3.247 (1972) (cit. on p. 22).

[KF48] P. Kusch and H. M. Foley. "On the Intrinsic Moment of the Electron". In: *Phys. Rev.* 73 (1948), p. 412. DOI: 10.1103/PhysRev.73.412 (cit. on p. 38).

[LR47] W. E. Lamb and R. C. Retherford. "Fine Structure of the Hydrogen Atom by a Microwave Method". In: *Phys. Rev.* 72 (1947), pp. 241–243. DOI: 10.1103/PhysRev.72.241 (cit. on p. 38).

[Lin76] G. Lindblad. "On the Generators of Quantum Dynamical Semigroups". In: *Commun. Math. Phys.* 48 (1976), p. 119 (cit. on pp. 22, 48).

[LWT+06] Yu-xi Liu, L. F. Wei, J. S. Tsai, and Franco Nori. "Controllable Coupling between Flux Qubits". In: *Phys. Rev. Lett.* 96 (6 2006), p. 067003. DOI: 10.1103/PhysRevLett.96.067003 (cit. on p. 87).

[Llo95] Seth Lloyd. "Almost Any Quantum Logic Gate is Universal". In: *Phys. Rev. Lett.* 75 (2 1995), pp. 346–349. DOI: 10.1103/PhysRevLett.75.346 (cit. on p. 2).

[LL35] F. London and H. London. "The Electromagnetic Equations of the Supraconductor". In: *Proc. Roy. Soc. (London)* A149 (1935), p. 71. DOI: 10.1098/rspa.1935.0048 (cit. on pp. 7, 37).

[MOPL+09] Francois Mallet, Florian R. Ong, Agustin Palacios-Laloy, Francois Nguyen, Patrice Bertet, Denis Vion, and Daniel Esteve. “Single-shot qubit readout in circuit quantum electrodynamics”. In: *Nat Phys* 5.11 (2009), pp. 791–795. DOI: 10.1038/nphys1400 (cit. on p. 118).

[Mar] *Marki Microwave, Inc.* URL: http://www.markimicrowave.com/ (cit. on pp. 68, 70, 73).

[MNA+02] J. M. Martinis, S. Nam, J. Aumentado, and C. Urbina. “Rabi Oscillations in a Large Josephson-Junction Qubit”. In: *Phys. Rev. Lett.* 89 (2002), p. 117901. DOI: 10.1103/PhysRevLett.55.1543 (cit. on p. 10).

[MO33] W. Meissner and R. Ochsenfeld. “Ein neuer Effekt bei Eintritt der Supraleitfähigkeit”. In: *Naturwissenschaften* 21 (1933), p. 787. DOI: 10.1007/BF01504252 (cit. on p. 7).

[Mer07] N. D. Mermin. *Quantum Computer Science: An Introduction*. 1st ed. Cambridge University Press, 2007 (cit. on p. 4).

[Min] *Mini-Circuits*. URL: http://www.mini-circuits.com (cit. on p. 65).

[MOL+99] J. E. Mooij, T. P. Orlando, L. Levitov, Lin Tian, Caspar H. van der Wal, and Seth Lloyd. “Josephson Persistent-Current Qubit”. In: *Science* 285.5430 (1999), pp. 1036–1039. DOI: 10.1126/science.285.5430.1036 (cit. on pp. 11, 13).

[Moo65] Gordon E. Moore. “Cramming more components onto integrated circuits”. In: *Electronics* 38.8 (1965) (cit. on p. 3).

[NPT99] Y. Nakamura, Yu. A. Pashkin, and J. S. Tsai. “Coherent control of macroscopic quantum states in a single-Cooper-pair box”. In: *Nature* 398 (1999), pp. 786–788. DOI: 10.1038/19718 (cit. on pp. 3, 10).

[NC04] Michael A. Nielsen and Isaac L. Chuang. *Quantum Computation and Quantum Information*. Cambridge University Press, 2004. ISBN: 978-0521635035 (cit. on p. 20).

[Nie74] J. Niemeyer. In: *PTB-Mitt.* 84 (1974), p. 251 (cit. on p. 59).

[Nyq28] H. Nyquist. “Thermal Agitation of Electric Charge in Conductors”. In: *Phys. Rev.* 32 (1 1928), pp. 110–113. DOI: 10.1103/PhysRev.32.110 (cit. on p. 64).

[Onn11] H. K. Onnes. “The resistance of pure mercury at helium temperatures”. In: *Commun. Phys. Lab. Univ. Leiden* 12 (1911), p. 120 (cit. on p. 7).

[OMT+99] T. P. Orlando, J. E. Mooij, Lin Tian, Caspar H. van der Wal, L. S. Levitov, Seth Lloyd, and J. J. Mazo. “Superconducting persistent-current qubit”. In: *Phys. Rev. B* 60.22 (1999), pp. 15398–15413. DOI: 10.1103/PhysRevB.60.15398 (cit. on p. 14).

[Pin02] Mark Pinsky. *Introduction to Fourier Analysis and Wavelets*. Brooks/Cole, 2002. ISBN: 0-534-37660-6 (cit. on p. 54).

[PGM+12] S. Poletto, Jay M. Gambetta, Seth T. Merkel, John A. Smolin, Jerry M. Chow, A. D. Córcoles, George A. Keefe, Mary B. Rothwell, J. R. Rozen, D. W. Abraham, Chad Rigetti, and M. Steffen. “Entanglement of Two Superconducting Qubits in a Waveguide Cavity via Monochromatic Two-Photon Excitation”. In: *Phys. Rev. Lett.* 109 (24 2012), p. 240505. DOI: 10.1103/PhysRevLett.109.240505 (cit. on p. 87).

[Poz05] David M. Pozar. *Microwave Engineering*. 3rd ed. John Wiley & Sons, Inc., 2005. ISBN: 0-471-64451-X (cit. on pp. 25, 27, 32, 35).

[Qsi] *Quantum Systems for Information Technology Lecture Notes*. URL: http://qudev.ethz.ch/content/courses/QSIT12/QSIT12_VO7_slides.pdf (cit. on p. 60).

[RH01] J. M. Raimond and S. Haroche. “Manipulating quantum entanglement with atoms and photons in a cavity”. In: *Rev. Mod. Phys.* 73 (2001), pp. 565–582. DOI: 10.1103/RevModPhys.73.565 (cit. on p. 38).

[Ram50] Norman F. Ramsey. “A Molecular Beam Resonance Method with Separated Oscillating Fields”. In: *Phys. Rev.* 78 (1950), p. 695. DOI: 10.1103/PhysRev.78.695 (cit. on p. 104).

[RGP+12] Chad Rigetti, Jay M. Gambetta, Stefano Poletto, B. L. T. Plourde, Jerry M. Chow, A. D. Córcoles, John A. Smolin, Seth T. Merkel, J. R. Rozen, George A. Keefe, Mary B. Rothwell, Mark B. Ketchen, and M. Steffen. "Superconducting qubit in a waveguide cavity with a coherence time approaching 0.1 ms". In: *Phys. Rev. B* 86 (10 2012), p. 100506. DOI: 10.1103/PhysRevB.86.100506 (cit. on p. 3).

[Rog] *Rogers Corporation RT/duroid 6010*. URL: http://www.rogerscorp.com/ (cit. on p. 60).

[SPW09] Bianca Schroeder, Eduardo Pinheiro, and Wolf-Dietrich Weber. "DRAM Errors in the Wild: A Large-Scale Field Study". In: *SIGMETRICS*. 2009 (cit. on p. 3).

[SHS+07] D. I. Schuster, A. A. Houck, J. A. Schreier, A. Wallraff, J. M. Gambetta, A. Blais, L. Frunzio, B. Johnson, M. H. Devoret, S. M. Girvin, and R. J. Schoelkopf. "Resolving photon number states in a superconducting circuit". In: *Nature* 445 (2007), pp. 515–518. DOI: 10.1038/nature05461 (cit. on p. 10).

[SZ97] M. O. Scully and M. S. Zubairy. *Quantum optics*. Cambridge University Press, 1997. ISBN: 0-521-43595-1 (cit. on p. 41).

[Sha94] R. Shankar. *Introduction to Quantum Mechanics*. 2nd: Springer, 1994. ISBN: 978-0306447907 (cit. on p. 21).

[Sho95] Peter W. Shor. "Scheme for reducing decoherence in quantum computer memory". In: *Phys. Rev. A* 52 (1995), R2493–R2496. DOI: 10.1103/PhysRevA.52.R2493 (cit. on p. 4).

[SLH+04] R. W. Simmonds, K. M. Lang, D. A. Hite, S. Nam, D. P. Pappas, and John M. Martinis. "Decoherence in Josephson Phase Qubits from Junction Resonators". In: *Phys. Rev. Lett.* 93 (7 2004), p. 077003. DOI: 10.1103/PhysRevLett.93.077003 (cit. on p. 87).

[Sim01] Rainee N. Simons. *Coplanar Waveguide Circuits, Components and Systems*. Ed. by Kai Chang. Microwave and Optical Engineering. John Wiley & Sons, Inc., 2001. ISBN: 0-471-16121-7 (cit. on p. 36).

[SHD+09] C. Song, T. W. Heitmann, M. P. DeFeo, K. Yu, R. McDermott, M. Neeley, John M. Martinis, and B. L. T. Plourde. "Microwave response of vortices in superconducting thin films of Re and Al". In: *Phys. Rev. B* 79 (17 2009), p. 174512. DOI: 10.1103/PhysRevB.79.174512 (cit. on p. 80).

[Spe] *Spectrum Systementwicklung GmbH*. URL: http://www.spec.de/ (cit. on p. 72).

[Ste96] A. M. Steane. "Error Correcting Codes in Quantum Theory". In: *Phys. Rev. Lett.* 77 (1996), pp. 793–797. DOI: 10.1103/PhysRevLett.77.793 (cit. on p. 4).

[Ste11] Matthias Steffen. "Superconducting Qubits Are Getting Serious". In: *Physics* 4 (2011), p. 103. DOI: 10.1103/Physics.4.103 (cit. on p. 3).

[SAM+06] Matthias Steffen, M. Ansmann, R. McDermott, N. Katz, Radoslaw C. Bialczak, Erik Lucero, Matthew Neeley, E. M. Weig, A. N. Cleland, and John M. Martinis. "State Tomography of Capacitively Shunted Phase Qubits with High Fidelity". In: *Phys. Rev. Lett.* 97 (2006), p. 050502. DOI: 10.1103/PhysRevLett.97.050502 (cit. on p. 98).

[Tek] *Tektronix, Inc.* URL: http://www.tek.com/ (cit. on pp. 70, 73).

[Tin04] M. Tinkham. *Introduction to Superconductivity*. 2nd ed. Dover Books, 2004. ISBN: 0-486-43503-2 (cit. on p. 7).

[Tur37] A. M. Turing. "On Computable Numbers, with an Application to the Entscheidungsproblem". In: *Proc. London Math. Soc.* s2-42.1 (1937), pp. 230–265. DOI: 10.1112/plms/s2-42.1.230 (cit. on p. 1).

[Tur39] A. M. Turing. "Systems of Logic Based on Ordinals". PhD thesis. Princeton University, 1939 (cit. on p. 1).

[Ghz] *UCSB GHzDAC*. URL: http://www.physics.ucsb.edu/~martinisgroup/electronics.shtml (cit. on p. 70).

[VSS11] R. Vijay, D. H. Slichter, and I. Siddiqi. “Observation of Quantum Jumps in a Superconducting Artificial Atom”. In: *Phys. Rev. Lett.* 106 (11 2011), p. 110502. DOI: 10.1103/PhysRevLett.106.110502 (cit. on p. 72).

[WSB+07] A. Wallraff, D. I. Schuster, A. Blais, J. M. Gambetta, J. Schreier, L. Frunzio, M. H. Devoret, S. M. Girvin, and R. J. Schoelkopf. “Sideband Transitions and Two-Tone Spectroscopy of a Superconducting Qubit Strongly Coupled to an On-Chip Cavity”. In: *Phys. Rev. Lett.* 99 (5 2007), p. 050501. DOI: 10.1103/PhysRevLett.99.050501 (cit. on p. 87).

[Wün05] S. Wünsch. “Supraleitende koplanare Mikrowellenfilter für radioastronomische Empfänger bei 15 K”. PhD thesis. Universität Karlsruhe (TH), 2005. ISBN: 3-937300-60-0 (cit. on p. 37).

[YHC+02] Y. Yu, S. Han, X. Chu, S.-I. Chu, and Z. Wang. “Coherent Temporal Oscillations of Macroscopic Quantum States in a Josephson Junction”. In: *Science* 296 (2002), pp. 889–892. DOI: 10.1126/science.1069452 (cit. on p. 10).

[ZB07] A. M. Zagoskin and A. Blais. “Superconducting Qubits”. In: *Physics in Canada* 63.4 (2007), pp. 215–227 (cit. on p. 10).

List of Publications

[BJSJ+10] V. Brosco, M. Jerger, P. San-José, G. Zarand, A. Shnirman, and G. Schön. "Prediction of resonant all-electric spin pumping with spin-orbit coupling". In: *Phys. Rev. B* 82 (4 2010), p. 041309. DOI: 10.1103/PhysRevB.82.041309.

[JPM+11] M. Jerger, S. Poletto, P. Macha, U. Hübner, A. Lukashenko, E. Il'ichev, and A. V. Ustinov. "Readout of a qubit array via a single transmission line". In: *EPL (Europhysics Letters)* 96.4 (2011), p. 40012. DOI: 10.1209/0295-5075/96/40012.

[JPM+12] M. Jerger, S. Poletto, P. Macha, U. Hübner, E. Il'ichev, and A. V. Ustinov. "Frequency division multiplexing readout and simultaneous manipulation of an array of flux qubits". In: *Applied Physics Letters* 101.4, 042604 (2012), p. 042604. DOI: 10.1063/1.4739454.

[PRW+12] S. Probst, H. Rotzinger, S. Wünsch, P. Jung, M. Jerger, M. Siegel, A. V. Ustinov, and P. A. Bushev. "Anisotropic rare-earth spin ensemble strongly coupled to a superconducting resonator". submitted to Phys. Rev. Lett. 2012.

[SKW+12] S. T. Skacel, Ch. Kaiser, S. Wünsch, H. Rotzinger, A. Lukashenko, M. Jerger, G. Weiss, M. Siegel, and A. V. Ustinov. "Probing the TLS Density of States in Thin a-SiO Films using Superconducting Lumped Element Resonators". in preparation. 2012.

Zusammenfassung und Ausblick

Die vorliegende Arbeit stellt eine Methode vor, die es ermöglicht den Zustand einer beliebigen Anzahl an supraleitenden Qubits mit minimalem Aufwand an Ressourcen gleichzeitig zu bestimmen. Hierfür wird ein Frequenzmultiplexverfahren verwendet, dass die Auslesesignale sämtlicher Qubits auf einer einzelnen Hochfrequenzübertragungsleitung zusammenfügt. Hierzu wird jedes Qubit mit einem Schwingkreis im Mikrowellenbereich kombiniert, der durch induktive Wechselwirkung mit dem Qubit eine Verstimmung erfährt, dessen Vorzeichen vom Zustand des Qubits abhängt. Alle Schwingkreise werden an eine gemeinsame Übertragungsleitung angeschlossen, durch die ihre Resonanzfrequenzen und damit auch die Zustände aller Qubits bestimmt werden können.

Mit Hilfe eines schmalbandigen Direktmischempfängers, der bei vielen Arbeitsgruppen auf dem Gebiet der supraleitenden Qubits zum Standard gehört, kann ein Qubit nach dem anderen gemessen werden. Dies erlaubt es bereits die Parameter aller Qubits, die sich auf dem selben Mikrochip befinden, mit einem Abkühlvorgang und einer Messleitung zu charakterisieren. Da beim gewählten Layout Mikrowellen, deren Frequenz nicht mit der Resonanzfrequenz eines der Schwingkreise übereinstimmt, ungestört durch die Probe übertragen werden, können sogar mehrere Proben in Serie geschaltet werden. Solche nacheinander ausgeführten Charakterisierungsmessungen, um etwa die Übergangsfrequenzspektren, Zerfalls- und Kohärenzzeiten der Qubits zu bestimmen, sind in den Abschnitten 4.1 und 4.2 vorgestellt.

Das volle Potenzial der Methode liegt allerdings im simultanen und unabhängigen Auslesen aller Qubits. Werden mehrere Frequenzenkomponenten, eine für jedes zu messende Qubit, durch die Probe gesendet, so wird der Zustand jedes Qubits in guter Näherung auf genau eine Komponente aufmoduliert. Der im Verlauf dieser Arbeit entwickelte Messaufbau (Schaubild 3.10) verwendet schnelle D/A und A/D Signalwandler und

digitale Signalverarbeitung um Signale mit einer beliebigen Anzahl an Frequenzkomponenten innerhalb einer Bandbreite von etwa 1 GHz zu erzeugen und erfassen, und kann somit eine beliebige Anzahl an Qubits gleichzeitig auszulesen. Mit diesem Aufbau wurden Experimente an bis zu sechs Qubits parallel durchgeführt, die im Abschnitt 4.3 vorgestellt sind.

Die Berechnungen in Abschnitt 2.5 zeigen, dass Interferenz zwischen den Auslesekanälen beinahe unabhängig von ihrer Gesamtzahl ist und vorrangig von ihrem Frequenzabstand abhängt. Der wichtigste Parameter der diesen Abstand nach unten begrenzt ist der Betriebsgütefaktor Q_L der Schwingkreise, die stark an die Messleitung gekoppelt sind um schnelles Auslesen zu gewährleisten. Simulationen zufolge garantiert ein Kanalabstand von zwei Linienbreiten ein Übersprechen von weniger als -10 dB und ein Abstand von 6,5 Linienbreiten ein Übersprechen von weniger als -20 dB. Die für Messungen verwendete Probe weist Linienbreiten von etwa 6 MHz auf, was theoretisch bis zu 80 Kanäle pro GHz Auslesebandbreite mit weniger als -10 dB Übersprechen oder 25 Kanäle pro GHz mit weniger als -20 dB Übersprechen erlaubt.

In der jetztigen Implementierung ist die Hauptschwäche der Methode die Tatsache, dass eine Einzelmessung nicht ausreicht um den Zustand der Qubits sicher zu bestimmen. Derzeit erhältliche Tieftemperaturverstärker im Mikrowellenbereich weisen Rauschtemperaturen von mehreren Kelvin auf und fügen zu jedem Signalphoton mehrere Rauschphotonen hinzu. Bei der Messung einzelner Schwingkreise konnte dieses Problem durch parametrische Verstärker auf Basis von Josephson-Kontakten gelöst werden, die annähernd quantenrauschbegrenzten Betrieb erreichen. Leider liegt das Verstärkungs-Bandbreite-Produkt typischer parametrischer Verstärker nur bei wenigen MHz, so dass ein separater Verstärker für jeden Auslesekanal vorgesehen werden müsste. Für Systeme mit vielen Kanälen ist ein auf der Birfurkation eines nichtlinearen Schwingkreises basierendes Ausleseverfahren, ähnlich der bei Transmon Qubits eingesetzten Technik, eine praktikablere Lösung. Hierbei rastet der Schwingkreis in einem von zwei klassischen Zuständen ein, abhängig vom Quantenzustand des Qubits, und behält diesen bei. Der Auslesevorgang kann dann über die Lebensdauer des Qubits hinaus fortgesetzt werden, bis ein

ausreichender Signal-Rauschabstand erreicht wird. Zukünftige Verbesserungen des Ausleseverfahrens weisen in diese Richtung.

Vor kurzem wurden neue Proben fertiggestellt, die sowohl eine gemultiplexte Ausleseleitung als auch die Möglichkeit von Qubit-Qubit Wechselwirkungen mittels eines als Quantenbus betriebenen Schwingkreises hoher Güte vorsehen. Diese Proben werden die Ausführung von Zweiqubitgattern ermöglichen und damit der erste echte am KIT betriebene Quantencomputer sein.

Danksagung

An erster Stelle möchte ich Professor Alexey Ustinov danken, dass er mir die Promotion in seiner Arbeitsgruppe ermöglicht hat. Seine guten Kontakte zu Labors in aller Welt und seine ständigen Anstrengungen die Ausstattung seines Labors noch weiter zu verbessern und natürlich sein wissenschaftlicher Input waren unverzichtbar für meine Arbeit.

Professor Hans Mooij danke ich für die Übernahme des Korreferats und die zahlreichen Verbesserungsvorschläge, durch die er mich an seiner jahrzehntelangen Erfahrung mit Fluss-Qubits teilhaben ließ.

Besonderer Dank gilt meinen direkten Betreuern Stefano Poletto und Jürgen Lisenfeld. Viele Grundlagen und die ersten Ergebnisse entstanden in enger Zusammenarbeit mit Stefano, bevor er zu IBM in die Vereinigten Staaten wechselte. Jürgen stand mir mit seinen Kenntnissen besonders von experimentellen Methoden für Qubit-Messungen immer zur Seite und investierte außerdem viele Stunden in das Lektorat meiner Arbeit.

Pascal Macha vom IPHT Jena entwarf die ersten Qubits und war meine Schnittstelle zur Fabrikation. Bei unseren gemeinsamen Publikationen war er immer der engagierteste Kritiker.

Mit seinem breiten Wissen in Tieftemperaturphysik, Fabrikationstechniken, Elektronik und mehr konnte mir Hannes Rotzinger stets hilfreiche Antworten auf die ausgefallensten Fragen geben.

Sasha Lukashenko und Alexey Feofanov führten mich in die Benutzung unserer Kryostate ein, kümmerten sich um ihre Instandhaltung und halfen bei der Problembeseitigung.

Die Elektronikwerkstatt, geleitet von Roland Jehle, entwarf und produzierte im Laufe der Zeit einige Gimmicks die meine Messaufbauten zusammenhielten.

Meinen Bürokollegen Tobias Wirth, Kirill Fedorov, Jochen Zimmer und Sebastian Probst sowie den weiteren Doktoranden der Gruppe, Grigorij Grabovski, Susanne Butz, Philipp Jung und Anastasia Shcherbakova danke

ich für die zahlreichen Diskussionen und alle gemeinsamen außeruniversitären Unternehmungen.

Unseren übrigen Postdoktoranden, Pavel Bushev, Gerda Fischer, Fengbin Song und Martin Weides danke ich für die gute Zusammenarbeit.

Wenn ich eine Pause von der Physik brauchte, war unser Systemadministrator Lars Behrens immer für eine Fachsimpelei zu haben.

Allen anderen Institusmitgliedern danke ich für die angenehme Zeit am Physikalischen Institut.

Zu guter Letzt danke ich meiner Frau Dorit und meinen Eltern Oswald und Maria Jerger für alle Unterstützung die ich während meines Studiums und darüber hinaus von ihnen erhalten habe.